

DELFT UNIVERSITY OF TECHNOLOGY

**SEQUENCE OPTIMISATION FOR MAGNETIC
RESONANCE FINGERPRINTING**

Author:

D.G.J. HEESTERBEEK
(4469437)

Supervisors:

Dr. F.M. VOS
Prof. Dr. Ir. M.B. VAN GIJZEN
Ir. M.A. NAGTEGAAL

Faculty of Applied Sciences
Faculty of Electrical Engineering, Mathematics & Computer Science

Delft,
September 23, 2021

SEQUENCE OPTIMISATION FOR MAGNETIC RESONANCE FINGERPRINTING

Master Thesis

In partial fulfillment of the requirements for the degree of

Master of Science

at the Delft University of Technology

To be defended on 27 September 2021, 14:30-17:30

By

D.G.J. HEESTERBEEK

Faculty of Applied Sciences,
Faculty of Electrical Engineering, Mathematics & Computer Science,

Delft University of Technology, Delft, The Netherlands,

Born in Beverwijk, The Netherlands.

*Details are all that matters
God dwells in these and you never get to see Him
if you don't struggle to get them right.*

Stephan Jay Gould

CONTENTS

Preface	vi
Abstract	vii
1 Introduction	1
2 Theory	4
2.1 MR principles	4
2.1.1 Evolution of magnetisation	5
2.1.2 Signal model	10
2.2 Gradient-spoiled SSFP sequences	13
2.2.1 Extended Phase Graphs	16
2.2.2 Modelling the gradient-spoiled SSFP sequence	18
2.3 Magnetic Resonance Fingerprinting	20
2.4 The multi-component setting	22
2.5 Cramér-Rao Lower Bound	23
2.6 Undersampling error	24
2.6.1 Signal model for undersampled k-space acquisition using convolution	24
2.6.2 Modelling parameter estimation in MRF	26
2.6.3 Perturbation theory	27
2.6.4 Linearization and isolation of the tissue parameters	28
2.7 Optimisation method	31
3 Methods	32
3.1 Optimisation <i>Framework I</i> : multi-component model and stochastic errors	33
3.2 Optimisation <i>Framework II</i> : undersampling errors	34
3.2.1 Signal model extended with stochastic term	34
3.2.2 Adding transmit phase	34
3.2.3 Variable reference proton density	35
3.2.4 Extended undersampling model	35
3.2.5 Redefining the linearization variables	37
3.3 Optimisation problems	38
3.3.1 Optimisation problems <i>Framework I</i>	38
3.3.2 Optimisation problems <i>Framework II</i>	39
3.4 Experiments	40
4 Results	43
4.1 Optimisation <i>Framework I</i>	43
4.1.1 Multi-component optimisation; Opt α	44

4.1.2	Multi-component optimisation; Opt β	45
4.2	Optimisation <i>Framework II</i>	49
4.2.1	Effect of the transmit phase	49
4.2.2	Optimised sequences	50
4.2.3	In vivo validation.	51
4.2.4	Model based insights into the effects of optimisation	64
5	Discussion	75
6	Conclusion	79
	Acknowledgements	80
	References	81
	Appendices	84
A	Undersampling model in a multi-component setting	84
B	Slice selection	86
C	Principle of reciprocity	88
D	Noise in k-space	91
E	Variable density sampling	93
F	Fourier analysis of the \mathcal{E}_2 error	94
G	ISMRM 2021 Annual meeting	97
	Curriculum Vitae	101

PREFACE

This research is conducted as partial fulfillment of the requirements for the degree of Master of Science for Applied Physics (AP) and Applied Mathematics (AM). When I started orientating for a Master project, I tried to find a direction in which physics could be combined with an interesting mathematical foundation. Most of the courses I followed for the physics program were in quantum mechanics. Although this direction keeps on fascinating me, final projects in quantum mechanics are usually too experimental for my taste, or not very applicable as the focus is on a small theoretical phenomenon. For this reason I started to look in the direction of medical imaging. The course *Medical Imaging Systems and Signals* from Dr. Frans Vos, which I followed during my physics Master, sparked my interest in MRI research because it combined an interesting theoretical basis with directly applicable results. This direction however, did not seem to be easily combined with mathematics and for a while I was willing to drop the idea of a combined Master project such that I could pursue my final project for AP in the MRI direction for which I had become passionate.

Luckily after a course in *Mathematical Data Science*, I met Prof. Martin van Gijzen. His research also focuses on MRI but from a mathematical perspective and suddenly a combined final project was within reach again. To my surprise both professors had not worked together on previous occasions and a nice multi-disciplinary team together with Ir. Martijn Nagtegaal was formed.

Even though Physics and Mathematics are inseparable, I will try to point out which part of the thesis focuses more on the physical side of the problem and which part focuses more on the mathematical aspects. The model developed to suppress the stochastic noise is based on the Cramér-Rao bound which has a deep mathematical meaning. The undersampling error is more directly related to imaging physics, although for the development of the models to predict this error a significant amount of mathematical tools is required such as perturbation theory. A hybrid model which combines a multi-component signal model with undersampling has been developed by this author and is presented in Appendix A. An interesting finding from this research project about noise correlation has been presented in Appendix D. I encourage the reader to take a look at these results. As the requirements for the report for AP and AM were quite different compromises have been made. A voluminous appendix has been added to keep the report more concise.

The results related to the Cramér-Rao bound optimisation have been accepted for the ISMRM conference and were presented on 17 May 2021. A paper based on the optimisations for the undersampling error is under construction. The development of this research project took a considerable amount of energy, but returned more in happiness.

ABSTRACT

Magnetic Resonance Fingerprinting (MRF) is a relatively new approach for simultaneously estimating multiple quantitative maps in one acquisition. Sequence optimisation for MRF can be a powerful tool in increasing the accuracy and precision of the quantitative results. Multi-component analysis in the MRF framework can distinguish multiple different tissues in one voxel such as myelin water and white matter which play an important role in monitoring progressive diseases such as multiple sclerosis. Using the estimation theoretic Cramér-Rao bound, optimisations of the acquisition sequences can be performed, that increase the precision of the resulting tissue maps. The effect of this optimisation has been confirmed using numerical simulations. Speed-ups in MRF are generated using significant undersampling of the k-space information. This results in spatially coherent undersampling artefacts, that generally is the dominating error source for regular T_1 and T_2 mapping. The undersampling artefacts can be predicted using a mathematical model leveraging on techniques from perturbation theory. Numerical simulations suggested that optimisations of the acquisition parameters are effective in effectively reducing the undersampling error. This was confirmed using in vivo scans. The optimisations resulting from these two different models are easily implemented in future clinical practice.

1

INTRODUCTION

Magnetic Resonance Imaging (MRI) is one of the leading medical imaging modalities for soft tissues. It offers high quality images in a non-invasive manner without the use of ionising radiation. Additionally, the clinical success of MRI derives from its ability to generate multiple different contrasts between tissues, relying on the physical phenomena called Nuclear Magnetic Resonance (NMR). Over the years many Nobel prizes have been awarded for contributions to this field. Some examples of Nobel laureates in this area are Otto Stern (1943), Isidor Rabi (1944), Felix Bloch (1952) and Peter Mansfield (2003).

Currently most clinical scans are qualitative in nature, presenting relative image intensities instead of meaningful quantitative values. Different acquisition sequences emphasise different contrast mechanisms such as the density of water protons or relaxation parameters T_1 or T_2 which will be explained in Chapter 2.1. The measured signal depends on the imaging settings, but also on the characteristics of the MR scanner which are not constant through time and differ between scanners of different vendors. Furthermore, interpreting images requires understanding of the interplay between the contrast mechanisms and the underlying pathology. For these reasons qualitative scans fail to generate quantitatively reproducible and easily interpretable results.

Quantitative MRI (qMRI) aims to measure the parameters that underlie the physical processes that determine the MR signal instead of merely depending on these parameters as is the case for qualitative scans. These quantitative scans offer improved longitudinal and inter-scanner reproducibility from which patient care could benefit as this may allow for comparison between maps acquired at different times or using different scanner hardware. Quantitative information about temporal changes in MR tissue parameters can function as biomarker for various diseases such as multiple sclerosis, osteoarthritis, iron overload and myocardial infarction [1].

Despite the advantages of quantitative qMRI, it suffers from long acquisition times. Conventional qMRI sequences such as inversion recovery to create a T_1 map or the Carr-

Purcell-Meiboom-Gill (CPMG) acquisition to create a T_2 map, obtain results over a clinically impractical time [2]. Multiple quantitative images reflecting different contrast mechanisms can often help for diagnostics, but acquiring more than one quantitative map requires a new scan which further extends the acquisition time. Magnetic Resonance Fingerprinting (MRF) has been proposed to overcome these boundaries [3]. MRF offers a flexible framework in which freely chosen acquisition parameters are used to probe the transient-state signal evolution. Probing the transient-state signal evolution is generally done by acquiring multiple low-quality images at different time points. The low-quality images are obtained by undersampling the k-space read-out which results in a speed-up of the acquisition time. The result is a unique signal measurement or fingerprint for every pixel, from which the desired quantitative tissue properties can be derived [2, 4, 5]. Using MRF it is possible to acquire multiple spatially-registered quantitative maps in the time it would take conventional methods to obtain just one map [6]. The technique is not yet widely adopted in clinical practice, but rapid improvements in the field make this goal realistic in the near future.

Usually in MRF, single component matching is performed where one assumes that there is only one tissue present in each voxel. However, this assumption breaks down when a voxel is on the border of two neighbouring tissues or when multiple tissues are diffusely merged. An example of the latter situation is the case of myelin and white matter. These partial volume effects can cause blurring artefacts when single component matching is performed. Multi-component (MC) analysis takes into account that one voxel can contain multiple tissues and assumes that the measured signal is composed of a weighted sum of the signals from the separate tissues in a voxel. Using advanced algorithms such as SPIJN [7], these different tissues can be identified and component maps can be constructed. The MC analysis reduces blurring due to partial volume effects and the resulting component maps are valuable in clinical diagnostics for tracing diseases such as multiple sclerosis.

When an MRF reconstruction of quantitative maps is performed with low-quality undersampled images, this results in so called undersampling artefacts. These artefacts are correlated with the true tissue parameter maps and cannot be modelled as spatio-temporal incoherent stochastic noise. A comprehensive model for the undersampling error was introduced in [8].

By using different acquisition parameters the artefacts in MRF maps due to multi-component and undersampling effects can be suppressed. Using numerical tools the acquisition parameters that can be freely chosen in MRF, might be optimised such that the resulting maps become more accurate or precise. As no closed-form solution is required to make quantitative information about the spin relaxation or experimental imperfections traceable when using MRF, there are many degrees of freedom for the optimisation.

Multiple studies on optimisation of acquisition parameters have been conducted in which different error models and optimisation metrics have been applied. B. Zhao et al. focused on optimisations using a single component model to reduce stochastic noise-like artefacts by optimising the Cramér-Rao lower bound (CRLB) [9]. J. Assländer et al. also applies the CRLB metric to reduce stochastic noise, but performed the optimisations in

the context of the hybrid state [10]. A very different approach was adopted by O. Cohen and R.S. Rosen, who focused on orthogonalising of the dictionary atoms to increase the differentiating ability of different fingerprints [11].

For this research project the overarching aim is to enhance the MRF image quality and/or reduce the scan time by using numerical methods to optimise the acquisition parameters. The resulting optimisations can be easily implemented in clinical practice as the potential improvements in image quality are achieved by merely changing the acquisition parameters, without the need for additional scan or processing steps.

This work can be separated into two main veins of research. The first part of the research aimed to enhance the MRF image quality by performing an optimisation of the acquisition parameters using an MC model. Here the goal was to reduce the errors resulting from stochastic white noise which is a common first order approximation of the errors involved. This part is referred to as Optimisation *Framework I* and the results were verified using numerical simulations.

The second part of the research aimed to enhance the MRF image quality by performing an optimisation of the acquisition parameters using a model which captures the undersampling error. Here the goal was to reduce the undersampling artefacts which are inherent to the conventional MRF technique. This part is referred to as Optimisation *Framework II* and the results were verified using numerical simulations, scans of a phantom and an in vivo study.

To the best of this author's knowledge, both these models have not been used before in this context.

In Chapter 2 the required theory will be presented starting with basic MR principles and a more theoretical introduction into MRF. Here the basis of both optimisation frameworks is presented. Chapter 3 is concerned with the full derivation of the frameworks. Chapter 4 contains the results and a thorough analysis of the results. The discussion in Chapter 5 presents the observations from this analysis and Chapter 6 will be concerned with the conclusion and the resulting recommendations. The Appendix contains an extension of the theory and the results and the work presented on the International Society for Magnetic Resonance in Medicine (ISMRM) 2021 conference by this author.

2

THEORY

This chapter is concerned with the theory required for the rest of the research project. Section 2.1 presents the basic concepts underlying magnetic resonance as well as a careful derivation of the signal model from first principles. Readers with a background in MRI can skip this section without loss of continuity. In section 2.3 Magnetic Resonance Fingerprinting is introduced. After this, multi-component problems are introduced in section 2.4 followed by a discussion of the Cramér-Rao bound which will appear to play an important role in Optimisation *Framework I*. Section 2.6 focuses on the undersampling error which is used as the basis for Optimisation *Framework II*. To conclude this chapter a short introduction to the optimisation method is presented in section 2.7. The reader is encouraged to take a look at Appendix A where an undersampling model is developed from a multi-component perspective by this author.

2.1. MR PRINCIPLES

Magnetic Resonance Imaging relies on a quantum mechanical property of atomic nuclei called spin. Nuclei with an odd number of neutrons or an odd number of protons possess a non-zero spin angular momentum, $\vec{\Phi}_s$, which in turn generates a magnetic moment, $\vec{\mu}$. The relation between these quantities is given by:

$$\vec{\mu} = \gamma \vec{\Phi}_s, \quad (2.1)$$

where γ denotes the gyromagnetic ratio which depends on the type of particle under consideration. For whole-body MR imaging the received signal generally comes from ^1H nuclei for which $\frac{\gamma}{2\pi} = 42.8 \text{ MHz/T}$. The ^1H protons are in high concentrations present in the body and can give a strong NMR signal. In general, there is no preferred orientation for the nuclei in a sample and as a result no macroscopic magnetic field is present. In the presence of a strong magnetic field the microscopic spin systems will tend to align their magnetic moment with the field due to the quantum mechanical Zeeman effect [12], which predicts an energy splitting for the different spin orientations. For a sample with

volume V in a homogeneous magnetic field, this results in a macroscopic magnetisation. As the ^1H protons are generally used for MR imaging we will define our macroscopic magnetisation vector \vec{M} as:

$$\vec{M} = \frac{1}{V} \sum_{\substack{^1\text{H protons} \\ \text{in volume } V}} \vec{\mu}_i. \quad (2.2)$$

In imaging this V generally refers to the volume of the voxels in which the sample is divided and \vec{M} becomes spatially dependent. If the sample is in thermodynamic equilibrium in a homogeneous magnetic field $\vec{B}_0 = B_0 \hat{z}$, the macroscopic magnetisation can be derived using Boltzmann statistics [13]:

$$\vec{M}_0 = \frac{B_0 \gamma^2 \hbar^2 \rho_0}{4k_b T} \hat{z}, \quad (2.3)$$

where \hbar is Planck's constant over 2π , k_b is Boltzmann's constant, T is the temperature of the sample (in Kelvin) and ρ_0 is the ^1H proton density.

In the MR scanner there is a large homogeneous magnetic field that will be referred to as the B_0 field. This field creates the net macroscopic magnetisation under equilibrium conditions as discussed above. The strength of the resulting net magnetisation is spatially varying and depends on the type of tissue. This quantity is responsible for the image contrast in MRI scans. The net magnetisation in equilibrium is not detectable using stationary coils. To get a detectable signal the magnetisation must have a component in the transverse plane as will be discussed in section 2.1.2.

2.1.1. EVOLUTION OF MAGNETISATION

The Bloch equations describe the motion of the macroscopic magnetisation in the presence of a magnetic field. To understand how the macroscopic magnetisation behaves in time, an individual spin object is considered first. Approaching this spin as a small current loop generating a magnetic moment, the quantum mechanic nature of the system is neglected but the resulting equations are identical to the ones derived using a quantum mechanical approach (for an interesting quantum mechanical approach to derive the Bloch equations using density-matrices see [14]). A spin system in an external magnetic field will experience a torque when the magnetic moment of the system has a component perpendicular to the external magnetic field. Using the definitions from classical mechanics it is easily derived that the time derivative of the total angular momentum equals the torque:

$$\frac{d\vec{J}_s}{dt} = \vec{N}, \quad (2.4)$$

where \vec{J}_s is the total angular momentum vector and \vec{N} the torque. The torque on any current distribution in a constant external magnetic field is given by:

$$\vec{N} = \vec{\mu} \times \vec{B}_{\text{ext}}, \quad (2.5)$$

where \vec{B}_{ext} is the external magnetic field vector. From experiments the relation between the total angular momentum of a spin system and the magnetic moment is found to be:

$$\vec{\mu} = \gamma \vec{J}_s. \quad (2.6)$$

Combining equation (2.4), (2.5) and (2.6), it can be concluded that:

$$\frac{d\vec{\mu}}{dt} = \gamma \vec{\mu} \times \vec{B}_{\text{ext}}. \quad (2.7)$$

Combining this expression with equation (2.2) to find the expression for a macroscopic sample in an uniform external magnetic field gives the Bloch equation for non-interacting spin systems:

$$\frac{d\vec{M}}{dt} = \gamma \vec{M} \times \vec{B}_{\text{ext}}. \quad (2.8)$$

This equation of motion with only a forcing term, does not describe the situation completely as the ^1H protons in a macroscopic sample do experience interactions which causes damping. These damping mechanisms will be discussed in the next section. A separation of the transverse and longitudinal parts of the magnetisation is used for convenience. The transverse component is denoted by: $\vec{M}_{\perp} = M_x \hat{x} + M_y \hat{y} + 0 \hat{z}$ and the longitudinal part by: $M_z \hat{z}$. In MR scanners the field $\vec{B}_{\text{ext}} = B_0 \hat{z}$ as discussed before, resulting in:

$$\begin{aligned} \frac{d\vec{M}_{\perp}}{dt} &= \gamma B_0 \vec{M} \times \hat{z} \\ \frac{dM_z}{dt} &= 0, \end{aligned} \quad (2.9)$$

for the non-interacting spin system. Solving this system of equations reveals that the longitudinal component M_z remains constant while the transverse component precesses around the z -axis with the Larmor frequency: $\omega_0 = \gamma B_0$. The Larmor frequency depends on the type of spin system at hand via γ . A microscopic group of spins with the same Larmor frequency is called an isochromat. Flipping the system from equilibrium into the transverse plane over a non-zero time, results in a motion depicted in Figure 2.1. Notice that because of the rotation, it is more convenient to describe the situation from a rotating frame of reference. This frame is generally denoted as an x', y', z' coordinate system.

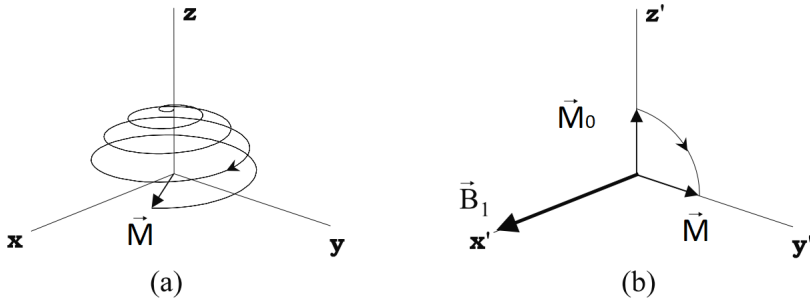


Figure 2.1: A $\frac{\pi}{2}$ flip as seen from the laboratory frame of reference (a) and the rotating frame of reference (b) denoted as an x' , y' , z' coordinate system. The magnetic field term \vec{B}_1 which forces the flip of the macroscopic magnetisation is only depicted in figure (b) for aesthetic reasons. (Modified from: Brown et al. 2014 [13]).

To flip the macroscopic magnetisation, an auxiliary magnetic field \vec{B}_1 is required. This auxiliary field should rotate with the Larmor frequency of the spin system under consideration and is produced using quadrature RF coils in the MR scanner that are able to generate circularly polarised RF excitations. If the auxiliary field rotates with a frequency which differs from the Larmor frequency no flip of the macroscopic magnetisation is achieved. To understand this, one should look at the situation from the rotating frame of reference as is depicted in figure 2.1 (b). If the auxiliary field rotates with the Larmor frequency of the spin system under research, it is stationary in its rotating frame such that the torque on the macroscopic magnetisation remains perpendicular to the magnetisation which allows the flip to happen. The duration of the circularly polarised RF-pulse determines to what extent the macroscopic magnetisation is flipped into the transverse plane. The angle the macroscopic magnetisation moves in the rotating frame with respect to the z' -axis due to the RF-pulse is called the Flip Angle (FA) and will be an important parameter for optimisations performed in this project.

2.1.1.1. T_1 RELAXATION

The longitudinal relaxation or ‘spin-lattice’ relaxation is captured using an empirically determined proportionality constant T_1 . This relaxation of the longitudinal component can be understood as the natural tendency of the system to move back to the equilibrium position which is the lowest energy state. Figure 2.2 depicts this process. The relaxation of the system is caused by the interaction of the spin system with the surrounding lattice. This local interaction can be modelled as a perturbation to the quantum states that exists due to the external magnetic field. Using time-dependent perturbation theory it can be derived that the longitudinal relaxation rate is proportional to the difference $M_0 - M_z$ [13]. Introducing this damping of the longitudinal component in the equations of motion (2.9) the following expression is found:

$$\frac{dM_z}{dt} = \frac{1}{T_1}(M_0 - M_z). \quad (2.10)$$

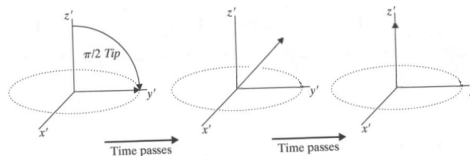


Figure 2.2: Impression of the longitudinal relaxation after a $\frac{\pi}{2}$ flip as seen from the rotating frame. The proportionality factor T_1 determines the rate of this process. (Modified from: Prince et al. 2015 [15])

2.1.1.2. T_2 RELAXATION

The transverse relaxation or ‘spin-spin’ relaxation is captured using an empirically determined proportionality constant T_2 . This relaxation of the transverse component is due to the fact that individual spins all experience a different local magnetic field due to other spins in its neighbourhood. As the Larmor frequency is dependent on the strength of the external field, this will cause a variation in precession frequency. The resulting dephasing causes the signal from the macroscopic magnetisation to decrease due to the loss of coherence. This situation is depicted in Figure 2.3. Introducing this damping of the transverse component in the equations of motion (2.9) the following expression is found:

$$\frac{d\vec{M}_\perp}{dt} = \gamma B_0 \vec{M}_\perp \times \hat{z} - \frac{1}{T_2} \vec{M}_\perp. \quad (2.11)$$

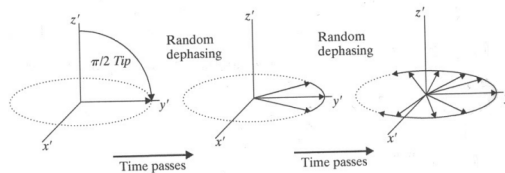


Figure 2.3: Impression of the transverse relaxation after a $\frac{\pi}{2}$ flip as seen from the rotating frame. The proportionality factor T_2 determines the rate of this process. (From: Prince et al. 2015 [15])

In practice the dephasing of the transverse component is stronger than suggested by the T_2 proportionality factor due to inhomogeneities in the B_0 field. The proportionality factor which also takes the dephasing due to inhomogeneities into account is referred to as T_2^* . This factor is not relevant for this research project as the used sequences are not sensitive to this parameter as discussed in [15].

2.1.1.3. FULL BLOCH EQUATIONS

If the Bloch equations for non-interacting spin systems from equation (2.9) is rewritten using the relaxation terms, the following result is found:

$$\frac{d\vec{M}}{dt} = \gamma B_0 \vec{M} \times \hat{z} - \frac{1}{T_2} \vec{M}_\perp + \frac{1}{T_1} (M_0 - M_z) \hat{z}. \quad (2.12)$$

This coupled differential equation can be solved by using a change of variables $M_x = m_x e^{\frac{t}{T_2}}$, $M_y = m_y e^{\frac{t}{T_2}}$ and $M_z = m_z e^{\frac{t}{T_1}}$:

$$\begin{aligned} \frac{dm_x}{dt} &= \gamma B_0 m_y \\ \frac{dm_y}{dt} &= -\gamma B_0 m_x \\ \frac{dm_z}{dt} &= \frac{M_0}{T_1} e^{\frac{t}{T_1}}. \end{aligned} \quad (2.13)$$

Solving the coupled equation for m_x is done by means of a substitution: $\frac{d^2 m_x}{dt^2} = \gamma B_0 \frac{dm_y}{dt}$. Using an equivalent substitution to solve for m_y and remembering the definition of the Larmor frequency $\omega_0 = \gamma B_0$, the following decoupled equations are found:

$$\begin{aligned} \frac{d^2 m_x}{dt^2} &= -\omega_0^2 m_x \\ \frac{d^2 m_y}{dt^2} &= -\omega_0^2 m_y. \end{aligned} \quad (2.14)$$

This decoupled system of differential equations is easily solved using the time at $t = 0$ as the initial condition resulting in:

$$\begin{aligned} M_x(t) &= e^{\frac{t}{T_2}} (M_x(0) \cos(\omega_0 t) + M_y(0) \sin(\omega_0 t)) \\ M_y(t) &= e^{\frac{t}{T_2}} (M_y(0) \cos(\omega_0 t) - M_x(0) \sin(\omega_0 t)) \\ M_z(t) &= M_0 + e^{\frac{t}{T_1}} (M_z(0) - M_0). \end{aligned} \quad (2.15)$$

Arbitrary phase shifts are omitted in this derivation, but will be introduced in chapter 3 in the context of undersampling errors. From the result in equation (2.15) it can be concluded that the longitudinal motion relaxes back to the equilibrium position with a rate determined by the proportionality constant T_1 and the transverse components rotate around the z -axis and relax with a rate determined by the proportionality constant T_2 .

2.1.2. SIGNAL MODEL

To understand how an MR scanner acquires information about the sample, the signal model is derived from first principles. It can be observed that the magnetisation vector introduced in last section is spatially dependent as it depends on tissue properties. The transverse part of the magnetisation is the quantity which is measured in an MRI scan. In this section the evolution of the magnetisation under imaging circumstances is substituted in the general signal model derived in Appendix C and the resulting MRI signal equation is presented. What ‘imaging circumstances’ are exactly will become clear in this section.

The transverse component of the magnetisation can be measured using the receive coils of the MR scanner. A schematic representation of the orientation of these coils is depicted in figure 2.4. Using Faraday’s law of induction the general signal model can be derived:

$$s(t) \propto emf = -\frac{d}{dt} \iiint_{\text{sample}} \vec{B}^{prod}(\vec{r}) \cdot \vec{M}(\vec{r}, t) d^3r, \quad (2.16)$$

where $s(t)$ is the signal from the detection coil induced by the magnetisation of the sample, $\vec{B}^{prod}(\vec{r}, t)$ is the field produced by one unit of current through this detection coil and $\vec{M}(\vec{r}, t)$ is the magnetisation in the sample that is spatially and temporally dependent. The proportionality factor depends on multiple factors e.g. the amplifier gain. The derivation of equation (2.16) from first principles can be found in Appendix C.

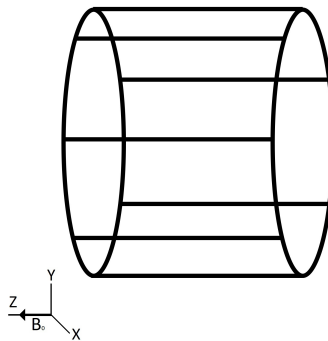


Figure 2.4: Type of Radio Frequency coil called bird cage coil. This transceiver coil is mainly used for brain imaging.

To model the signal from an MR scanner, a sample in a static, uniform \vec{B}_0 field is assumed which has been excited by some RF-pulse such that there is a transverse component to the macroscopic magnetisation. Slice selection as explained in Appendix B, is used to select a desired 2-dimensional plane by applying a magnetic field gradient. To obtain spatial information from the slice, additional gradients are required called readout gradients. They will cause the Larmor frequency to become spatially dependent within the slice, which is used to extract spatial information. When we note that the gradients can

be time dependent, we find $\omega(\vec{r}, t) = \omega_0 + \Delta\omega(\vec{r}, t)$. Note that $\omega_0 \gg \Delta\omega(\vec{r}, t)$ as the magnitude of the gradient is small compared to the static B_0 field. To understand how the spatial information within a slice is extracted, the MR signal is derived using the equations of motion from equation (2.15) which are substituted in the signal model from equation (2.16). It is convenient to introduce $M_+(\vec{r}, t) = M_x(\vec{r}, t) + M_y(\vec{r}, t) \cdot i$ as this will simplify keeping track of the rotation. As additional gradients in the x and y direction are taken into account, the Larmor frequency becomes dependent on space and time causing $\omega_0 t$ in equation (2.15) to be changed to $\int_0^t \omega(\vec{r}, t') dt'$. This results in:

$$s(t) \propto -\frac{d}{dt} \iiint_{\text{sample}} [B_x^{prod}(\vec{r}) \text{Re}(M_+(\vec{r}, 0) e^{-i \int_0^t \omega(\vec{r}, t') dt' + \frac{t}{T_2}}) + B_y^{prod}(\vec{r}) \text{Im}(M_+(\vec{r}, 0) e^{-i \int_0^t \omega(\vec{r}, t') dt' + \frac{t}{T_2}}) + B_z^{prod}(\vec{r}) M_z(t)] d^3 r. \quad (2.17)$$

As the appropriate smoothness conditions are satisfied, the derivative can be taken inside the integrand and the Re and Im operators. Noting that $\frac{1}{T_1}$ and $\frac{1}{T_2}$ are at least four orders-of-magnitude smaller than $\omega(\vec{r})$, the derivatives of the factors $e^{\frac{t}{T_1}}$ and $e^{\frac{t}{T_2}}$ can be neglected [13] as well as the derivative of the slowly changing $M_z(t)$. If $B_-^{prod} = B_x^{prod} - B_y^{prod} i$ and the definition of $\omega(\vec{r}, t)$ is taken into account, equation (2.17) can be rewritten into:

$$s(t) \propto \iiint_{\text{sample}} \omega(\vec{r}, t) \text{Re}(i e^{-i\omega_0 t} B_-^{prod}(\vec{r}) M_+(\vec{r}, 0) e^{-i \int_0^t \Delta\omega(\vec{r}, t') dt' + \frac{t}{T_2}}) d^3 r. \quad (2.18)$$

A demodulation step of the signal is applied to filter the high frequency component introduced by $e^{-i\omega_0 t}$. The demodulation is performed by multiplication with a time dependent function with frequency ω_0 and a low-pass filtering step. By considering a multiplication with $\sin(\omega_0 t)$ as well as $-\cos(\omega_0 t)$, two different demodulated signals are found which are referred to as the signals from the 'real' and 'imaginary' channels respectively. The signal from both these channels gives information about the original signal. A detailed description of the demodulation process can be found in [13]. The resulting complex signal after demodulation is:

$$s(t) \propto \iiint_{\text{sample}} \omega(\vec{r}, t) B_-^{prod}(\vec{r}) M_+(\vec{r}, 0) e^{-i \int_0^t \Delta\omega(\vec{r}, t') dt' + \frac{t}{T_2}} d^3 r. \quad (2.19)$$

Note that for spatially constant gradients $\int_0^t \Delta\omega(\vec{r}, t') dt' = \gamma(\int_0^t G_x(t') dt' \cdot x + \int_0^t G_y(t') dt' \cdot y)$. A few approximations to the equation above results in an expression which clarifies how spatial information is extracted using the signal from the encoded sample. Note that $\Delta\omega(\vec{r}, t) \ll \omega_0$ such that $\omega(\vec{r}, t) \approx \omega_0$ for the first term in equation (2.19). The receiving coils can be approximated as sufficiently uniform such that $B_-^{prod}(\vec{r}) = B_-^{prod}$. Finally, the signal is acquired directly after the excitation such that the damping factor: $e^{\frac{t}{T_2}}$ can be neglected. Taking all these approximations into account the following result obtained:

$$s(t) \propto \Delta z \omega_0 B_-^{prod} \iint_{\text{slice}} M_+(\vec{r}, 0) e^{-i\gamma(\int_0^t G_x(t') dt' \cdot x + \int_0^t G_y(t') dt' \cdot y)} dx dy, \quad (2.20)$$

where Δz is the width of the slice in the z direction. Defining the Fourier transform of a function $f(x,y)$ as:

$$\mathcal{F}(u, v) = \iint f(x, y) e^{-i(ux+vy)} dx dy, \quad (2.21)$$

it can be observed that equation (2.20) relates to the 2D-Fourier transform of the transverse magnetisation $M_+(\vec{r}, 0)$:

$$\mathcal{F}\left(\gamma \int_0^t G_x(t') dt', \gamma \int_0^t G_y(t') dt'\right) = \iint M_+(\vec{r}, 0) e^{-i\gamma(\int_0^t G_x(t') dt' \cdot x + \int_0^t G_y(t') dt' \cdot y)} dx dy \propto s(t). \quad (2.22)$$

By measuring the signal from the MR scanner, k-space information of the function $M_+(\vec{r}, 0)$ along the line set out by the readout gradient is obtained. The k-space sampling can be performed in a radial manner as depicted in figure 2.5a, but generally in MR fingerprinting the sampling is performed using a spiral trajectory (figure 2.5b). To find the original image with the information about the transverse magnetisation, an inverse Fourier transform is performed.

The sequence of acquisition parameters such as flip angles resulting from the RF-pulses, the time in between these pulses (Repetition time; TR) and the time from the RF-pulse to the k-space readout (Echo time; TE) are part of the so called pulse sequence which determines the evolution of the signal. In the next section the pulse sequence used in this research project is discussed.

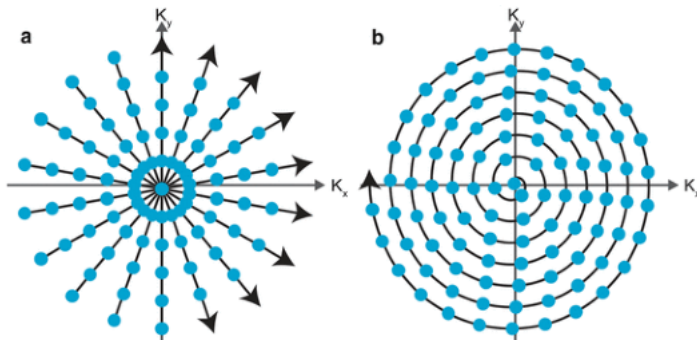


Figure 2.5: Different k-space sampling trajectories. a) Radial sampling, b) Spiral sampling. The blue dots represent the points in k-space where a readout is performed (the MR signal is measured) and the arrows show in which direction the information is gathered. (Modified from: Loecher et al. 2015 [16])

2.2. GRADIENT-SPOILED SSFP SEQUENCES

The pulse sequence used in this research project is called gradient-spoiled Steady-State Free Precession (SSFP) or non-balanced SSFP and makes use of gradient and spin-echos. To understand what a gradient echo is, a string of isochromats in one voxel is considered, in presence of a (slice selection) gradient. As the Larmor frequency is varying in the z -direction, the isochromats start to dephase as is depicted in figure 2.6a. This dephasing obliterates the coherence of the spin ensembles, resulting in the loss of signal from this voxel. To revive the signal, a refocusing gradient with the opposite polarity can be applied, which restores the coherence as the isochromats with the highest Larmor frequency during the dephasing, will now have the lowest frequency which rephases the spin ensembles in the voxel as is depicted in figure 2.6b.

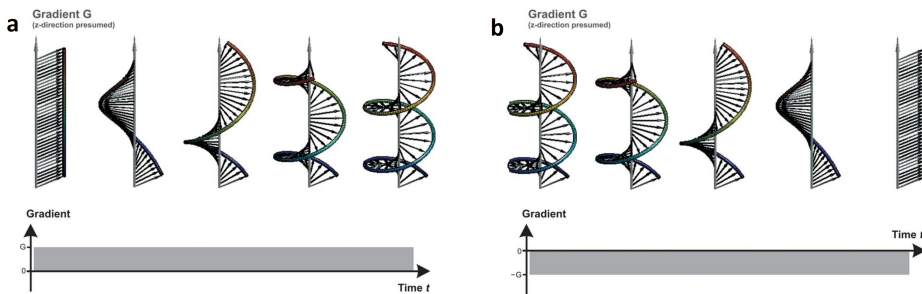


Figure 2.6: Gradient echo. a) Dephasing of spin ensembles in one voxel due to a slice selection gradient. b) Rephasing of spin ensembles in one voxel due to a refocusing gradient. (Modified from: Weigel. 2015 [17])

Just as the gradient-echo, the spin-echo triggers rephasing after signal loss due to dephasing of the spin ensembles. A spin-echo is caused by playing a flip angle pulse after dephasing of the spin ensembles, which allows the system to rephase back after the flip. To explain this, a simple example situation where the spins are in equilibrium is considered and sketched in Figure 2.7. By rotating the spins with an angle $\alpha = \frac{\pi}{2}$ the macroscopic magnetisation enters the transverse plane. Here dephasing takes place due to applied gradients or inhomogeneities in the magnetic B_0 field. By applying a flip angle around the x' -axis with $\alpha = \pi$ as depicted in the figure, the magnetisation from the spin ensembles get mirrored. Spin ensembles which were lagging behind as they move with a Larmor frequency lower than the frequency of the rotating frame are now leading as can be seen in figure 2.7d. As the position of the spins did not alter, their Larmor frequency is still lower than the frequency of the rotating frame resulting in the spins moving to the negative y' axis. The result is the formation of a coherent echo at the negative y' axis. When the flip angle is not $\alpha = \pi$ but an arbitrary angle, the situation becomes less intuitive as a part of the dephased signal ends up in the longitudinal direction. Although the principles remain the same, one should carefully keep track of the different dephasing modes, in order not to miss any echos. Section 2.2.2.4 will sketch how the administration of the dephasing modes is performed.

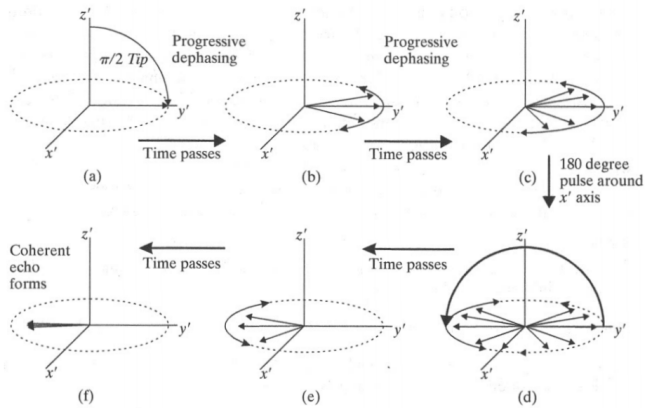


Figure 2.7: Formation of a spin-echo. The RF pulse which causes the π flip, causes the spins to rephase again. (From: Prince et al. 2015 [15])

For MR Fingerprinting, a sequence of system readouts is required, which is obtained using the gradient-spoiled SSFP pulse sequence. This sequence starts with an adiabatic inversion pulse, which causes an inversion of the spin states for the entire sample. After this inversion, single RF-pulses are used to manipulate the macroscopic magnetisation by causing a flip with a certain angle α . An example of a flip angle pattern used in this research project is shown in figure 2.8b. The RF-pulses are modelled as instantaneous rotations (hard pulse approximation). Right before the single RF-pulses are sent the slice selection gradient is turned on, causing dephasing in the z direction. The slice selection gradient after the pulse is balanced to maintain coherence. After the excitation pulse has been applied, the readout takes place using a spiral sampling pattern as in figure 2.8c. The spiral is rotated every repetition to assure that the k -space is efficiently sampled. The spiral is zero moment compensated to prevent dephasing in the x and y direction.

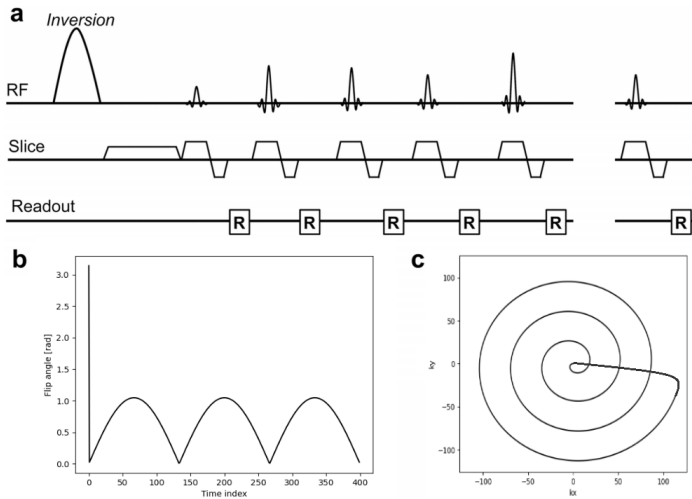


Figure 2.8: SSFP pulse sequence with a conventional FA sequence. a) A pulse sequence diagram of a gradient-spoiled SSFP sequence in the MRF framework. The sequence starts with an adiabatic inversion pulse and is followed by a series of RF pulses introducing certain flip angles as depicted in part b of this image. The slice-selection gradients are unbalanced in this acquisition. b) A sinusoidal flip angle pattern that is generally used. c) One interleaf of a spiral is used for each readout. The spiral is zero moment compensated. To fully sample k -space, the spiral rotates every every step with 11.25 degrees resulting in 32 different spiral trajectories for a 225×225 image. (Modified from: Jiang et al. 2015 [18])

Since the early 2000s it is possible to balance the slice selection gradient to achieve balanced SSFP [19]. This acquisition method generally has a higher signal to noise ration than gradient-spoiled SSFP as there are no dephasing modes. However, this also makes the sequence prone to errors due to field inhomogeneities causing so called banding artefacts. This is why we, like most studies, opted to use gradient-spoiled SSFP sequence.

2.2.1. EXTENDED PHASE GRAPHS

There are two widely used methods to simulate the behaviour of spins during an MRI sequence. The first is called the ‘isochromat summation’ approach, which is a brute force method where the evolution of multiple spin ensembles with different Larmor frequencies are followed through time. The vector sum of all the simulated isochromats determines the resulting signal. To obtain an accurate result, thousands of isochromats are typically required, making the method computationally very demanding. The second method is called the ‘extended phase graph’ approach (EPG) which is more elegant [17].

Individual isochromats are described using a Cartesian basis:

$$\vec{M}(\vec{r}) = \begin{bmatrix} M_x(\vec{r}) \\ M_y(\vec{r}) \\ M_z(\vec{r}) \end{bmatrix}. \quad (2.23)$$

Instead of focusing on the evolution of individual isochromats, it is more efficient to keep track of the configuration states of an ensemble of isochromats [17]. Configuration states are directly linked to the Fourier transform of the magnetisation and describe different levels of dephasing. For this approach, a change from the Cartesian basis to a complex basis is introduced:

$$\vec{M}(\vec{r}) \equiv \begin{bmatrix} M_+(\vec{r}) \\ M_-(\vec{r}) \\ M_z(\vec{r}) \end{bmatrix} = \begin{bmatrix} 1 & i & 0 \\ 1 & -i & 0 \\ 0 & 0 & 1 \end{bmatrix} \vec{M}(\vec{r}), \quad (2.24)$$

where the matrix left of the Cartesian representation is referred to as the S-matrix. In the configuration state space \vec{F} , the dephasing is quantified by taking the Fourier transform of the spatially dependent complex magnetisation vector from equation (2.24) in a voxel with volume V :

$$\vec{F}(\vec{k}) \equiv \begin{bmatrix} \tilde{F}_+(\vec{k}) \\ \tilde{F}_-(\vec{k}) \\ \tilde{Z}(\vec{k}) \end{bmatrix} = \begin{bmatrix} \iiint_V M_+(\vec{r}) e^{-i\vec{k}\cdot\vec{r}} d\vec{r} \\ \iiint_V M_-(\vec{r}) e^{-i\vec{k}\cdot\vec{r}} d\vec{r} \\ \iiint_V M_z(\vec{r}) e^{-i\vec{k}\cdot\vec{r}} d\vec{r} \end{bmatrix}. \quad (2.25)$$

A 3-dimensional approach would be necessary to model an experiment with multiple dephasing directions or with anisotropic diffusion effects [20]. In this study however, it is assumed that effective dephasing only occurs in one direction such that, instead of the vectors \vec{r} and \vec{k} , the scalars r and k suffice. We assume without loss of generality that the amount of dephasing introduced during one repetition time is the same for all time indices. The dephasing states are the discrete configuration states $\tilde{F}_+(k)$, with integer $k > 0$. Without loss of generality we assume that the dephasing introduced during one time index, corresponds to a unit step in the discrete configuration states. Note that $M_+ = M_-^*$ such that $\tilde{F}_+(-k) = \tilde{F}_-^*(k)$. If the M_+ representation of the magnetisation rotates in the clockwise direction, the M_- representation rotates counter clockwise. For this reason, integer values $k > 0$ of the Fourier transform of $M_-(\vec{r})$ are referred to as the rephasing states. The dephasing and rephasing states are shown in the top and middle row of figure 2.9 respectively, where the dephasing level k is presented as subscript and the ‘+’ and ‘-’

are denoted as a superscript for readability purposes. This notation will be used from now on. When the axis with respect to which the flip angle is performed is constant, and the initial magnetisation is in the equilibrium position, all echos are generated on the same axis in the x', y' -plane. This situation is referred to as in-phase refocusing. Because the longitudinal magnetisation is real, it can be constructed using discrete real harmonics build from complex harmonic functions with opposite rotation as shown in the last row of figure 2.9.

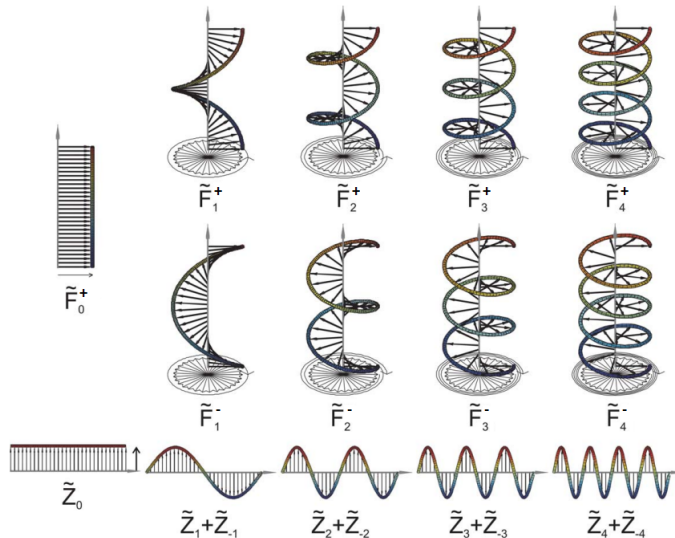


Figure 2.9: Graphical representation of discrete configuration states used in the EPG framework. The \tilde{F}_0^+ state represents the coherent part of the magnetisation, yielding a measurable signal. \tilde{F}^+ and \tilde{F}^- -states with a non-zero index cannot be measured as their configuration is such that the net magnetisation is destroyed. The top row with $k > 0$ shows the dephasing configurations, while the middle row with $k < 0$ represents the corresponding rephasing configurations which are rotated in the other direction. The longitudinal components are made up of identical complex configuration rotating in opposite directions. (Modified from: Weigel, 2015 [17])

The weighting of the configuration states is stored in a state matrix. This matrix contains all the information to describe the complete ensemble magnetisation and is denoted as:

$$\Omega = \begin{bmatrix} \tilde{F}_0^+ & \tilde{F}_1^+ & \tilde{F}_2^+ & \tilde{F}_3^+ & \dots \\ \tilde{F}_0^- & \tilde{F}_1^- & \tilde{F}_2^- & \tilde{F}_3^- & \dots \\ \tilde{Z}_0 & \tilde{Z}_1 & \tilde{Z}_2 & \tilde{Z}_3 & \dots \end{bmatrix}. \quad (2.26)$$

Column k in this matrix contains the information to fully describe the k th dephasing order of the total magnetisation. How the gradient-spoiled SSFP sequence is modelled, is discussed in section 2.2.2.4. Note that only \tilde{F}_0^+ and \tilde{F}_0^- represent a detectable coherent state while all other \tilde{F}_k^+ and \tilde{F}_k^- states with $k \neq 0$ are fully dephased i.e. do not yield a measurable signal.

2.2.2. MODELLING THE GRADIENT-SPOILED SSFP SEQUENCE

The modelling of the gradient-spoiled SSFP sequence is performed using the EPG framework introduced in section 2.2.1. How basic operations on the macroscopic magnetisation are modelled in the EPG framework can be derived by looking at these operations on a single isochromat using a Cartesian basis. The operations of interest to model a gradient-spoiled SSFP sequence are RF pulse induced rotations, relaxation and dephasing.

2.2.2.1. RF PULSE

An RF-pulse induced rotation of the magnetisation with a flip angle α can be modelled in the EPG framework by looking at this operation on a single isochromat using a Cartesian basis. The effect of an RF-pulse on a single isochromat at position \vec{r} in a voxel can be modelled using the elemental rotation matrix around the x' -axis:

$$R_x(\alpha) = \begin{bmatrix} 1 & 0 & 0 \\ 0 & \cos(\alpha) & -\sin(\alpha) \\ 0 & \sin(\alpha) & \cos(\alpha) \end{bmatrix}. \quad (2.27)$$

The result is: $\vec{M}(\vec{r})^\dagger = R_x(\alpha)\vec{M}(\vec{r})^\downarrow$ where the superscript \downarrow and \uparrow mark the magnetisation of the isochromat before and after the manipulation respectively. Notice that the RF-pulse induced rotation is assumed to be instantaneous (hard pulse approximation). To understand how this rotation is applied in configuration state space, it is noted that: $\vec{F} = \mathcal{F}(\vec{M})$. As the Fourier transform is a linear operator, a rotation in configuration state space is the same as rotating the complex vector \vec{M} . This can be denoted as: $\tilde{R}_x(\alpha)\mathcal{F}(\vec{M}) = \mathcal{F}(\tilde{R}_x(\alpha)\vec{M})$ where \tilde{R}_x is the rotation in the complex basis. Using the definition $\vec{M} = S\vec{M}$, it can be derived that the rotation matrix for the complex basis and thus for configuration state space is $\tilde{R}_x(\alpha) = SR_x(\alpha)S^{-1}$:

$$\tilde{R}_x(\alpha) = \begin{bmatrix} \cos^2(\frac{\alpha}{2}) & \sin^2(\frac{\alpha}{2}) & -i \sin(\alpha) \\ \sin^2(\frac{\alpha}{2}) & \cos^2(\frac{\alpha}{2}) & i \sin(\alpha) \\ -\frac{i}{2} \sin(\alpha) & \frac{i}{2} \sin(\alpha) & \cos(\alpha) \end{bmatrix}. \quad (2.28)$$

As the off-diagonal elements are generally non-zero, the application of an RF-pulse introduces mixing between different configuration states. Using the state matrix, the application of an RF-pulse induced rotation is modelled as follows:

$$\Omega^\dagger = \tilde{R}_x(\alpha)\Omega^\downarrow. \quad (2.29)$$

2.2.2.2. RELAXATION EFFECTS

Using a similar approach, relaxation effects can be modelled in the EPG framework by looking at this operation on single isochromats in the Cartesian basis. The relaxation matrix for a single isochromat using the Cartesian basis at position \vec{r} is:

$$E(t, T_1, T_2) = \begin{bmatrix} e^{-\frac{t}{T_2}} & 0 & 0 \\ 0 & e^{-\frac{t}{T_2}} & 0 \\ 0 & 0 & e^{-\frac{t}{T_1}} \end{bmatrix} \quad (2.30)$$

where the recovery toward the equilibrium is not yet incorporated. For the same reasons as in section 2.2.2.1, the relaxation matrix for the configuration state space is: $\bar{E}(t, T_1, T_2) = SE(t, T_1, T_2)S^{-1} = E(t, T_1, T_2)$ as E is a diagonal matrix.

Using the state matrix, the relaxation effects are modelled as follows:

$$\Omega^\dagger = E(t, T_1, T_2)\Omega^\dagger + \begin{bmatrix} 0 & 0 & \dots \\ 0 & 0 & \dots \\ M_0(1 - e^{-\frac{t}{T_1}}) & 0 & \dots \end{bmatrix}. \quad (2.31)$$

where the recovery toward the thermal equilibrium is modelled using the last term on the right hand side, also denoted as $M_0(1 - e^{-\frac{t}{T_1}})e_{2,1}$. Here $e_{3,1}$ is a matrix with the same dimensions as the state matrix, and all entries 0 except for the entry (2, 1) which is 1. The longitudinal recovery increases the coherent magnetisation in the z -direction, thus \tilde{Z}_0 is the only state matrix entry which is influenced by this process.

2.2.2.3. DEPHASING EFFECTS

Dephasing of the magnetisation can be modelled in the EPG framework using the shift operator D . As the EPG concept is build using dephasing states, the dephasing effects caused by gradients or time-independent inhomogeneities in the magnetic field can be described in a simple way [17]:

$$D(\Omega) : \begin{cases} \tilde{F}_k^+ \rightarrow \tilde{F}_{k+1}^+ \\ \tilde{F}_k^- \rightarrow \tilde{F}_{k-1}^- \\ \tilde{Z}_k \rightarrow \tilde{Z}_k \end{cases} \quad k > 0 \quad \text{and} \quad D(\Omega) : \begin{cases} \tilde{F}_0^+ \rightarrow \tilde{F}_1^+ \\ (\tilde{F}_1^-)^* \rightarrow \tilde{F}_0^+ \\ \tilde{Z}_0 \rightarrow \tilde{Z}_0 \end{cases} \quad (2.32)$$

where k are integers. Notice that only the transverse F^+ and F^- states are influenced by dephasing, whereas the longitudinal states are not. The $k < 0$ states are of no interest because of the redundancy pointed out in section 2.2.1: $\tilde{F}_{-k}^+ = (F_k^-)^*$ and the fact that the longitudinal component M_z is real resulting in: $\tilde{Z}_{-k} = (\tilde{Z}_k)^*$.

2.2.2.4. GRADIENT-SPOILED SSFP MODEL

Manipulation of the transverse magnetisation in a voxel while applying a gradient-spoiled SSFP sequence is modelled by calculating the time evolution of the state matrix Ω_n using the manipulations discussed above. The subscript n denotes the time index. The flip angle patterns used in this research project, all start with an inversion pulse. The angles are defined as rotations around the x -axis. For the experiments in this research project the repetition time is fixed at 15 ms and the echo time at 4 ms. To simplify the model, the echo time is approximated as 0 ms, meaning that the transverse magnetisation readout is performed directly after application of the excitation pulse. Using Ω_{-1} to denote the system in thermal equilibrium, the first readout after the inversion pulse is modelled as:

$$\Omega_0 = \tilde{R}_x(\pi)\Omega_{-1}. \quad (2.33)$$

Assuming the state matrix at time index n is known, the magnetisation should be manipulated to achieve the state matrix at time index $n + 1$. The physical processes relaxation, dephasing and the application of RF-pulses between the magnetisation states at time

index n and $n + 1$ are discussed. After the readout at time index n , the system starts to relax. Before the next flip angle is played the slice selection gradient causes dephasing. Noting that the relaxation operator and the dephasing operator commute the following result is found:

$$\Omega_{n+1} = \bar{R}_x(\alpha) \left(E(TR, T_1, T_2) D(\Omega_n) + M_0 (1 - e^{-\frac{T}{T_1}}) e_{2,1} \right) \quad (2.34)$$

As F_0^+ is the only coherent dephasing configuration, this state represents the measurable transverse magnetisation and is used as the MRF signal in image space:

$$M_+ = F_0^+. \quad (2.35)$$

2.3. MAGNETIC RESONANCE FINGERPRINTING

Magnetic Resonance Fingerprinting (MRF) [3] is a relatively new approach to quantitative MRI that allows simultaneous measurement of multiple different tissue maps in a single acquisition. It offers a flexible framework in which freely chosen acquisition parameters are used to probe the transient-state signal evolution. The set of acquisition parameters chosen for the MRF scan, result in a unique signal evolution or ‘fingerprint’, of a certain tissue. This unique signal encodes for a certain set of tissue parameters of interest. The measured signals are matched to a pre-computed dictionary that contains generated fingerprints for a range of different tissue properties. These fingerprints are simulated (using EPG in this project) for the acquisition parameters used in the scan. A pattern matching algorithm subsequently finds the quantitative tissue parameters corresponding to the measured signal, by comparing it with the dictionary signals. Figure 2.10 shows a schematic overview of the MRF framework. Usually in MRF, inner product matching is applied using a normalised dictionary. The dictionary atom which has the highest inner product with the measured signal is selected for the resulting parameter maps. Using this approach, multiple inherently registered quantitative tissue maps are generated using one acquisition.

Using multiple k-space readouts performed at different times during the transient-state signal evolution, the fingerprint from a single voxel can be acquired. These k-space acquisitions are significantly undersampled (only 1/48 of the full k-space was acquired for each time point in the original work [3]) to achieve speed-ups in scan duration, resulting in quantitative maps in a clinically feasible time. In this project spiral sampling patterns are used for the acquisition. The undersampling causes severe artefacts in the images for each individual time point. Despite the undersampling, the signals from a single voxel can still be matched to the corresponding dictionary entry. This results in accurate quantitative maps, although these reconstructions can still contain undersampling errors as discussed in section 2.6.

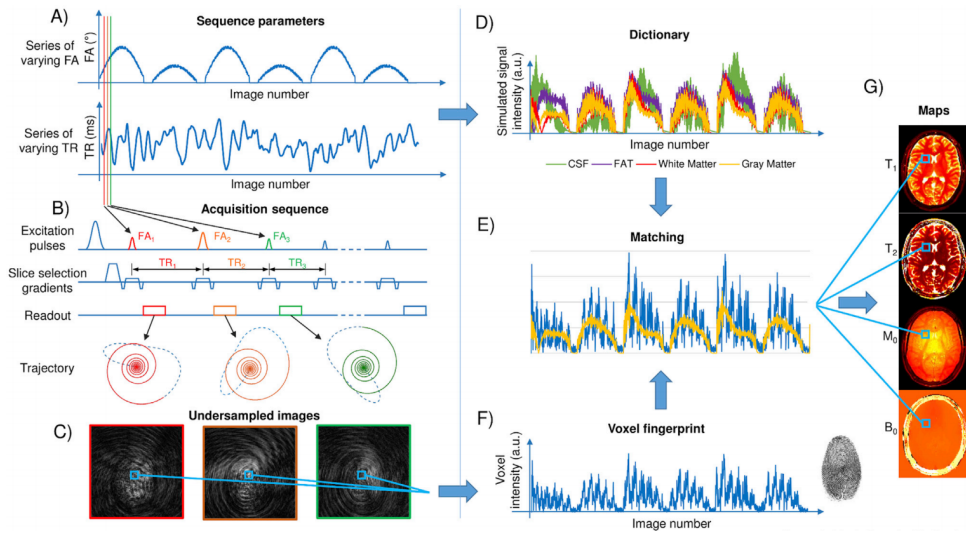


Figure 2.10: Schematic overview of the MRF framework. A) Example of the acquisition parameters for the flip angles and repetition times. B) Sequence diagram showing the excitation pulses, slice selection gradients, read-out and k-space trajectories for 3 different time indices. C) Example of three undersampled images at three different time points. D) Example of 4 dictionary atoms. E) Pattern matching of the measured voxel fingerprint with the closest element in the dictionary. F) Measured signal from a voxel across the undersampled images. G) Parameter maps obtained from repeating the dictionary matching process for each voxel. (from: Panda et al. 2017 [5]).

2.4. THE MULTI-COMPONENT SETTING

Straight-forward dictionary matching based on minimisation of the inner product assumes that every voxel contains merely one type of tissue. This assumption breaks down if a voxel is on the border of two neighbouring tissues or when multiple tissues are diffusely merged. An example of the latter situation is the case of myelin and white matter. The myelin fraction is an interesting parameter in progressive diseases such as multiple sclerosis. As it is hard to image myelin directly, myelin water serves as a bio marker for myelin alterations and its tissue properties will be used in this research project [21]. If single-component matching is performed when the measured signal actually comes from multiple tissues, this results in so called partial volume effects that degrade the image quality. Multi-component (MC) analysis takes into account that one voxel can contain multiple tissues and assumes that the measured signal is composed of a weighted sum of the signals from the separate tissues in a voxel. One of the most basic approaches to separate the multi-component signal is using the Non-Negative Least Squares (NNLS) algorithm [22]. This algorithm matches the measured signal to a weighted sum of dictionary signals using a least-squares approximation, where the constraint is added that the weights cannot have a non-physical negative value. There exist more advanced algorithms that also promote sparsity in the set of dictionary atoms that are selected to match the measured signals. One example of such algorithm is SPIJN [7] that introduces a joint sparsity constraint to minimise the total amount of different dictionary atoms for all image voxels.

The simplest signal model in a multi-component setting is an addition of the individual signals:

$$M_{\text{multi}}(\boldsymbol{\theta}) = \sum_{n=1}^{N_T} M(\boldsymbol{\theta}^n), \quad (2.36)$$

where M_{multi} is the measured transverse magnetisation from the voxel, $\boldsymbol{\theta}$ is a vector with the tissue parameters for all the tissues, $\boldsymbol{\theta}^x$ is a vector with the tissue parameters for tissue type x and N_T is the total amount of different tissues in the voxel. Note that the volume fractions follow from the proton densities $\rho^x \in \boldsymbol{\theta}^x$ of the different tissue types. In a multi-component voxel magnetisation exchange might influence the measured signal. This influence can be such that the approximation in equation (2.36) might break down. The EPG framework can be extended to model magnetisation exchange as well [23]. For this research project we opted to model the MC voxel as a nonexchanging system under the assumption that the exchange effects for brain tissues are too small to significantly influence the results.

2.5. CRAMÉR-RAO LOWER BOUND

MR signals suffer from stochastic noise from various sources e.g. thermal noise from the subject itself and electronic noise from stochastic motion of free electrons in the coils. When dealing with in-phase refocusing, where all echos are generated on the same axis in the x', y' -plane, the general signal model can be approximated as:

$$s_j(\boldsymbol{\theta}) = M_j(\boldsymbol{\theta}) + \varepsilon_j e^{i\phi} \quad j = 1, 2, \dots, N_j \quad (2.37)$$

where s_j is the measured signal, M_j is the transverse magnetisation without noise, ε_j is independent identically distributed Gaussian noise with mean 0 and variance σ^2 , j is the time index and ϕ is the phase of the in-phase refocusing axis. Note that noise perpendicular to the in-phase axis could be added, but if the dictionary signals have the same phase as the measured signal, adding this extra noise term would make later evaluations computationally more expensive whilst not altering the results. This was confirmed by a short numerical study. The Cramér-Rao Lower Bound (CRLB) is an estimation theoretic inequality which provides a lower bound on the covariance of any unbiased estimator under mild regularity conditions. It is derived using the Cauchy-Schwarz inequality [24]. Mathematically the CRLB inequality is expressed as:

$$\mathbb{E}[(\hat{\boldsymbol{\theta}} - \boldsymbol{\theta})(\hat{\boldsymbol{\theta}} - \boldsymbol{\theta})^T] \geq \mathbf{N}^{-1}(\boldsymbol{\theta}), \quad (2.38)$$

where $\boldsymbol{\theta}$ are the unknown tissue specific parameters in an MRF experiment (e.g. T_1 , T_2 and proton density) and $\hat{\boldsymbol{\theta}}$ are the unbiased estimators for these parameters. Note that the left hand side of this equation is the covariance matrix of the estimators $\hat{\boldsymbol{\theta}}$. The matrix \mathbf{N} denotes the Fisher Information Matrix (FIM) defined as:

$$N_{p,q}(\boldsymbol{\theta}) = \mathbb{E} \left[\left(\frac{\partial \ln(p(\mathbf{s}; \boldsymbol{\theta}))}{\partial \theta_p} \right) \left(\frac{\partial \ln(p(\mathbf{s}; \boldsymbol{\theta}))}{\partial \theta_q} \right) \right] \quad (2.39)$$

where p is the probability density function of the stochastic signal \mathbf{s} . This stochastic signal is an $N_j \times 1$ vector. The matrix inequality from equation (2.38) is defined as $\mathbb{E}[(\hat{\boldsymbol{\theta}} - \boldsymbol{\theta})(\hat{\boldsymbol{\theta}} - \boldsymbol{\theta})^T] - \mathbf{N}^{-1}$ being positive semidefinite. Using the definition of positive semidefinite, it is trivial to extract the lower bound on the variance of unbiased individual tissue parameter estimates by matching it to the corresponding diagonal dictionary entry:

$$\text{Var}[\hat{\theta}_i] \geq N_{i,i}^{-1}. \quad (2.40)$$

These diagonal entries of the inverse FIM will be used for the numerical optimisations in section 3.3.

2.6. UNDERSAMPLING ERROR

MR Fingerprinting allows for the use of highly undersampled images for the construction of a quantitative maps. The use of undersampled images results in significant speed-ups in acquisition time as only a small portion of k-space has to be sampled. A direct result of using undersampled images is the presence of significant undersampling artefacts. A comprehensive model of the undersampling error is presented by *C.C. Stolk* and *A. Sbrizzi* [8]. I will use their ideas as the basis for a model which is applied to simulate the undersampling artefacts in the quantitative maps resulting from an MRF scan. As explored in the next sections, these key ideas are: (1) rewriting the mathematical expression for the undersampled signal using convolution; (2) modelling dictionary matching using the expression for a stationary point; (3) applying perturbation theory. Extensions to this model made by this author concerning thermal noise and the transmit phase are discussed in chapter 3.

2.6.1. SIGNAL MODEL FOR UNDERSAMPLED K-SPACE ACQUISITION USING CONVOLUTION

To model the undersampled images used in MRF, the expression for the undersampled images is rewritten using convolution. The spatial image domain is discretised using a rectangular mesh G_p of size $m_1 \times m_2$ with grid spacing 1 (it is assumed that both m_1 and m_2 are uneven) which is defined as:

$$G_p = \left\{ -\left\lfloor \frac{m_1}{2} \right\rfloor, -\left\lfloor \frac{m_1}{2} \right\rfloor + 1, \dots, 0, \dots, \left\lfloor \frac{m_1}{2} \right\rfloor \right\} \times \left\{ -\left\lfloor \frac{m_2}{2} \right\rfloor, -\left\lfloor \frac{m_2}{2} \right\rfloor + 1, \dots, 0, \dots, \left\lfloor \frac{m_2}{2} \right\rfloor \right\}. \quad (2.41)$$

A position in this grid is denoted by $\vec{x} = (x_1, x_2)$. The acquisition parameters such as flip angle, transmit phase and the repetition times (respectively: α , ϕ and T_R) are denoted with the vector ξ . The tissue parameters are denoted with the vector $\theta(\vec{x})$ with dimension N_θ . The undersampled images from which the quantitative maps are constructed are indexed with $j \in \{1, 2, \dots, N_j\}$. The full k-space data can be calculated by using the discrete Fourier transform of the transverse magnetisation M_j :

$$s_j(\vec{k}) = \sum_{\vec{x} \in G_p} M_j(\theta(\vec{x}); \xi) e^{-i\vec{k} \cdot \vec{x}}. \quad (2.42)$$

Notice that the complex notation of the transverse magnetisation was denoted as M_+ in section 2.1, but the subscript '+' will be dropped for readability. The vector $\mathbf{M}(\theta(\vec{x})) = (M_1(\theta(\vec{x})), M_2(\theta(\vec{x})), \dots, M_{N_j}(\theta(\vec{x})))$ is defined which contains information about the evolution of the transverse magnetisation of one pixel in the absence of errors. In this research project a spiral sampling pattern is used to generate the undersampled images. The l -th location in k-space which is sampled for the j -th undersampled image is denoted as $\vec{k}_{j,l}$ and $l \in \{1, 2, \dots, N_L\}$. As the images in MRF are highly undersampled the following inequality holds: $N_l \ll m_1 \cdot m_2$.

Using the k-space data $s_j(\vec{k}_{j,l})$, undersampled images $I_j(\vec{x})$ can be constructed by ap-

plying the discrete inverse Fourier transform:

$$I_j(\vec{x}) = \frac{1}{m_1 m_2} \sum_{l=1}^{N_l} w_{j,l} s_j(\vec{k}_{j,l}) e^{i\vec{k}_{j,l} \cdot \vec{x}}, \quad (2.43)$$

where $k_{j,l} \in [-\pi, \pi]^2$ due to the unit spacing of the grid G_p and $w_{j,l}$ are density compensation weights. The undersampled images $I_j(\vec{x})$ are used for the dictionary matching as explained in section 2.3.

The density compensation weights compensate for the fact that the sampling is performed on a non-Cartesian grid. For spiral sampling they are defined as follows [25]:

$$w_{j,l} = \begin{cases} 0 & \text{if } l = 1 \\ |\vec{k}_{j,l}| \cdot \|\vec{k}_{j,l}\| - \|\vec{k}_{j,l-1}\| & \text{if } l > 1 \end{cases} \quad (2.44)$$

These weights are intuitive for spiral sampling as $w_{j,l}$ is an estimation for the Jacobian when sampling space is divided into rings.

Substituting equation (2.42) into equation (2.43) yields the following expression:

$$I_j(\vec{x}) = \frac{1}{m_1 m_2} \sum_{l=1}^{N_l} \sum_{\vec{y} \in G_p} w_{j,l} M_j(\boldsymbol{\theta}(\vec{y}); \boldsymbol{\xi}) e^{i\vec{k}_{j,l} \cdot (\vec{x} - \vec{y})}. \quad (2.45)$$

This equations presents the undersampled image $I_j(\vec{x})$ as a function of the transverse magnetisation. From this equation a Point Spread Function (PSF) is extracted:

$$P_j(\vec{x}) = \frac{1}{m_1 m_2} \sum_{l=1}^{N_l} w_{j,l} e^{i\vec{k}_{j,l} \cdot \vec{x}}, \quad (2.46)$$

such that equation (2.45) can be rewritten as a convolution sum:

$$I_j(\vec{x}) = \sum_{\vec{y} \in G_p} P_j(\vec{x} - \vec{y}) M_j(\boldsymbol{\theta}(\vec{y}); \boldsymbol{\xi}). \quad (2.47)$$

Note that the PSF is time dependent trough the index j . We define $\mathbf{I}(\vec{x}) = (I_1(\vec{x}), I_2(\vec{x}), \dots, I_{N_j}(\vec{x}))$, which contains information about the evolution of the undersampled transverse magnetisation. This vector \mathbf{I} can be conceived as the signal detected by the scanner if all other error sources were ignored. Notice that the PSF should be defined on an extended grid for equation (2.45) and (2.47) to be mathematically equivalent. The dimensions of the extended grid are $(2m_1 - 1) \times (2m_2 - 1)$. Equation (2.46) can be evaluated explicitly for problems with few samples in k-space. For problems with a realistic amount of k-space samples an efficient implementation using the Non-Uniform Fast Fourier Transform (NUFFT) is used, which improves the calculation time with several orders of magnitude.

For k-space read-outs conforming to the Nyquist sampling ratio, the PSF function P_j becomes a Kronecker delta-peak. For undersampled MRF read-outs P_j causes strong

undersampling artefacts in image I_j . In a typical MRF sequence, the number of images N_j is much larger than the undersampling factor in k-space. The sampling spiral is rotated in order to achieve full k-space coverage over the whole set of acquisitions. For this reason the sum of all PSF functions for an MRF experiment, which will be denoted as P , approaches the Kronecker delta $\delta(\vec{x})$:

$$P \equiv \frac{1}{N_j} \sum_{j=1}^{N_j} P_j(\vec{x}) \approx \delta(\vec{x}). \quad (2.48)$$

An advantage of using equation (2.47) over equation (2.45) is that the former contains an inherent separation of the spatial and temporal functions. The spatial response function (the PSF) depends on the k-space sampling and the temporal function (the transverse magnetisation) depends on the acquisition parameters such as the sequence of flip angles and repetition times. Therefore, when using this model for an optimisation of the temporal acquisition parameters, the spatial response function does not need to be recalculated every iteration as it is independent of the acquisition parameters. Only the transverse magnetisation has to be updated for the optimisation resulting in a speed-up of at least one order of magnitude.

2.6.2. MODELLING PARAMETER ESTIMATION IN MRF

For a certain signal $\mathbf{I}(\vec{x})$, the MRF reconstruction of the tissue parameters can be described as:

$$\boldsymbol{\theta}^*(\vec{x}) = \underset{\boldsymbol{\theta}}{\operatorname{argmin}} \|\mathbf{I}(\vec{x}) - \mathbf{M}(\boldsymbol{\theta}(\vec{x}))\|^2, \quad (2.49)$$

in this model. The dependence on acquisition parameters $\boldsymbol{\xi}$ will be left out for readability from now on. In MR Fingerprinting experiments, the tissue parameters are reconstructed by applying a pattern matching algorithm to match the signal to an atom in a pre-computed dictionary. For realistic MRF experiments, the dictionary is such that the least-squares estimator in equation (2.49) and the resulting tissue parameters from pattern matching are in good agreement. We assume for now that the tissue parameters are $\boldsymbol{\theta} = (T_1, T_2, \rho)^T$ with ρ being the real valued proton density.

The MRF estimate for the tissue parameters $\boldsymbol{\theta}^*$ is the stationary point of the objective function in equation (2.49) for a certain signal $\mathbf{I}(\vec{x})$:

$$\left. \frac{\partial}{\partial \theta_p} \|\mathbf{I}(\vec{x}) - \mathbf{M}(\boldsymbol{\theta}(\vec{x}))\|^2 \right|_{\theta_p = \theta_p^*} = 0, \quad \forall x \in G_p, \forall p = 1, 2, \dots, N_{\boldsymbol{\theta}}. \quad (2.50)$$

Writing out this equation using the definition of the l_2 -norm and the product rule, the

following expression to model the dictionary matching is obtained:

$$\begin{aligned}
 & \left. \frac{\partial}{\partial \theta_p} \left\langle \mathbf{I}(\vec{x}) - \mathbf{M}(\boldsymbol{\theta}(\vec{x})), \mathbf{I}(\vec{x}) - \mathbf{M}(\boldsymbol{\theta}(\vec{x})) \right\rangle \right|_{\theta_p = \theta_p^*} = 0 \\
 & \left[\left\langle -\frac{\partial}{\partial \theta_p} \mathbf{M}(\boldsymbol{\theta}(\vec{x})), \mathbf{I}(\vec{x}) - \mathbf{M}(\boldsymbol{\theta}(\vec{x})) \right\rangle + \left\langle \mathbf{I}(\vec{x}) - \mathbf{M}(\boldsymbol{\theta}(\vec{x})), -\frac{\partial}{\partial \theta_p} \mathbf{M}(\boldsymbol{\theta}(\vec{x})) \right\rangle \right] \bigg|_{\theta_p = \theta_p^*} = 0 \\
 & \left[\overline{\left\langle \mathbf{M}(\boldsymbol{\theta}(\vec{x}) - \mathbf{I}(\vec{x})), \frac{\partial}{\partial \theta_p} \mathbf{M}(\boldsymbol{\theta}(\vec{x})) \right\rangle} + \left\langle \mathbf{M}(\boldsymbol{\theta}(\vec{x}) - \mathbf{I}(\vec{x})), \frac{\partial}{\partial \theta_p} \mathbf{M}(\boldsymbol{\theta}(\vec{x})) \right\rangle \right] \bigg|_{\theta_p = \theta_p^*} = 0 \\
 & \operatorname{Re} \left\langle \mathbf{M}(\boldsymbol{\theta}(\vec{x}) - \mathbf{I}(\vec{x})), \frac{\partial}{\partial \theta_p} \mathbf{M}(\boldsymbol{\theta}(\vec{x})) \right\rangle \bigg|_{\theta_p = \theta_p^*} = 0,
 \end{aligned} \tag{2.51}$$

for all $x \in G_p$ and for all $p \in 1, \dots, N_\Theta$.

2.6.3. PERTURBATION THEORY

To obtain a model for the undersampling error, the signal model for the undersampled images $\mathbf{I}(\vec{x})$ from equation (2.47) is substituted in the expression for dictionary matching from equation (2.51):

$$\operatorname{Re} \sum_{j=1}^{N_j} \left(M_j(\boldsymbol{\theta}^*(\vec{x})) - \sum_{\vec{y} \in G_p} P_j(\vec{x} - \vec{y}) M_j(\boldsymbol{\theta}(\vec{y})) \overline{\mathcal{D}M_{j,p}(\boldsymbol{\theta}^*(\vec{x}))} \right) = 0. \tag{2.52}$$

In this equation $\boldsymbol{\theta}$ are the true tissue parameters for which $\boldsymbol{\theta}^*$ is the estimator and $\mathcal{D}M_j$ is the Jacobian matrix of M_j . The subscript p denote the components of the Jacobian matrix: $p = 1$: derivative to T_1 , $p = 2$: derivative to T_2 , $p = 3$: derivative to ρ . To obtain the reconstructed parameters $\boldsymbol{\theta}^*$ analytically from this non-linear equation is difficult, if not impossible. To solve this we assume that the tissue parameters are relatively constant such that a perturbation theoretic expansion can be applied on $\boldsymbol{\theta}$ and $\boldsymbol{\theta}^*$:

$$\begin{aligned}
 \boldsymbol{\theta}(\vec{x}) &= \boldsymbol{\theta}_0 + \boldsymbol{\theta}_1(\vec{x}) \\
 \boldsymbol{\theta}^*(\vec{x}) &= \boldsymbol{\theta}_0 + \boldsymbol{\theta}_1^*(\vec{x}),
 \end{aligned} \tag{2.53}$$

where $\boldsymbol{\theta}$ and $\boldsymbol{\theta}^*$ denote the perturbation around the spatially constant $\boldsymbol{\theta}_0$. Using these expansions and a linearization in the magnetisation $M_j(\boldsymbol{\theta})$ and its derivative $M_j(\boldsymbol{\theta})$ an expression for $\boldsymbol{\theta}^*$ can be obtained. This expression is the model prediction of the reconstructed tissue parameters and should give information about the undersampling errors. The final result has the form:

$$\boldsymbol{\theta}_1^*(\vec{x}) = P * \boldsymbol{\theta}_1(\vec{x}) + \mathcal{E}_1(\vec{x}; \boldsymbol{\xi}) + \mathcal{E}_2(\vec{x}; \boldsymbol{\theta}_1, \boldsymbol{\xi}), \tag{2.54}$$

where \mathcal{E}_1 and \mathcal{E}_2 are error terms. This form will be derived in the next section.

2.6.4. LINEARIZATION AND ISOLATION OF THE TISSUE PARAMETERS

When working out equation (2.52) the following expression is obtained:

$$\begin{aligned} & \operatorname{Re} \sum_{j=1}^{N_j} M_j(\boldsymbol{\theta}^*(\vec{x})) \overline{\mathcal{D}M_{j;p}(\boldsymbol{\theta}^*(\vec{x}))} - \\ & \operatorname{Re} \sum_{j=1}^{N_j} \sum_{\vec{y} \in G_p} P_j(\vec{x} - \vec{y}) M_j(\boldsymbol{\theta}(\vec{y})) \overline{\mathcal{D}M_{j;p}(\boldsymbol{\theta}^*(\vec{x}))} = 0 \quad \forall x \in G_p, \forall p = 1, 2, \dots, N_\Theta. \end{aligned} \quad (2.55)$$

2.6.4.1. EXPANSION OF THE SECOND TERM OF EQUATION (2.55)

To obtain an expression from the second term of equation (2.55) in which the reconstructed tissue parameters $\boldsymbol{\theta}^*$ are explicit, the perturbation theoretic expansion from equation (2.53) is substituted into $M_j(\boldsymbol{\theta}(\vec{y})) \mathcal{D}M(\boldsymbol{\theta}^*(\vec{x}))$ and subsequently a linearization is performed:

$$\begin{aligned} M_j(\boldsymbol{\theta}(\vec{y})) \overline{\mathcal{D}M_{j;p}(\boldsymbol{\theta}^*(\vec{x}))} &= M_j(\boldsymbol{\theta}_0) \overline{\mathcal{D}M_{j;p}(\boldsymbol{\theta}_0)} + \sum_{q=1}^{N_\Theta} \mathcal{D}M_{j;q}(\boldsymbol{\theta}_0) \overline{\mathcal{D}M_{j;p}(\boldsymbol{\theta}_0)} \theta_{1,q}(\vec{y}) \\ &+ \sum_{q=1}^{N_\Theta} M_j(\boldsymbol{\theta}_0) \overline{\mathcal{D}^2 M_{j;p,q}(\boldsymbol{\theta}_0)} \theta_{1,q}^*(\vec{x}) + \text{h.o.t.}, \end{aligned} \quad (2.56)$$

where h.o.t. is the abbreviation for higher order terms. Some ad hoc definitions will now be presented, in order to make the derivation easier to follow:

$$\begin{aligned} S_p^{(1,0)}(\vec{x}) &= \sum_{j=1}^{N_j} P_j(\vec{x}) \overline{\mathcal{D}M_{j;p}(\boldsymbol{\theta}_0)} M_j(\boldsymbol{\theta}_0) \\ S_{p,q}^{(1,1)}(\vec{x}) &= \sum_{j=1}^{N_j} P_j(\vec{x}) \overline{\mathcal{D}M_{j;p}(\boldsymbol{\theta}_0)} \mathcal{D}M_{j;q}(\boldsymbol{\theta}_0) \\ S_{p,q}^{(2,0)}(\vec{x}) &= \sum_{j=1}^{N_j} P_j(\vec{x}) \overline{\mathcal{D}^2 M_{j;p,q}(\boldsymbol{\theta}_0)} M_j(\boldsymbol{\theta}_0). \end{aligned} \quad (2.57)$$

Substituting the expansion in equation (2.56) in the second term of equation (2.55), the following expression is obtained:

$$\begin{aligned} \operatorname{Re} \sum_{j=1}^{N_j} \sum_{\vec{y} \in G_p} P_j(\vec{x} - \vec{y}) M_j(\boldsymbol{\theta}(\vec{y})) \overline{\mathcal{D}M_{j;p}(\boldsymbol{\theta}^*(\vec{x}))} &= \operatorname{Re} \left(S_p^{(1,0)}(\vec{x}) * \mathbb{1}(\vec{x}) \right. \\ &+ \sum_{q=1}^{N_\Theta} S_{p,q}^{(1,1)}(\vec{x}) * \theta_{1,q}(\vec{x}) \\ &\left. + \sum_{q=1}^{N_\Theta} (S_{p,q}^{(2,0)}(\vec{x}) * \mathbb{1}(\vec{x})) \theta_{1,q}^*(\vec{x}) \right), \end{aligned} \quad (2.58)$$

where ‘*’ is the convolution operator and $\mathbb{1}(\vec{x})$ is a constant function which is 1 for all locations \vec{x} .

2.6.4.2. EXPANSION OF THE FIRST TERM OF EQUATION (2.55)

To make the reconstructed tissue parameters $\boldsymbol{\theta}^*$ in the first term of equation (2.55) explicit, the perturbation theoretic expansion from equation (2.53) is substituted into $M_j(\boldsymbol{\theta}^*(\vec{x}))\overline{\mathcal{D}M(\boldsymbol{\theta}^*(\vec{x}))}$ and subsequently a linearization is performed. The results are equivalent to equation (2.56) upon replacement of $\theta_{1,q}(\vec{y})$ with $\theta_{1,q}^*(\vec{x})$. Some ad hoc separation will be presented, which proved to make the derivation easier to follow:

$$\begin{aligned} S_{\text{mean};p,q}^{(1,1)}(\vec{x}) &= P(\vec{x}) \sum_{j=1}^{N_j} \overline{\mathcal{D}M_{j;p}(\boldsymbol{\theta}_0)} \mathcal{D}M_{j;q}(\boldsymbol{\theta}_0) \\ S_{\text{resid};p,q}^{(1,1)}(\vec{x}) &= \sum_{j=1}^{N_j} (P_j(\vec{x}) - P(\vec{x})) \overline{\mathcal{D}M_{j;p}(\boldsymbol{\theta}_0)} \mathcal{D}M_{j;q}(\boldsymbol{\theta}_0). \end{aligned} \quad (2.59)$$

such that:

$$S_{p,q}^{(1,1)}(\vec{x}) = S_{\text{mean};p,q}^{(1,1)}(\vec{x}) + S_{\text{resid};p,q}^{(1,1)}(\vec{x}) \cdot A \quad (2.60)$$

The separation for $S_p^{(1,0)}(\vec{x})$ and $S_{p,q}^{(2,0)}(\vec{x})$ are achieved in a similar way. The final errors $\epsilon_1(\vec{x})$ and $\epsilon_2(\vec{x})$ will be depend on the residual parts. As already noted in [8], the residual parts vanish when there is no undersampling as $P_j(\vec{x}) = P(\vec{x}) = \delta(\vec{x})$ or when the magnetisation is in steady state such that the weighting terms $\overline{\mathcal{D}M_{j;p}(\boldsymbol{\theta}_0)} \mathcal{D}M_{j;q}(\boldsymbol{\theta}_0)$ become time-independent. The latter situation applies to (most) conventional MRI acquisitions.

Using this separation and noting that $P * \mathbb{1} \approx \mathbb{1}$, the linearization of the first term of equation (2.55) can be written as:

$$\begin{aligned} \text{Re} \sum_{j=1}^{N_j} M_j(\boldsymbol{\theta}^*(\vec{x})) \overline{\mathcal{D}M_{j;p}(\boldsymbol{\theta}^*(\vec{x}))} &= \text{Re} \left(S_{\text{mean};p}^{(1,0)}(\vec{x}) * \mathbb{1}(\vec{x}) \right. \\ &\quad + \sum_{q=1}^{N_\Theta} \left(S_{\text{mean};p,q}^{(1,1)}(\vec{x}) * \mathbb{1}(\vec{x}) \right) \theta_{1,q}^*(\vec{x}) \\ &\quad \left. + \sum_{q=1}^{N_\Theta} \left(S_{\text{mean};p,q}^{(2,0)}(\vec{x}) * \mathbb{1}(\vec{x}) \right) \theta_{1,q}^*(\vec{x}) \right). \end{aligned} \quad (2.61)$$

2.6.4.3. ISOLATION OF THE TISSUE PARAMETERS

Combining the expansions from equations (2.59) and (2.61) in equation (2.55) results in the following equation:

$$\begin{aligned} \text{Re} \left(\sum_{q=1}^{N_\Theta} S_{\text{mean};p,q}^{(1,1)} * \theta_{1,q} - \sum_{q=1}^{N_\Theta} \left(S_{\text{mean};p,q}^{(1,1)} * \mathbb{1} \right) \theta_{1,q}^* \right. \\ \left. S_{\text{resid};p}^{(1,0)} * \mathbb{1} + \sum_{q=1}^{N_\Theta} S_{\text{resid};p,q}^{(1,1)} * \theta_{1,q} \right) \\ \sum_{q=1}^{N_\Theta} \left(S_{\text{resid};p,q}^{(2,0)} * \mathbb{1} \right) \theta_{1,q}^* = 0 \quad \forall x \in G_p, \forall p = 1, 2, \dots, N_\Theta, \end{aligned} \quad (2.62)$$

where the dependence on \vec{x} is left out for readability. Note that this equation is obtained by cancellation of $\pm S_{\text{mean};p}^{(1,0)} * \mathbb{1}$ and $\pm (S_{\text{mean};p,q}^{(2,0)} * \mathbb{1}) \theta_{1,q}^*$. The next step is to use the Fisher Information Matrix:

$$N_{p,q} = \sum_{j=1}^{N_j} \overline{\mathcal{D} M_{j;p}(\boldsymbol{\theta}_0)} \mathcal{D} M_{j;q}(\boldsymbol{\theta}_0), \quad (2.63)$$

and rewrite the first two terms of equation (2.62) into matrix form:

$$\begin{aligned} \sum_{q=1}^{N_\Theta} S_{\text{mean};p,q}^{(1,1)} * \theta_{1,q} &= N(P * \boldsymbol{\theta}_1) \\ \sum_{q=1}^{N_\Theta} (S_{\text{mean};p,q}^{(1,1)} * \mathbb{1}) \theta_{1,q}^* &= (N\boldsymbol{\theta}_1^*)(P * \mathbb{1}) = N\boldsymbol{\theta}_1^*, \end{aligned} \quad (2.64)$$

where for the second equation $P * \mathbb{1} \approx \mathbb{1}$ was used. The last term in equation (2.62) will be neglected as it consists of two terms which are believed to be small: $S_{\text{resid}}^{(2,0)}$ and $\boldsymbol{\theta}_1^*$. Note that $\boldsymbol{\theta}_1^*$ and $\boldsymbol{\theta}_1$ should be real as they contain tissue parameters, and that P is approximately real as it approaches the Kronecker delta. Rewriting equation (2.62) with the matrix forms from (2.64) and using the observations mentioned above, the following result is obtained:

$$\boldsymbol{\theta}_1^* = P * \boldsymbol{\theta}_1 + \text{Re}(N)^{-1} \mathbf{E}_1(\boldsymbol{\xi}) + \text{Re}(N)^{-1} \mathbf{E}_2(\boldsymbol{\theta}; \boldsymbol{\xi}), \quad (2.65)$$

with the error vectors:

$$\begin{aligned} \mathbf{E}_{1,p}(\vec{x}) &= \text{Re}(S_{\text{resid};p}^{(1,0)}(\vec{x}) * \mathbb{1}(\vec{x})) \\ \mathbf{E}_{2,p}(\vec{x}) &= \text{Re}\left(\sum_{q=1}^{N_\Theta} S_{\text{resid};p,q}^{(1,1)}(\vec{x}) * \theta_{1,q}(\vec{x})\right). \end{aligned} \quad (2.66)$$

Note that the first term in equation (2.65) is an approximation of the true tissue parameters $\boldsymbol{\theta}_1$. This part can only be improved by using a better k-space sampling scheme. The error terms \mathbf{E}_1 and \mathbf{E}_2 depend on the acquisition parameters and might be improved by an optimisation of these variables.

2.7. OPTIMISATION METHOD

The optimisation problems in this project are non-linear and non-convex. For a non-convex problem the global convergence is not guaranteed. In this research project Sequential Least-Square Quadratic Programming (SLSQP) is used for the optimisations. This Sequential Quadratic Programming (SQP) algorithm is an iterative optimisation method suited for non-linearly constrained gradient-based optimisation. The idea behind the method is to reformulate the problem by applying a quadratic approximation of the cost function function at the current solution. Then it solves a constrained quadratic optimisation problem using linearisation of the constraints.

To speed-up the algorithm, the gradients in the multi-dimensional optimisation space are calculated explicitly using a forward-difference method and fed back to the optimisation algorithm. This approach is faster than letting the algorithm calculate the gradients itself as it was parallelised using a multi-processor tool. The step size for the forward-difference method is $h = \sqrt{\epsilon_m} \max(x, 1)$, with ϵ_m the machine precision and x the optimisation parameters. This step size is an approximation to the optimal step size taking into account the roundoff and truncation error [26].

3

METHODS

This chapter is concerned with presenting the frameworks used for numerical optimisations. Section 3.1 presents *Optimisation Framework I*, which is an MRF-based model that relates the lower bound of the variance in the reconstructed tissue parameters to the sequence choice. This framework assumes stochastic noise in the measurements, implemented in a multi-component setting. After this, section 3.2 presents *Optimisation Framework II* that is an MRF-based model that relates the undersampling error in the reconstructed tissue parameters to the sequence choice for a certain k-space sampling scheme. In section 3.3 the optimisation problems based on both frameworks are made explicit and finally section 3.4 discusses the settings used for the numerical and in vivo experiments.

3.1. OPTIMISATION *Framework I*: MULTI-COMPONENT MODEL AND STOCHASTIC ERRORS

The multi-component signal model with stochastic noise is created by combining the signal models introduced in section 2.4 and 2.5:

$$s_j = \sum_{n=1}^{N_T} M_j(\boldsymbol{\theta}^n) + \varepsilon_j \quad j = 1, 2, \dots, N_J \quad (3.1)$$

with N_T the amount of different tissue types in a voxel, $\boldsymbol{\theta}^n$ the tissue parameters for tissue n and j is the time index. Remember the notation $M_{j;\text{multi}}(\boldsymbol{\theta}) \equiv \sum_{n=1}^{N_T} M_j(\boldsymbol{\theta}^n)$ from section 2.4. Note that the in-phase refocusing axis is chosen to be real, without loss of generality. For this research project two different tissue types ($N_T = 2$) are used: tissue a and tissue b . The unknown tissue parameters for the MRF experiment are: $\boldsymbol{\theta} = (T_1^a, T_2^a, \rho^a, T_1^b, T_2^b, \rho^b)^T$ in this multi-component case. The optimisation of the acquisition parameters, which will be introduced in section 3.3, will decrease the lower bound on the variance for any unbiased estimator of the tissue parameters $\hat{\boldsymbol{\theta}}$ using the CRLB. We hope that using optimised acquisition parameters with a decreased lower bound on the variance of the unbiased estimators in the vector $\hat{\boldsymbol{\theta}}$, will result in MRF tissue maps that are more robust for stochastic noise. It was assumed that the noise can be modelled as an independent identically distributed Gaussian process with mean 0 and variance σ^2 . To find the CRLB the FIM has to be constructed using the Gaussian noise distribution. The probability density distribution of the signal is:

$$p(\mathbf{s}; \boldsymbol{\theta}) = \prod_{j=1}^{N_J} \frac{1}{\sqrt{2\pi\sigma^2}} e^{-\frac{(s_j - M_{j;\text{multi}}(\boldsymbol{\theta}))^2}{2\sigma^2}}. \quad (3.2)$$

Taking the natural logarithm of this probability density function and partially differentiating to tissue parameter θ_p the following expression is obtained:

$$\frac{\partial \ln p(\mathbf{s}; \boldsymbol{\theta})}{\partial \theta_p} = \frac{1}{\sigma^2} \sum_{j=1}^{N_J} (s_j - M_{j;\text{multi}}(\boldsymbol{\theta})) \frac{\partial M_{j;\text{multi}}}{\partial \theta_p}. \quad (3.3)$$

Using this, the resulting components of the FIM are:

$$\begin{aligned} N_{p,q} &= \mathbb{E} \left[\left(\frac{\partial \ln(p(\mathbf{s}; \boldsymbol{\theta}))}{\partial \theta_p} \right) \left(\frac{\partial \ln(p(\mathbf{s}; \boldsymbol{\theta}))}{\partial \theta_q} \right) \right] \\ &= \frac{1}{\sigma^4} \mathbb{E} \left[\sum_{j_1=1}^{N_J} \sum_{j_2=1}^{N_J} (s_{j_1} - M_{j_1;\text{multi}}) (s_{j_2} - M_{j_2;\text{multi}}) \frac{\partial M_{j_1;\text{multi}}}{\partial \theta_p} \frac{\partial M_{j_2;\text{multi}}}{\partial \theta_q} \right] \\ &= \frac{1}{\sigma^4} \sum_{j=1}^{N_J} \frac{\partial M_{j;\text{multi}}}{\partial \theta_p} \frac{\partial M_{j;\text{multi}}}{\partial \theta_q} \mathbb{E} [(s_j - M_{j;\text{multi}})^2] \\ &= \frac{1}{\sigma^2} \sum_{j=1}^{N_J} \frac{\partial M_{j;\text{multi}}}{\partial \theta_p} \frac{\partial M_{j;\text{multi}}}{\partial \theta_q}. \end{aligned} \quad (3.4)$$

where the third line in the derivation is due to the fact that the noise from measurements at different time indices is uncorrelated. The analytic expression for the derivatives in equation (3.4) can be calculated by using the EPG model from section 2.2.2.4.

3.2. OPTIMISATION *Framework II*: UNDERSAMPLING ERRORS

The undersampling model used in this research project is an extension of the model introduced in section 2.6. The extensions will be discussed in this section and are crucial to make the model predict the undersampling error in real scan data. The 3 extensions are: (1) adding noise to the model; (2) introducing the transmit phase in the model; (3) introducing a variable reference proton density [8]. Addition (2) will appear to be especially important to obtain a model with reasonable predictive power.

3.2.1. SIGNAL MODEL EXTENDED WITH STOCHASTIC TERM

The k-space noise free signal can be calculated using the discrete Fourier transform of the magnetisation M_j :

$$s_j(\vec{k}_{j,l}) = \sum_{\vec{x} \in G_p} M_j(\boldsymbol{\theta}(\vec{x}); \boldsymbol{\xi}) e^{-i\vec{k}_{j,l} \cdot \vec{x}}. \quad (3.5)$$

Again, j denotes the time index and l denotes the index of the k-space read-out. Note that the acquisition parameters ($\boldsymbol{\xi}$) can also be spatially dependent, but for this research project they are assumed to be constant for the x, y -plane under consideration. When performing MR measurements, multiple noise sources such as the stochastic motion of free electrons in the receiver coil and eddy current losses will deteriorate the quality of the image. These noise sources can be modelled by adding a stochastic term to the k-space signal $s_j(\vec{k}_{j,l})$.

However, adding uncorrelated complex Additive White Gaussian Noise (AWGN) in k-space causes the noise in image space to become correlated because of the undersampling. A derivation of this fact can be found in Appendix D. To avoid having to use correlated noise terms in image space, complex AWGN noise is added directly to image space. Therefore, the expression for the undersampled image changes to:

$$I_j(\vec{x}) = P_j * M_j + \varepsilon_j(\vec{x}), \quad (3.6)$$

where $\varepsilon_j(\vec{x}) = n_r(0, \sigma^2) + n_i(0, \sigma^2) \cdot i$. In this equation $n(0, \sigma^2)$ is a Gaussian white noise term with 0 mean and variance σ^2 . Adding noise directly to image space has been proven to be a valid approach in the context of MR Fingerprinting [9]. The choice to add the noise to image space also facilitates the estimation of the noise variance, as this process is easier in image space than it is in k-space.

3.2.2. ADDING TRANSMIT PHASE

Thus far we have assumed that the axis with respect to which the flip angle is applied, is spatially constant such that the refocusing takes place in the same direction for all voxels in an image. In practice, this is not the case due to e.g. spatial variations in the electrical conductivity and permittivity of the sample [27] and timing issues within the system. The angle that the rotation axis makes with the x' -axis will be referred to as the transmit phase, denoted by $\omega(\vec{x})$ (do not confuse this ω with the Larmor frequency used in section 2.1). To include the spatially dependent transmit phase in the undersampling model, a multiplicative term is added:

$$s_j(\vec{k}_{j,l}) = \sum_{\vec{x} \in G_p} \omega(\vec{x}) M_j(\boldsymbol{\theta}(\vec{x}); \boldsymbol{\xi}) e^{-i\vec{k}_{j,l} \cdot \vec{x}}. \quad (3.7)$$

To include the transmit phase in the undersampling model, it is absorbed in the proton density ρ^* , as will become apparent from the derivation. This results in an extension of the tissue parameter vector $\boldsymbol{\theta}^* = (T_1^*, T_2^*, \text{Re}(\rho^*), \text{Im}(\rho^*))^T$.

3.2.3. VARIABLE REFERENCE PROTON DENSITY

To obtain the undersampling model, a linearization is performed around $\boldsymbol{\theta}_0$. This is only valid when all tissue parameters are close to some constant reference value throughout the entire image. For the proton density, this assumption is conflicting with reality as it is zero outside the sample where there is air. By exploiting the linearity of the proton density in the transverse magnetisation a variable reference proton density can be introduced: $\rho_0(\vec{x})$. This function is constant inside the sample and zero outside. Defining the vector $\boldsymbol{\eta} = (T_1, T_2)^T$ for convenience, the perturbation theoretic expansion can be rewritten as:

$$\begin{aligned} \boldsymbol{\eta}(\vec{x}) &= \boldsymbol{\eta}_0 + \boldsymbol{\eta}_1(\vec{x}) & \boldsymbol{\eta}^*(\vec{x}) &= \boldsymbol{\eta}_0 + \boldsymbol{\eta}_1^*(\vec{x}) \\ \rho(\vec{x}) &= \rho_0(\vec{x})(1 + \rho_1(\vec{x})) & \rho^*(\vec{x}) &= \rho_0^*(\vec{x})(1 + \rho_1^*(\vec{x})), \end{aligned} \quad (3.8)$$

Notice that the function $\rho_0^*(\vec{x})$ can be freely chosen. This freedom will be exploited later in the derivation of the extended undersampling model. Using the linearity of the proton density in the transverse magnetisation, $\rho_0^{(*)}(\vec{x})$ can be introduced in the signal model as an explicit term:

$$\begin{aligned} M_j(\boldsymbol{\theta}(\vec{x})) &= \rho_0(\vec{x})M_j(\boldsymbol{\theta}_0 + \boldsymbol{\theta}_1(\vec{x})) \\ M_j(\boldsymbol{\theta}^*(\vec{x})) &= \rho_0^*(\vec{x})M_j(\boldsymbol{\theta}_0 + \boldsymbol{\theta}_1^*(\vec{x})), \end{aligned} \quad (3.9)$$

such that the remaining tissue parameters can be expanded as:

$$\begin{aligned} \boldsymbol{\theta}_0 + \boldsymbol{\theta}_1(\vec{x}) &= \left(\boldsymbol{\eta}_0, 1, 0 \right)^T + \left(\boldsymbol{\eta}_1(\vec{x}), \text{Re}(\rho_1(\vec{x})), \text{Im}(\rho_1(\vec{x})) \right)^T \\ \boldsymbol{\theta}_0 + \boldsymbol{\theta}_1^*(\vec{x}) &= \left(\boldsymbol{\eta}_0, 1, 0 \right)^T + \left(\boldsymbol{\eta}_1^*(\vec{x}), \text{Re}(\rho_1^*(\vec{x})), \text{Im}(\rho_1^*(\vec{x})) \right)^T. \end{aligned} \quad (3.10)$$

For this perturbation theoretic expansion, the same definitions for $S_{p,q}^{(1,1)}$, etc. as in equation (2.57) can be used for the derivation of the extended undersampling model.

3.2.4. EXTENDED UNDERSAMPLING MODEL

Using complex AWGN in image space, the spatially dependent transmit phase and the variable reference proton density, an extended undersampling model can be obtained. The final result has the form:

$$\boldsymbol{\theta}_1^*(\vec{x}) = \text{Re}(f(P) * (\rho_0 \boldsymbol{\theta}_1))(\vec{x}) + \mathcal{E}_1(\vec{x}; \boldsymbol{\xi}) + \mathcal{E}_2(\vec{x}; \boldsymbol{\theta}_1, \boldsymbol{\xi}) + \mathcal{E}_3(\vec{x}; \boldsymbol{\xi}), \quad (3.11)$$

where f is a linear operator on the PSF. In this equation \mathcal{E}_1 , \mathcal{E}_2 and \mathcal{E}_3 are error terms, with the latter being of stochastic nature. This form will be derived in the next paragraph.

Starting with the extended version of equation (2.52) for dictionary matching:

$$\text{Re} \sum_{j=1}^{N_j} \left[\left(\rho_0^*(\vec{x}) M_j(\boldsymbol{\theta}_0 + \boldsymbol{\theta}_1^*(\vec{x})) - \left(P_j * (\rho_0 \omega M_j(\boldsymbol{\theta}_0 + \boldsymbol{\theta}_1)) \right)(\vec{x}) - \varepsilon_j(\vec{x}) \right) \cdot \overline{\rho_0^*(\vec{x}) \mathcal{D} M_{j;p}(\boldsymbol{\theta}_0 + \boldsymbol{\theta}_1^*(\vec{x}))} \right] = 0, \quad (3.12)$$

for all $\vec{x} \in G_p$ and for all $p \in 1, \dots, N_\Theta$. Working out the brackets, this results in three terms:

$$\begin{aligned} \operatorname{Re} \left(\overline{\rho_0^*}(\vec{x}) \left[\sum_{j=1}^{N_j} \rho_0^*(\vec{x}) M_j(\boldsymbol{\theta}_0 + \boldsymbol{\theta}_1^*(\vec{x})) \overline{\mathcal{D}M_{j;p}(\boldsymbol{\theta}_0 + \boldsymbol{\theta}_1^*(\vec{x}))} + \right. \right. \\ \left. \left. - \sum_{j=1}^{N_j} \sum_{\vec{y} \in G_p} P_j(\vec{x} - \vec{y}) \rho_0(\vec{y}) \omega(\vec{y}) M_j(\boldsymbol{\theta}_0 + \boldsymbol{\theta}_1(\vec{y})) \overline{\mathcal{D}M_{j;p}(\boldsymbol{\theta}_0 + \boldsymbol{\theta}_1^*(\vec{x}))} + \right. \right. \\ \left. \left. - \sum_{j=1}^{N_j} \varepsilon_j(\vec{x}) \overline{\mathcal{D}M_{j;p}(\boldsymbol{\theta}_0 + \boldsymbol{\theta}_1^*(\vec{x}))} \right] \right) = 0 \end{aligned} \quad (3.13)$$

Linearizing these three terms like in section 2.6.4, the following result is obtained:

$$\begin{aligned} \operatorname{Re} \left(\overline{\rho_0^*} \left[\rho_0^* S_{\text{mean};p}^{(1,0)} * \mathbb{1} + \sum_{q=1}^{N_\Theta} \rho_0^* (S_{\text{mean};p,q}^{(1,1)} * \mathbb{1}) \theta_{1,q}^* + \sum_{q=1}^{N_\Theta} \rho_0^* (S_{\text{mean};p,q}^{(2,0)} * \mathbb{1}) \theta_{1,q}^* \right. \right. \\ \left. \left. - S_{\text{mean};p}^{(1,0)} * (\rho_0 \omega) - \sum_{q=1}^{N_\Theta} S_{\text{mean};p,q}^{(1,1)} * (\rho_0 \omega \theta_{1,q}) - \sum_{q=1}^{N_\Theta} (S_{\text{mean};p,q}^{(2,0)} * (\rho_0 \omega)) \theta_{1,q}^* \right. \right. \\ \left. \left. - S_{\text{resid};p}^{(1,0)} * (\rho_0 \omega) - \sum_{q=1}^{N_\Theta} S_{\text{resid};p,q}^{(1,1)} * (\rho_0 \omega \theta_{1,q}) - \sum_{q=1}^{N_\Theta} (S_{\text{resid};p,q}^{(2,0)} * (\rho_0 \omega)) \theta_{1,q}^* \right. \right. \\ \left. \left. - \sum_{j=1}^{N_j} \varepsilon_j \overline{\mathcal{D}M_{j;p}(\boldsymbol{\theta}_0)} - \sum_{q=1}^{N_\Theta} \sum_{j=1}^{N_j} \varepsilon_j \overline{\mathcal{D}^2 M_{j;p,q}(\boldsymbol{\theta}_0)} \theta_{1,q}^* \right] \right) = 0 \end{aligned} \quad (3.14)$$

where the dependencies are left out for readability. Note that the definition of ρ_0^* can still be chosen. In order to obtain some cancellations, it is set to:

$$\rho_0^*(\vec{x}) \equiv P * (\rho_0(\cdot) \omega(\cdot)). \quad (3.15)$$

As pointed out in section 2.6.4: $P * \mathbb{1} \approx \mathbb{1}$, such that $\rho_0^* S_{\text{mean};p}^{(1,0)} * \mathbb{1} \approx S_{\text{mean};p}^{(1,0)} * (\rho_0 \omega)$ and $\sum_{q=1}^{N_\Theta} \rho_0^* (S_{\text{mean};p,q}^{(2,0)} * \mathbb{1}) \theta_{1,q}^* \approx \sum_{q=1}^{N_\Theta} (S_{\text{mean};p,q}^{(2,0)} * (\rho_0 \omega)) \theta_{1,q}^*$, resulting in the cancellation of these terms in equation (3.14). Just as in section 2.6.4, $\sum_{q=1}^{N_\Theta} (S_{\text{resid};p,q}^{(2,0)} * (\rho_0 \omega)) \theta_{1,q}^*$ is neglected in the spirit of keeping only the first order terms.

The term $\sum_{q=1}^{N_\Theta} \sum_{j=1}^{N_j} \varepsilon_j \overline{\mathcal{D}^2 M_{j;p,q}(\boldsymbol{\theta}_0)} \theta_{1,q}^*$ in equation 3.14 is removed as well, as it appeared to be negligible compared to the other stochastic term. This can be made plausible by noting that:

$$\begin{aligned} M_j &\propto e^{\frac{-1}{\eta(1,2)}} \\ M_j &\propto \rho \end{aligned} \quad (3.16)$$

Using these proportionalities the following asymptotic behaviour is found:

$$\begin{aligned} \mathcal{D}M_{j;\{1,2\}} &= \mathcal{O}(\eta^{-2}) & \mathcal{D}^2 M_{j;\{(1,1),(2,2)\}} &= \mathcal{O}(\eta^{-3}) \\ \mathcal{D}M_{j;3} &= \mathcal{O}(1) & \mathcal{D}^2 M_{j;\{3,3\}} &= 0 \end{aligned} \quad (3.17)$$

where \mathcal{O} is the Bachmann-Landau symbol. It has been checked by this author that the mixed second derivatives multiplied by their respective factors $\theta_{1,q}^*$ are also small compared to the first order derivative. Finally a small numerical study on a toy example confirmed that the stochastic term based on the first order derivative dominated the one based on the second order derivative (data not shown). This motivates neglecting the term $\sum_{q=1}^{N_\Theta} \sum_{j=1}^{N_J} \varepsilon_j \overline{\mathcal{D}^2 M_{j;p,q}(\boldsymbol{\theta}_0)} \theta_{1,q}^*$.

The resulting equation after the 6 cancellations described above is:

$$\begin{aligned} \operatorname{Re} \left(\overline{\rho_0^*} \left[\sum_{q=1}^{N_\Theta} \rho_0^* (S_{\text{mean};p,q}^{(1,1)} * \mathbb{1}) \theta_{1,q}^* - \sum_{q=1}^{N_\Theta} S_{\text{mean};p,q}^{(1,1)} * (\rho_0 \omega \theta_{1,q}) - S_{\text{resid};p}^{(1,0)} * (\rho_0 \omega) \right. \right. \\ \left. \left. - \sum_{q=1}^{N_\Theta} S_{\text{resid};p,q}^{(1,1)} * (\rho_0 \omega \theta_{1,q}) - \sum_{j=1}^{N_J} \varepsilon_j \overline{\mathcal{D} M_{j;p}(\boldsymbol{\theta}_0)} \right] \right) = 0 \quad \forall \vec{x} \in G_p, \forall p = 1, 2, \dots, N_\Theta. \end{aligned} \quad (3.18)$$

Applying the same steps as in section 2.6.4.3, the extended undersampling model is found:

$$\boldsymbol{\theta}_1^* = \frac{1}{|\overline{\rho_0^*}|^2} \operatorname{Re}(N)^{-1} \left(\operatorname{Re} \left(\overline{\rho_0^*} N (P * (\rho_0 \omega \boldsymbol{\theta}_1)) \right) + \mathbf{E}_1(\boldsymbol{\xi}) + \mathbf{E}_2(\boldsymbol{\theta}; \boldsymbol{\xi}) + \mathbf{E}_3(\boldsymbol{\xi}) \right) \quad (3.19)$$

with the error vectors:

$$\begin{aligned} E_{1,p}(\vec{x}) &= \operatorname{Re} \left(\overline{\rho_0^*} S_{\text{resid};p}^{(1,0)} * (\rho_0 \omega) \right) \\ E_{2,p}(\vec{x}) &= \operatorname{Re} \left(\overline{\rho_0^*} \sum_{q=1}^{N_\Theta} S_{\text{resid};p,q}^{(1,1)} * (\rho_0 \omega \theta_{1,q}) \right) \\ E_{3,p}(\vec{x}) &= \operatorname{Re} \left(\overline{\rho_0^*} \sum_{j=1}^{N_J} \varepsilon_j \overline{\mathcal{D} M_{j;p}(\boldsymbol{\theta}_0)} \right). \end{aligned} \quad (3.20)$$

Note that the first term in equation (3.19) is an approximation of the true tissue parameters $\boldsymbol{\theta}_1$. This part can only be improved by using a better k-space sampling scheme. The error terms \mathbf{E}_1 , \mathbf{E}_2 and \mathbf{E}_3 depend on the acquisition parameters and might be improved by an optimisation of these variables.

3.2.5. REDEFINING THE LINEARIZATION VARIABLES

As the extended undersampling model is based on a first order Taylor expansion in the tissue parameters, it is interesting to investigate the accuracy of this approximation using the Taylor remainder term. In this context a brief numerical investigation suggested a change of variables to the tissue parameters: $\hat{\boldsymbol{\theta}} = (\ln(T_1), \ln(T_2), \operatorname{Re}(\rho), \operatorname{Im}(\rho))$. A short numerical evaluation using a simplified system showed that the remainder term is lower on a domain of realistic relaxation times when the suggested change of variables is applied. This result does not hold true for any domain, but it does for the domains interesting for this research project.

3.3. OPTIMISATION PROBLEMS

This section presents the minimisation problems for which the optimisations are performed for both frameworks. The optimisations are performed using a nonlinear optimisation method called SLSQP. This iterative algorithm was introduced in section 2.7. A multi-processor implementation was developed which reduced the computation time by an order of magnitude.

3.3.1. OPTIMISATION PROBLEMS *Framework I*

The first MC optimisation is performed using a voxel with two different tissues ($N_T = 2$). The estimators for the tissue parameters are: $\hat{\theta} = (\hat{T}_1^a, \hat{T}_2^a, \hat{\rho}^a, \hat{T}_1^b, \hat{T}_2^b, \hat{\rho}^b)$. This results in a FIM with dimensions 6×6 . This optimisation is called Opt α and is defined as follows:

$$\begin{array}{ll}
 \min_{\{\alpha_n\}_{n=1}^{N_J}, \{TR_n\}_{n=1}^{N_J-1}} & \sum_{i=1}^6 w_i \cdot N^{-1} (T_1^a, T_2^a, M_0^a, T_1^b, T_2^b, M_0^b)_{i,i} \\
 \text{Opt}\alpha \quad \text{s.t.} & 10^\circ \leq \alpha_n \leq 60^\circ \quad \forall n \in \{2, 3, \dots, N_J\} \\
 & 11 \text{ ms} \leq TR_n \leq 15 \text{ ms} \quad \forall n \in \{1, 2, \dots, N_J - 1\} \\
 & |\alpha_{n+1} - \alpha_n| \leq 1^\circ \quad \forall n \in \{1, 2, \dots, N_J - 1\}
 \end{array}$$

where w_i is a manually chosen weighting term such that the variances are normalised and weighted according to our believes of which tissue parameters are more important. The bounds on the first flip angle are $10^\circ \leq \alpha_1 \leq 180^\circ$. For this optimisation: $w_{\{1,4\}} = 2 \cdot 10^{-5}$; $w_{\{2,5\}} = 5 \cdot 10^{-4}$; $w_{\{3,6\}} = 30$. The acquisition parameters α_n and TR_n denote the flip angle and repetition time for time index n respectively. The first constraint is added to reduce the optimisation space and keep the result unique. The second constraint is added to keep the scan time of the resulting sequence clinically feasible. The third constraint causes the resulting magnetisation evolution to be more smooth, which is beneficial in most reconstruction algorithms [9].

The second MC optimisation is again performed using a voxel with two different tissues ($N_T = 2$). The relaxation parameters are assumed to be known such that the estimators for the tissue parameters are: $\hat{\theta} = (\hat{\rho}^a, \hat{\rho}^b)$. This results in a FIM with dimensions 2×2 . This optimisation is called Opt β and is defined as follows:

$$\begin{array}{ll}
 \min_{\{\alpha_n\}_{n=1}^{N_J}, \{TR_n\}_{n=1}^{N_J-1}} & \sum_{i=1}^2 N^{-1} (M_0^a, M_0^b)_{i,i} \\
 \text{Opt}\beta \quad \text{s.t.} & 10^\circ \leq \alpha_n \leq 60^\circ \quad \forall n \in \{2, 3, \dots, N_J\} \\
 & 11 \text{ ms} \leq TR_n \leq 15 \text{ ms} \quad \forall n \in \{1, 2, \dots, N_J - 1\} \\
 & |\alpha_{n+1} - \alpha_n| \leq 1^\circ \quad \forall n \in \{1, 2, \dots, N_J - 1\}
 \end{array}$$

where the bounds on the first flip angle are $10^\circ \leq \alpha_1 \leq 180^\circ$.

The optimisations are performed with two different initialisations to estimate if the result is close to the global minimum. Two different FA sequences and one TR sequence

are used and they are shown in Figure 3.1. Init 1 will also be taken as the conventional sequence.

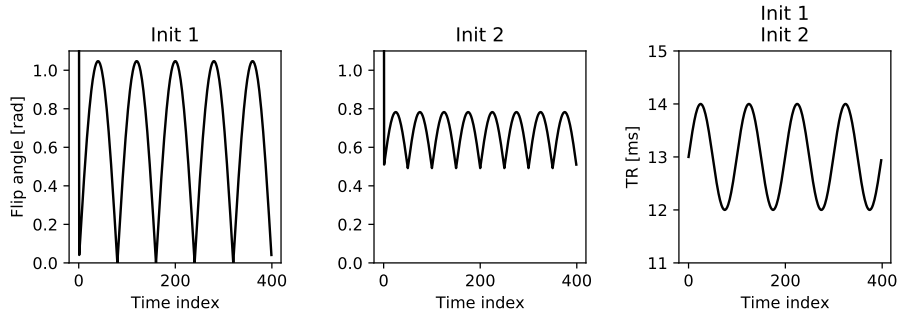


Figure 3.1: Two different initialisations of the SLSQP optimisation algorithm. The FA sequences start with a 180° inversion pulse.

3.3.2. OPTIMISATION PROBLEMS *Framework II*

The cost function for *Framework II* is based on the root mean square (RMS) of the relative error in the tissue maps of the relaxation parameters. These relative errors are predicted with the extended undersampling model presented in section 3.2. The error in the first term of the extended undersampling model from equation (3.19) is set to 0 as the error in this term cannot be suppressed by optimisation of the acquisition parameters. The ground truth for this model is a brain scan of a healthy volunteer (Nr. I).

The RMS of the tissue maps are defined as:

$$\text{RMS}_{T_1} = \sqrt{\frac{1}{N_{\text{vox}}} \left(\frac{T_1 - T_1^{\text{model}}}{T_1} \right)^2} \quad \text{RMS}_{T_2} = \sqrt{\frac{1}{N_{\text{vox}}} \left(\frac{T_2 - T_2^{\text{model}}}{T_2} \right)^2}, \quad (3.21)$$

where T_1 and T_2 are the true tissue parameters and T_1^{model} and T_2^{model} the model predictions. The amount of unmasked voxels is denoted with N_{vox} . For the same reasons as for *Framework I*, the following constraints are introduced for the optimisation:

$$\begin{aligned} \text{constr. } \textcircled{1}: \quad & \text{L.b.} \leq \alpha_n \leq 60^\circ \quad \forall n \in \{2, 3, \dots, N_J\} \\ \text{constr. } \textcircled{2}: \quad & |\alpha_{n+1} - \alpha_n| \leq 1^\circ \quad \forall n \in \{1, 2, \dots, N_J - 1\}. \end{aligned} \quad (3.22)$$

There were 6 different optimisations performed with *Framework II*, which are stated in table 3.1.

Table 3.1: Settings for the optimisation schemes.

	Cost function	N_J	Undersampling factor	L.b. constr. ①	Constr. ②
Opt A	$\text{RMS}_{T_1} + \text{RMS}_{T_2}$	400	1/32	10°	✓
Opt B	$\text{RMS}_{T_1} + \text{RMS}_{T_2}$	400	3/32	10°	✓
Opt C	$\text{RMS}_{T_1} + \text{RMS}_{T_2}$	200	2/32	10°	✓
Opt D	$\text{RMS}_{T_1} + \text{RMS}_{T_2}$	400	1/32	0°	✓
Opt E	$\text{RMS}_{T_1} + \text{RMS}_{T_2}$	400	1/32	10°	×
Opt F	RMS_{T_2}	400	1/32	10°	✓

For the optimisation the cost function is minimised as a function of the $N_J \times 1$ vector with flip angles $\vec{\alpha}$.

The optimisations are performed with two different initialisations to estimate if the result is close to the global minimum. Two different FA sequences are used and they are shown in Figure 3.2. Init 1 will also be taken as the conventional FA sequence. All sequences for *Framework II* use a constant TR of 15ms.

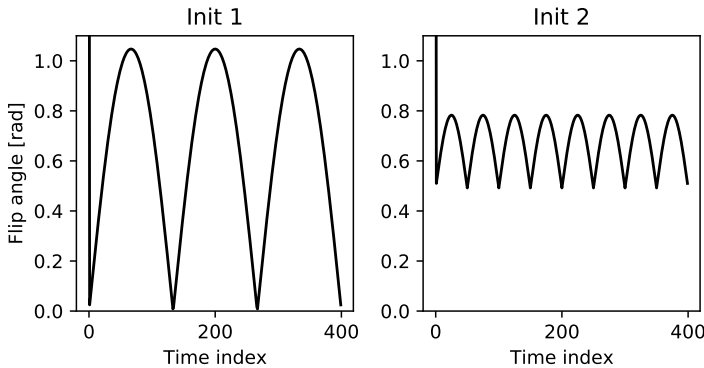


Figure 3.2: Two different initialisations of the SLSQP optimisation algorithm. Both sequences start with a 180° inversion pulse.

3.4. EXPERIMENTS

To demonstrate the benefit of using optimised sequences in vivo, multiple scans were acquired for a healthy volunteer (Nr. II) using a 3.0 T Philips Ingenia scanner (Best, The Netherlands). Two slices were acquired with a FOV of $224\text{mm} \times 224\text{mm}$, $1\text{mm} \times 1\text{mm}$ in plane resolution and 5mm slice thickness. The fully sampled acquisitions took around 8 minutes to acquire, while the undersampled acquisition took no longer than 30 seconds. The even amount of voxels in each dimension was made odd (225×225) by adding a row of zeros in each direction to have a natural centre of the image. This benefits the model as well as the analysis because the PSF can better approach a Kronecker delta function with odd dimensions. The dictionaries used for the reconstruction consisted of atoms with T_1 ranging from 150ms to 5000ms and T_2 ranging from 30ms to 1000ms both with

120 logarithmically spaced steps. When the restriction $T_2 \leq T_1$ is taken into account this results in a dictionary of 12,255 atoms. The k-space sampling is performed using spiral patterns shown in Figure 3.3.

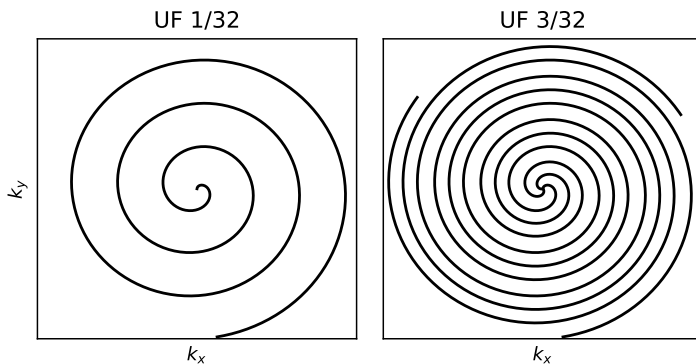


Figure 3.3: Spiral sampling patterns for an undersampling Factor (UF) of 1/32 and 3/32. Both patterns are rotated with $\frac{2\pi}{32}$ for every time index.

To assess the reconstructions using the undersampled images, they are compared to the fully sampled results. However, because of time constraints, the fully sampled scans are only acquired for two flip angle sequences: the conventional sequence and the sequence resulting from Opt A. The difference between these fully sampled scans is not significant as expected. The undersampled reconstructions using the flip angle sequence resulting from Opt B, C, D, E, and F are compared with the fully sampled results from Opt A. The reason we chose this fully sampled result as reference for Opt B to F is that it resulted in the lowest RMS of the relative error.

The numerical experiments in this research project are carried out using the same sampling patterns as for the in vivo results. Two different ground truths are used for the numerical analysis: the regular checkerboard ground truth is presented in Figure 3.4 and the more realistic brain phantom ground truth is shown in Figure 3.5.

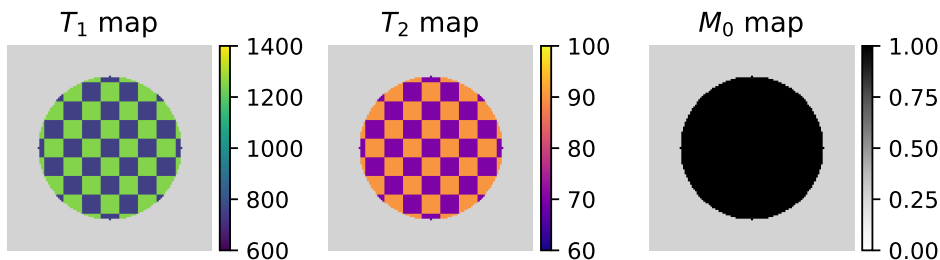


Figure 3.4: Chequerboard phantom for numerical simulations. The dimensions of this phantom are 121×121 . The parameter values are $(T_1, T_2) = (750, 70)$ ms and $(T_1, T_2) = (1250, 90)$ ms. Relaxation times are given in ms.

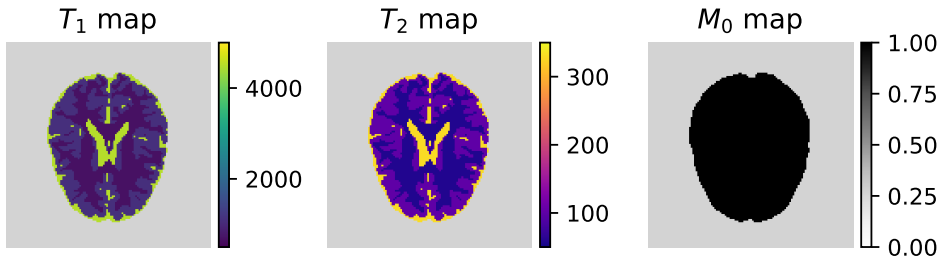


Figure 3.5: Brain phantom for numerical simulations based on component maps from [28]. The dimensions of this phantom are 121×121 . The (T_1, T_2) parameter values are chosen as white matter=(700,60) ms; grey matter=(1100, 102) ms; CSF=(4500, 330) ms. Relaxation times are given in ms.

The performance evaluation of the optimised sequences from Opt β is achieved using a Monte-Carlo simulation. A set of 20,000 different stochastic noise initialisations is added to the multi-component signal for which the M_0^a and M_0^b are determined using an NNLS algorithm. The reconstruction of the M_0 parameter is performed using a small dictionary with only two atoms to avoid sparsity problems. These atoms are the magnetisation evolutions belong to the tissues in the multi-component voxel under research. The NNLS algorithm only has to determine the M_0 weighting for both dictionary atoms from the multi-component signal. As the optimisations focus on reducing the Standard Deviation (SD) of the M_0 reconstruction for both tissues in a multi-component voxel, this property is studied in the results.

4

RESULTS

This chapter is structured as follows: first the numerical results from optimisation *Framework I* will be discussed in section 4.1. After this, the results for *Framework II* will be introduced in section 4.2. Here we will look at in vivo results and perform numerical analyses based on the optimisations with this framework. The chapter is concluded with a Fourier analysis that will shed light on the question of why the optimised sequence outperforms the conventional one.

4.1. OPTIMISATION *Framework I*

Optimisation *Framework I* focuses on reducing the stochastic errors in the reconstructed tissue maps. This is achieved by decreasing the Cramér-Rao bound using optimised acquisition parameters. B. Zhao et al. already performed this optimisation in a single-component context with tissue parameters $\theta = (T_1, T_2, \rho)$ using the isochromat summation approach [9]. The algorithm we developed using the EPG approach found the same optimisation result for the single-component case as shown in [29]. This ISMRM 2021 abstract by this author is presented in Appendix G.

4.1.1. MULTI-COMPONENT OPTIMISATION; OPT α

Besides the single-component optimisation, *Framework I* was also used for a multi-component optimisation. Figure 4.1 shows the Flip Angle (FA) and TR sequences resulting from Opt α in section 3.3. In this minimisation scheme the estimators on which the optimisation focuses are: $\hat{\theta} = (\hat{T}_1^a, \hat{T}_2^a, \hat{\rho}^a, \hat{T}_1^b, \hat{T}_2^b, \hat{\rho}^b)$, i.e. a mixture of two tissues. The optimisation was performed in a multi-component setting with White Matter (WM) and Grey Matter (GM) in one voxel (WM/GM optimisation).

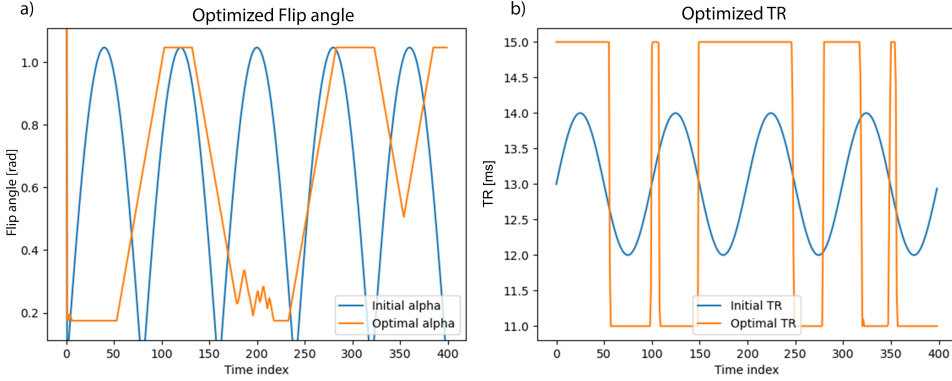


Figure 4.1: a) FA and b) TR sequences after WM/GM optimisation for multi-component MRF using *Framework I*; Opt α . Different initialisation of the optimisation problem returned the same result. The tissue parameters in the multi-component voxel are $\theta^{WM} = (700\text{ms}, 60\text{ms}, 0.3)$ and $\theta^{GM} = (1100\text{ms}, 102\text{ms}, 0.3)$.

Notice how the optimised sequence is very structured and often at a boundary of the optimisation space or moving towards a bound. The result is not evaluated for reasons discussed in chapter 5.

4.1.2. MULTI-COMPONENT OPTIMISATION; OPT β

Figure 4.1 shows the FA and TR sequences resulting from Opt β in section 3.1. Here the estimators on which the optimisation focuses are: $\hat{\theta} = (\hat{\rho}^a, \hat{\rho}^b)$. The optimisation was performed in two multi-component settings: one with white matter and grey matter in one voxel (WM/GM optimisation) and one with white matter and Myelin Water (MW) in one voxel (WM/MW optimisation).

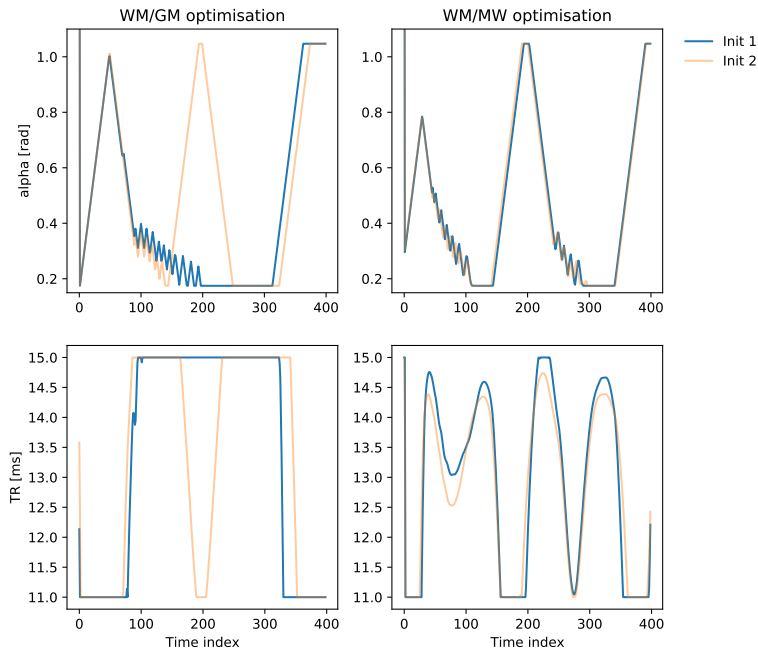


Figure 4.2: FA and TR sequences after WM/GM and WM/MW optimisation for multi-component MRF using *Framework I*; Opt β . The result for two different initialisations (see section 3.3) of the optimisation algorithm are shown. The tissue parameters for myelin water in the multi-component voxel are: $\theta^{MW} = (200\text{ms}, 20\text{ms}, 0.3)$. The cost-function value for the WM/GM optimisation is 6.08 and 6.38 for Init 1 and Init 2 respectively. The cost-function value for the WM/MW optimisation is 1.54 and 1.56 for Init 1 and Init 2 respectively.

The optimisations starting from Init 1 result in sequences which have the lowest value for the cost function compared to the results using Init 2. However, the results are very close together. The WM/MW optimisation shows practically the same outcome for both initialisations suggesting that this sequence is at a global minimum for the minimisation problem. Studying the optimisation process, we found that the FA sequence plays a significantly more important role in the optimisation than the TR sequence. This result was expected as the former acquisition parameter has a larger influence on the spin dynamics than the latter. The highly varying parts of the result appear not to be a numerical artefact. The cost function obtains a lower value with these highly varying parts than in a situation where they are smoothed (data not shown). This suggests that the encoding

capability of the sequence in a multi-component setting benefits from these parts.

The optimisations for *Framework I* took about 105 minutes to converge with the multi-processor implementation using 8 CPUs. The algorithm terminated when the change in the cost function was less than the pre-specified tolerance $\epsilon = 10^{-4}$.

In Figure 4.3, the magnetisation evolution for $M_0 = 0.3$ is presented for the conventional and the optimised sequences shown in Figure 4.2.

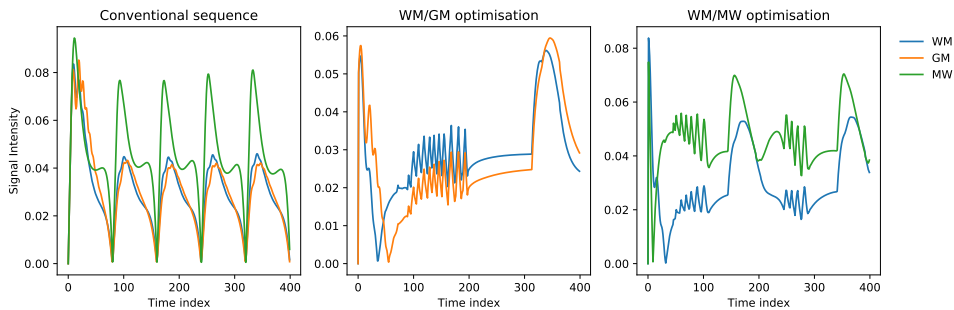


Figure 4.3: Absolute value of the signal from different tissues for $M_0 = 0.3$. The spin dynamics for the conventional sequence, the WM/GM optimisation and the WM/MW optimisation are presented.

From this figure we can observe that the signal from myelin water is distinctly larger than the signal for white matter resulting from the difference in T_1 relaxation times. A small numerical study revealed that the GM/WM optimised sequence decreased the inner-product between the WM and GM signals compared to this inner-product using the conventional sequence (using normalised signals: 0.96; 0.99, respectively). The same holds true for the WM and MW signals from the WM/MW optimisation and the conventional sequence (using normalised signals: 0.89; 0.97, respectively). This means that the signals from the optimised sequences are easier to differentiate from one another than the signals from the conventional sequences when using standard inner-product matching. Note from the inner-product values that WM and MW are easier to differentiate from one another than WM and GM using their respective optimisations.

The results of the MC evaluation are shown in Figure 4.4.

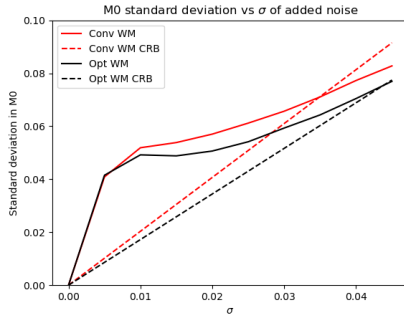
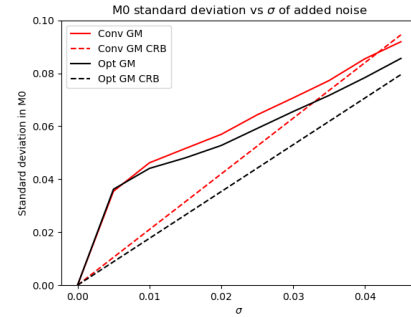
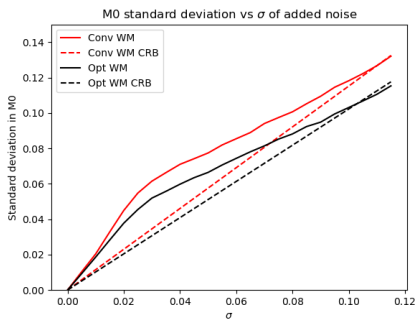
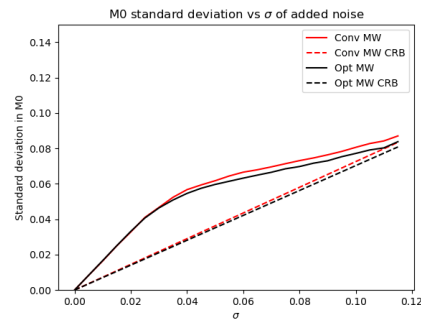
(a) SD in the M_0 reconstruction of white matter for the WM/GM optimisation.(b) SD in the M_0 reconstruction of grey matter for the WM/GM optimisation.(c) SD in the M_0 reconstruction of white matter for the WM/MW optimisation.(d) SD in the M_0 reconstruction of myelin water for the WM/MW optimisation.

Figure 4.4: Standard deviation (SD) in the reconstruction of M_0^a and M_0^b from a Monte-Carlo simulation with 20,000 noise initialisations. The results from the WM/GM and WM/MW optimisations are evaluated together with the results from the conventional sequence for comparison. The theoretical lower bound on the variance (CRLB) which the optimisations try to minimise are shown with dashed lines. Notice that the standard deviation of the added noise is plotted for two different domains.

From this evaluation we can observe that even though the optimisations outperform the conventional sequence, the difference is not very large. Notice that for large standard deviations of the added noise, the evaluated SD for the M_0 parameters gets under the Cramér-Rao Lower Bound.

In the next paragraph some observations with respect to these results are presented together with the intuition behind them. As the CRLB in this setting depends on the derivative of the magnetisation to M_0 which is a linear parameter in the magnetisation, the intuition can be easily backed-up with the underlying mathematics.

Notice that the standard deviation for white matter is lower in a multi-component voxel with myelin water than it is with grey matter. This implies that it is easier to estimate

the parameter M_0^{WM} when white matter is in a voxel with myelin water, than when it is in a voxel with grey matter. This can be explained by noting that WM and MW are easier to differentiate from one another than WM and GM as the tissue parameters are further apart and the inner product of their signal is lower (see discussion under Figure 4.3). Furthermore, notice that in the WM/MW optimisation, the CRLB for myelin water barely changes. This is because myelin water has a larger signal than white matter. This implies that the added noise will have relatively less impact on the signal-to-noise ratio for myelin water which results in a lower standard deviation for the reconstruction of M_0^{MW} . For this reason the WM/MW optimisation focuses on reducing the variance in the M_0^{WM} reconstruction as it can gain more here. This fact can be backed-up easily using the underlying mathematics.

4.2. OPTIMISATION *Framework II*

Optimisation *Framework II* focuses on reducing the undersampling error in the reconstructed tissue maps. This is achieved using the extended undersampling model from section 3.2.4 to predict the undersampling error for a certain set of acquisition parameters. The RMS of this undersampling error prediction for a tissue map will serve as the cost function for which the optimisation is performed (see section 3.3). The stochastic term \mathcal{E}_3 in equation (3.11) is left out of the optimisations and analyses as its effect were considered marginal.

4.2.1. EFFECT OF THE TRANSMIT PHASE

The transmit phase introduced in the extended undersampling model from section 3.2.4, is of major importance for the resulting undersampling error. To demonstrate its influence and to show that the extended undersampling model predictions are accurate, a short numerical study using three different transmit phase maps is performed. The true MRF error with which the model predictions are compared, is obtained by undersampling the noise-free signals and matching them to a pre-computed dictionary. This true error is referred to as the ‘simulation’.

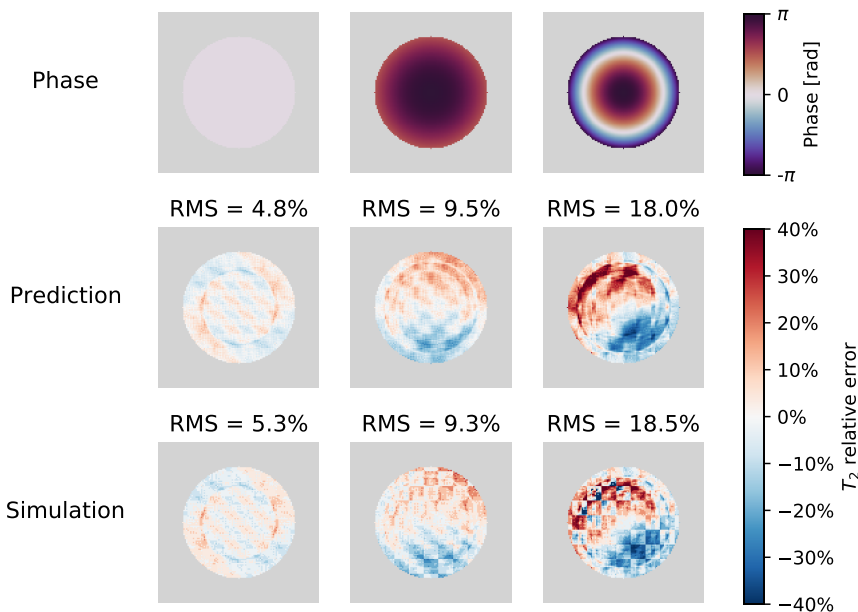


Figure 4.5: Effect of the transmit phase on the relative errors in T_2 reconstruction. The chequerboard phantom from Figure 3.4 is used as ground truth. The columns in this figure show the transmit phase and the resulting model prediction and simulation of the relative errors.

From this figure we can conclude that the transmit phase is a very important system parameter in the reconstruction, leading to an almost four-fold increase in T_2 -RMS com-

pared to a constant phase. The structure of the relative error as well as its magnitude highly depend on the spatial configuration of the transmit phase. It can be seen that the predictions from the extended undersampling model are in very good agreement with the undersampling errors from the simulation.

4.2.2. OPTIMISED SEQUENCES

The optimisations are performed using the settings from section 3.3. The results for the two different initialisations of the optimisation algorithm are shown in Figure 4.6.

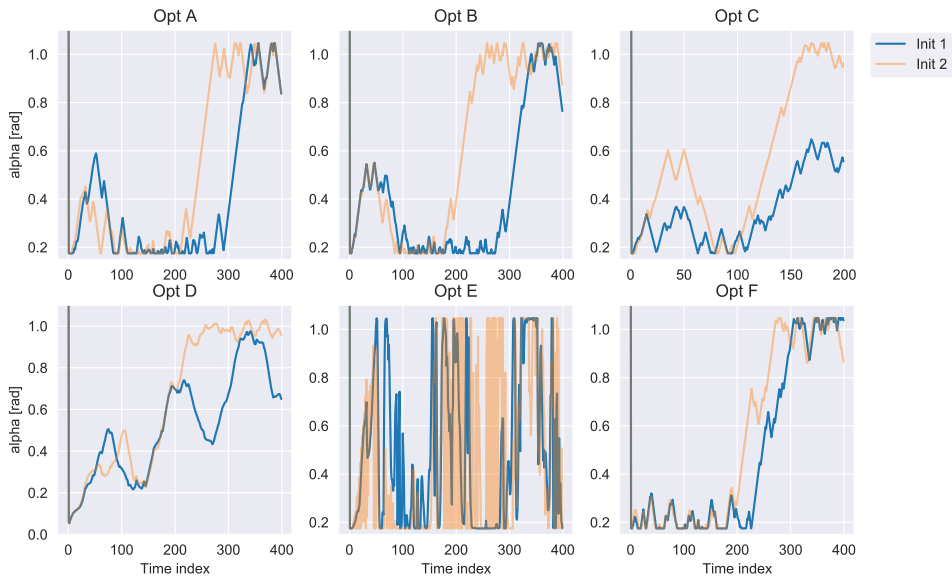


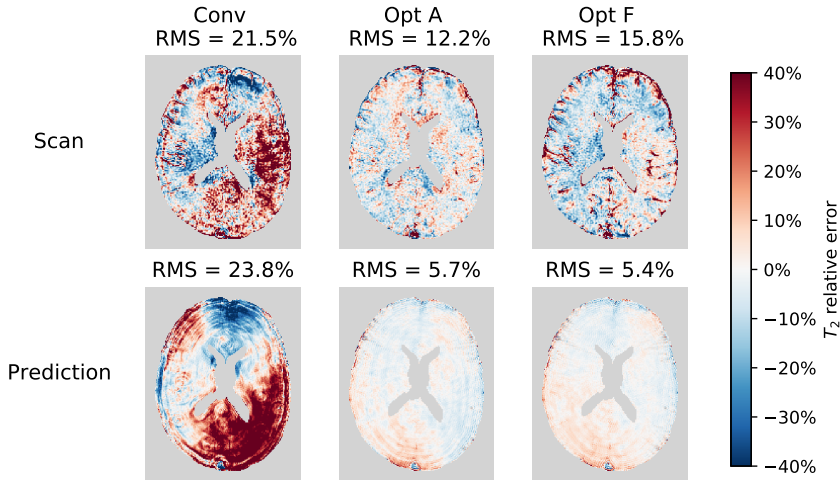
Figure 4.6: Optimised FA sequence using different optimisation schemes described in section 3.3 for *Framework II*. The result for two different initialisations (see section 3.1) of the optimisation algorithm are shown. All optimised acquisition schemes start with a 180° inversion pulse.

The optimisations starting from Init 1 result in the lowest cost function value, although the results are very close together as shown in Figure 4.14 in the next section. These sequences are used for the scans in the next section. For all optimisation schemes except for Opt E, the results from both initialisations show structural similarity. Note that the result from Opt E is highly varying as the smoothing constraint is missing here. The only major difference in the results from Opt A and Opt F is the peak in the first 100 time indices. This confirms that the manipulation of the spin dynamics directly after the 180° inversion pulse determines the T_1 encoding.

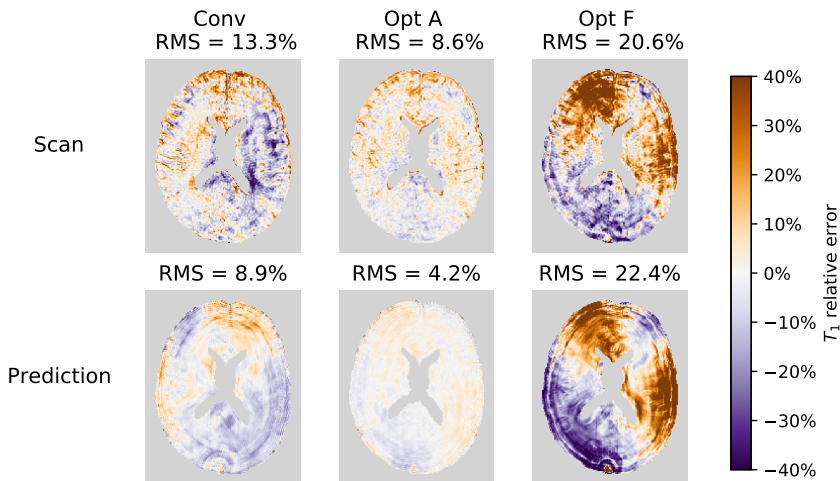
The optimisations for *Framework II* took about 1.5 days to converge with the multi-processor implementation using 8 CPUs for a single run. The algorithm terminated when the change in the cost function was less than the pre-specified tolerance $\epsilon = 10^{-4}$.

4.2.3. IN VIVO VALIDATION

To test the extended undersampling model developed in section 3.2, the predictions and the in vivo results from a healthy volunteer (Nr. II) are compared for a selection of sequences from Figure 4.7. For the model predictions the same sampling scheme is used as for the scans and fully sampled MRF maps of this volunteer are used as ground truth.



(a) Relative errors in the T_2 map.



(b) Relative errors in the T_1 map.

Figure 4.7: Relative errors in the tissue parameter maps for slice 1 of volunteer Nr. II. The predictions are made with the extended undersampling model from section 3.2. The RMS of the relative error is calculated by limiting all errors to $\pm 40\%$ to reduce the impact of outliers. For the acquisition, a spiral sampling pattern as discussed in section 3.4 is applied with an undersampling factor of $1/32$.

From these results we can conclude that the model performs very well in situations where the undersampling artefacts are the dominating source of error. This is the case for the T_2 map obtained with the conventional flip angle sequence and the T_1 map obtained with Opt F (the optimisation which did not consider the undersampling error in T_1). When the undersampling error is successfully suppressed by the optimisations, other sources of error that are not taken into account in the model become dominant such that the predictions are not accurate anymore.

The transmit phase for the fully sampled scan using the conventional flip angle sequence is shown in Figure 4.8. The transmit phase does not (or not noticeably) change for the other scans. In Figure 4.9 and 4.10 a region of interest (ROI) in the reconstructed parameter maps was selected to enable a more detail oriented comparison between the results from the conventional sequence and the sequence resulting from Opt A.

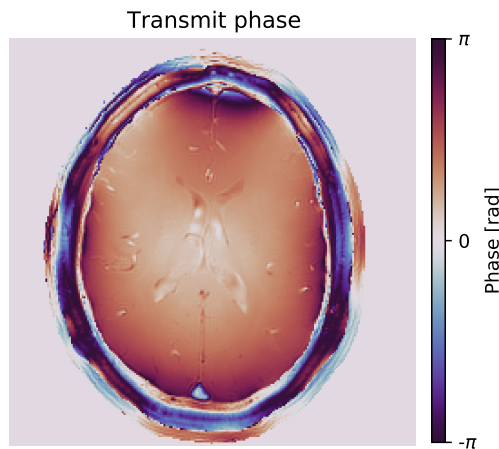


Figure 4.8: Transmit phase for the fully sampled scan using the conventional flip angle sequence.

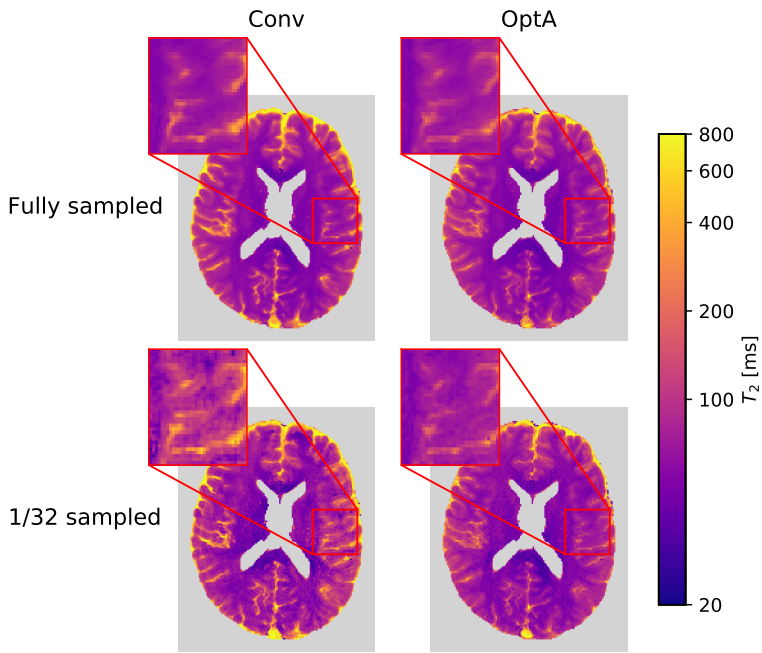
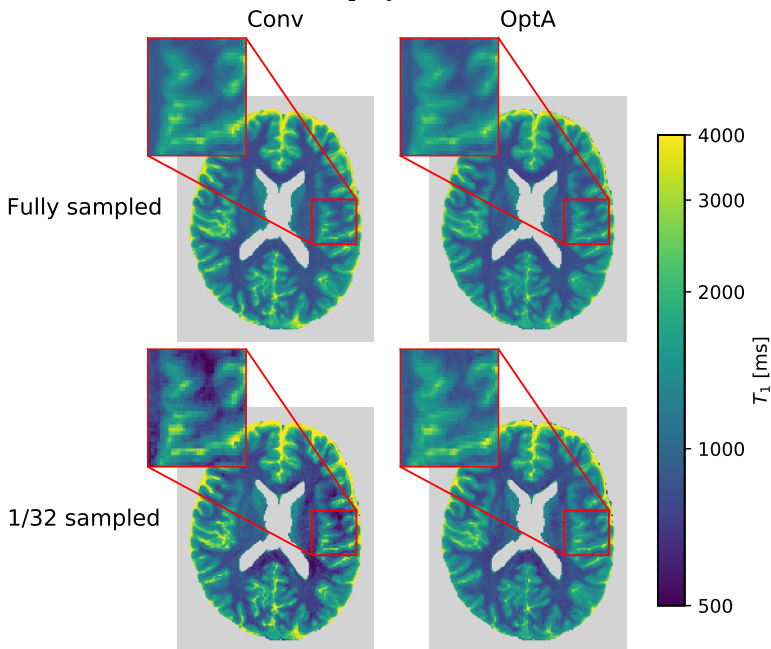
(a) T_2 maps; slice 1.(b) T_1 maps; slice 1.

Figure 4.9: Tissue parameter maps with inset figures for slice 1 of volunteer Nr. II. The conventional flip angle sequence and the sequence resulting from Opt A are used. For the acquisition, a spiral sampling pattern as discussed in section 3.4 is applied with an undersampling factor of 1/32.

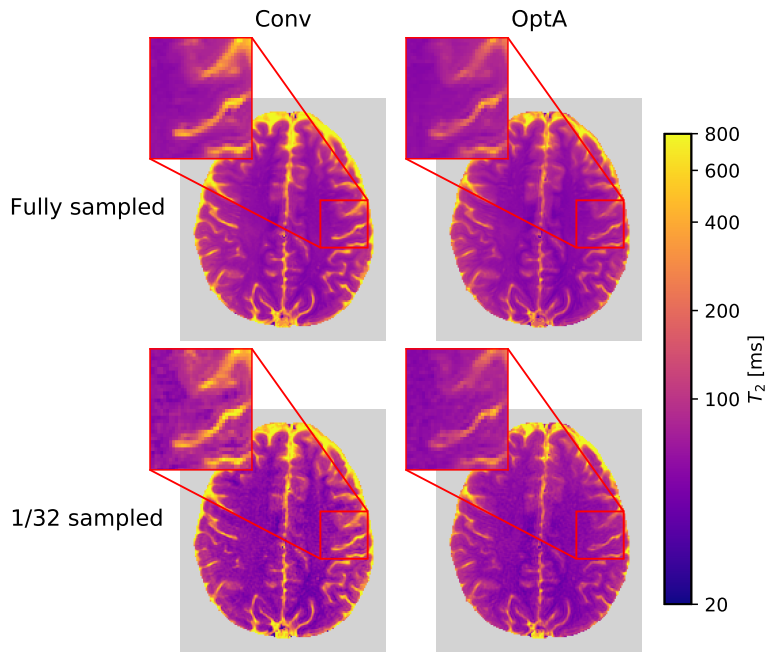
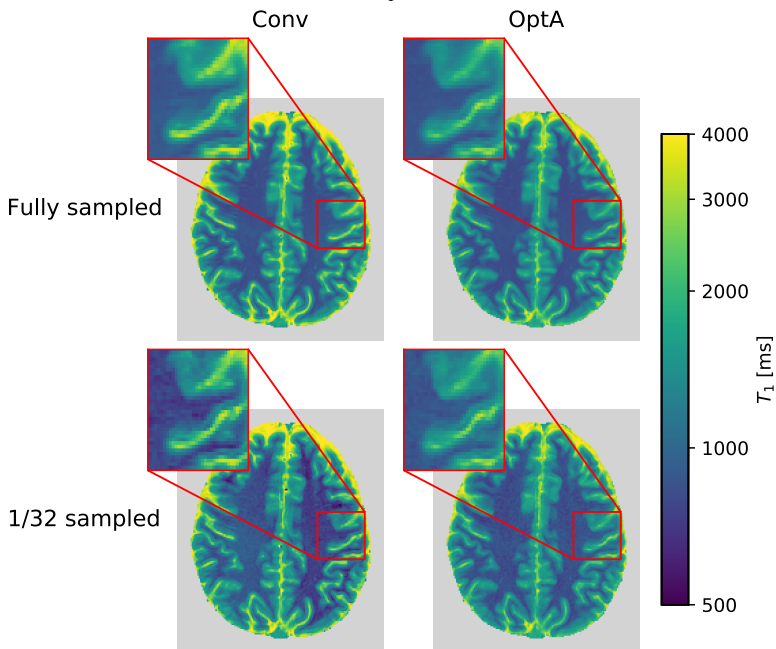
(a) T_2 maps; slice 2.(b) T_1 maps; slice 2.

Figure 4.10: Tissue parameter maps with inset figures for slice 2 of volunteer Nr. II. The conventional flip angle sequence and the sequence resulting from Opt A are used. For the acquisition, a spiral sampling pattern as discussed in section 3.4 is applied with an undersampling factor of 1/32.

The T_2 maps in Figure 4.9a clearly show less blurring of the CSF filled crevices with flip angle pattern from Opt A. For the T_1 maps in Figure 4.9b, there is no direct difference in blurring of the CSF filled crevices. However, grey matter T_1 is underestimated when using the conventional sequence while the optimised result shows a much more accurate reconstruction with respect to the fully sampled data. From these observations we conclude that the flip angle sequence from Opt A outperforms the conventional sequence. Note that the result from the two fully sampled sequences is in good agreement as expected. In Figure 4.10 similar effects can be observed despite the structural differences between the slices.

The relative error maps using the optimised sequences are presented in Figures 4.11 to 4.13 for two different brain slices.

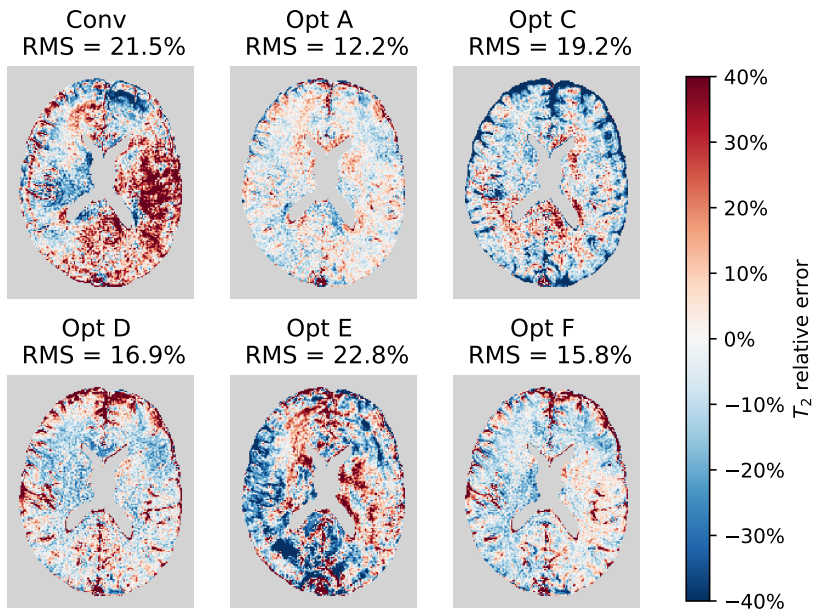
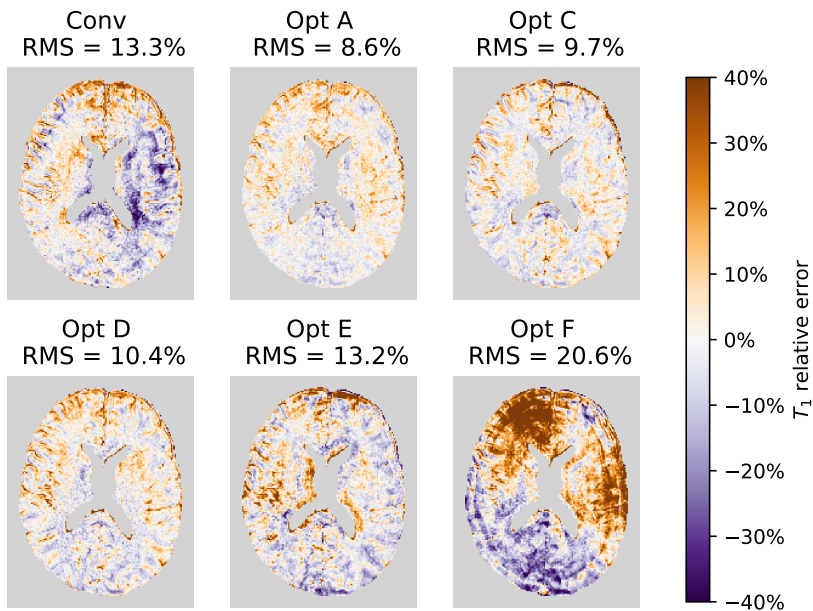
(a) Relative errors in the T_2 map.(b) Relative errors in the T_1 map.

Figure 4.11: Relative errors in the tissue parameter maps for slice 1 of volunteer Nr. II. The conventional flip angle sequence and the optimised sequences are used. For the acquisition, a spiral sampling pattern as discussed in section 3.4 is applied with an undersampling factor of $1/32$. The RMS of the relative error is calculated by limiting all errors to $\pm 40\%$ to reduce the impact of outliers.

The relative errors from slice 1 in Figure 4.11a show that applying the flip angle sequence from Opt A results in a distinct improvement in image quality compared to the conventional flip angle sequence. The magnitude of the error decreases and its distribution becomes more homogeneous. Note that the resulting relative errors from Opt A are more stochastic in nature than the relative errors from the conventional flip angle sequence. This suggests that the undersampling error is reduced to such a level that other, more stochastic, error sources become dominating.

Opt C, clearly performs worse than Optimisation A, although it requires the same scan time. It still outperforms the conventional scan in terms of RMS of the relative errors, although the difference for the T_2 map is small.

Applying the flip angle pattern from Opt D again results in an improvement over the conventional flip angle sequence, but performs worse than optimisation A. A short study on the conventional flip angle sequence and Opt A (the only sequences for which fully sampled data is available) showed that comparing the undersampled scan results with the fully sampled maps from the same sequence resulted in a lower RMS of the relative error than when the undersampled maps were compared to fully sampled maps from the other sequence. This observation suggests that the relatively small difference between the RMS of Opt A and Opt D might be due to the fact that the ground truth is a fully sampled scan using the flip angle sequence from Opt A.

The flip angle pattern from Opt E shows worse image quality than the conventional pattern. This suggests that smoothness of the magnetisation plays an important role in the performance of a flip angle sequence.

Opt F performs better than the conventional scan for T_2 in terms of RMS, but is outperformed by Opt A. Here the same footnote as with Opt D has to be placed: the ground truth is the fully sampled scan using the flip angle sequence from Opt A.

Figure 4.11b shows that the RMS of the relative errors in T_1 are lower than the RMS of the relative errors in T_2 . Approximately the same conclusions as for figure 4.11a can be drawn except for the results from Optimisation F. As this Optimisation did not take into account the undersampling error in T_1 in its cost function (see section 3.3) this error has increased.

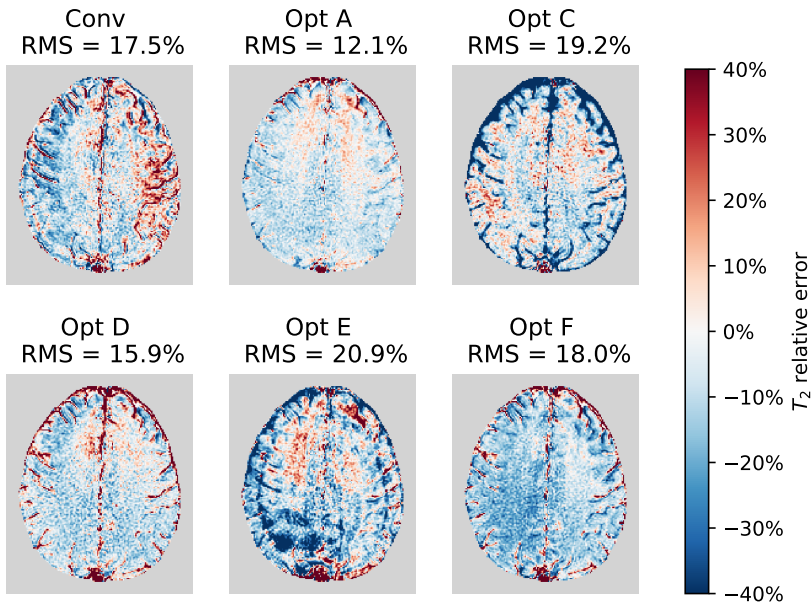
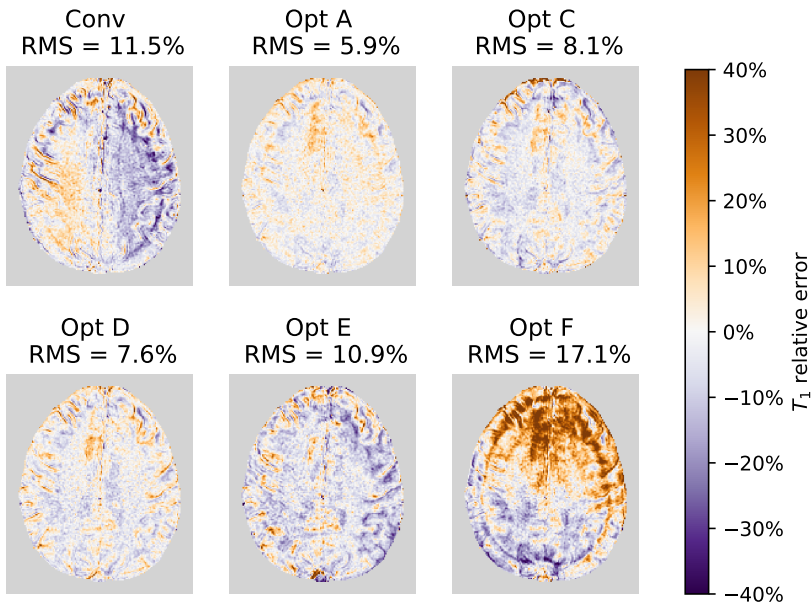
(a) Relative errors in the T_2 map.(b) Relative errors in the T_1 map.

Figure 4.12: Relative errors in the tissue parameter maps for slice 2 of volunteer Nr. II. The conventional flip angle sequence and the optimised sequences are used. For the acquisition, a spiral sampling pattern as discussed in section 3.4 is applied with an undersampling factor of $1/32$. The RMS of the relative error is calculated by limiting all errors to $\pm 40\%$ to reduce the impact of outliers.

The results from slice 2 in Figure 4.12 suggest the same qualitative conclusions as the results from slice 1. The relative improvement in the T_2 maps has decreased a little when comparing the conventional sequence and the sequence from Opt A. However, doing the same comparison for the T_1 maps, we noted that the relative improvement in T_1 maps has increased.

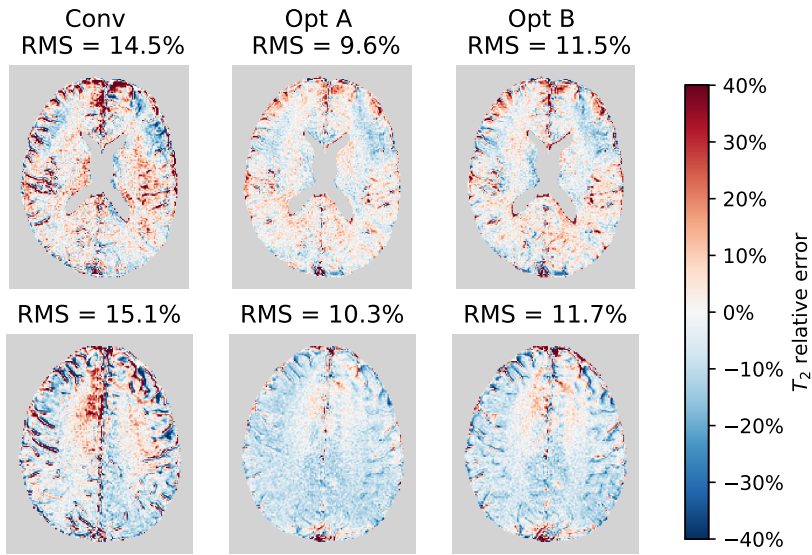
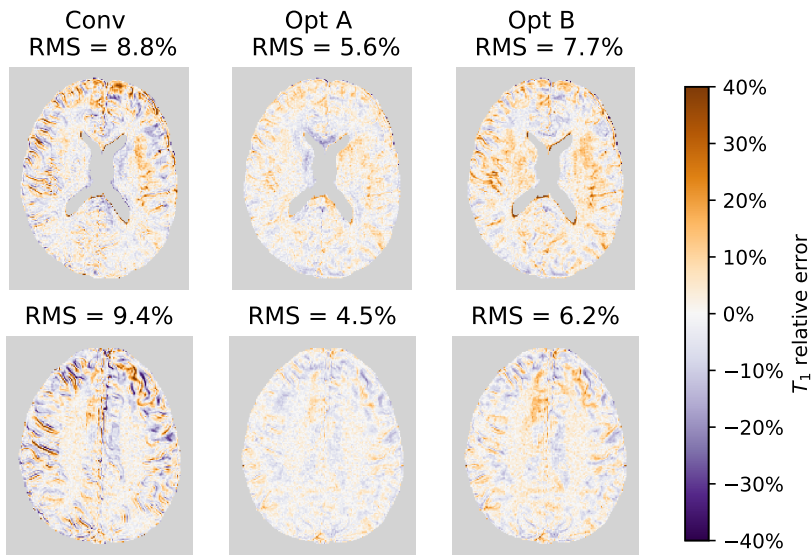
(a) Relative errors in the T_2 map.(b) Relative errors in the T_1 map.

Figure 4.13: Relative errors in the tissue parameter maps of volunteer Nr. II. The first row are the relative errors for slice 1 and the second row are the relative errors for slice 2. The conventional flip angle sequence and the optimised sequences are applied on both slices. For the acquisition, a spiral sampling pattern as discussed in section 3.4 is applied with an undersampling factor of 3/32. The RMS of the relative error is calculated by limiting all errors to $\pm 40\%$ to reduce the impact of outliers.

The results in Figure 4.13 show that the RMS of the undersampling error for 3/32 undersampled scans is lower than the undersampling error for 1/32 undersampled scans as expected. Opt A outperforms the conventional sequence when comparing the RMS of the relative error, but the improvement compared to the 1/32 undersampled case is decreased. This is natural as the undersampling error is lower when an undersampling factor of 3/32 is applied. This means that less improvement can be obtained by suppressing the remaining undersampling error as the magnitude of the other errors is expected not to improve as the optimisation does not take those into account. The flip angle sequence from Opt B outperforms the conventional sequence as well, but performs slightly worse than Opt A. Here the same footnote as with Opt D has to be placed: the ground truth is the fully sampled scan using the flip angle sequence from Opt A. Both slices show approximately the same behaviour.

4.2.3.1. QUANTITATIVE ANALYSIS OF THE SCAN RESULTS

In Figure 4.14 the RMS of the relative errors in T_1 and T_2 are given for the predictions made with the extended undersampling model.

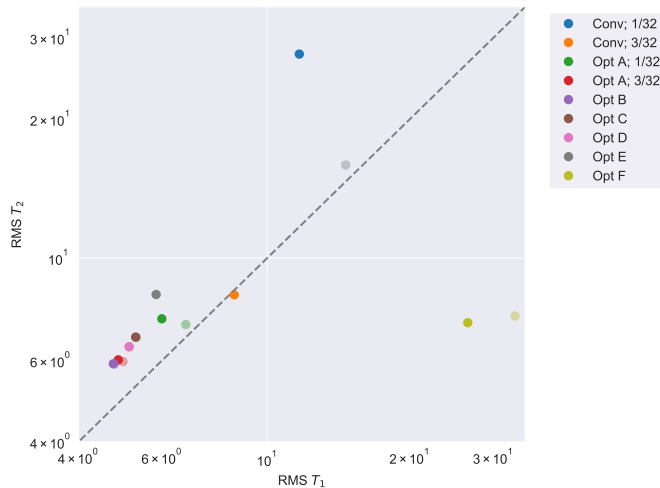


Figure 4.14: RMS of the relative errors in T_1 and T_2 for the predictions made with the extended undersampling model for slice 1 on a loglog scale. The bright dots are the results from Init 1 and the transparent dots are the results for Init 2. Note that the results from Init 1 and 2 are on top of each other for Opt B, Opt C and Opt D.

Note that the results for both initialisations of the same optimisation are close together for all optimisations except for Opt E. This fact, together with the structural similarity in the sequences resulting from both initialisations (see Figure 4.6), suggests that the optimisations are (close to) a global minimum. The sequences from Opt E show less structural similarity and their RMS values are relatively far apart. This suggests that the optimisation space for this scheme is such that the algorithm easily gets stuck in local minima before reaching the global minimum.

In Figure 4.15 the RMS of the relative errors in T_1 and T_2 are given for the scans made from slice 1.

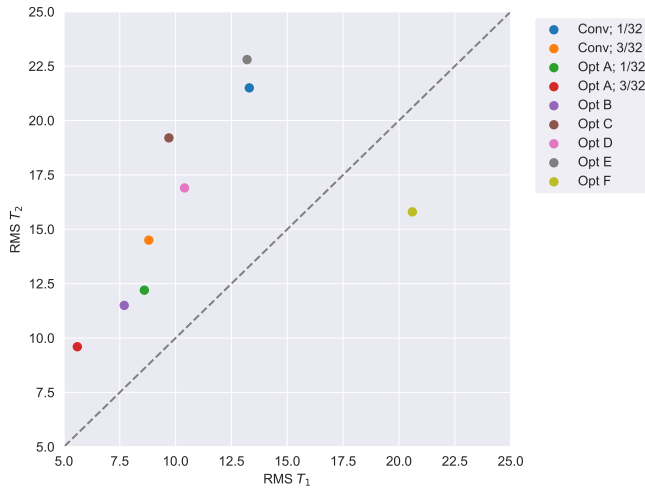


Figure 4.15: RMS of the relative errors in T_1 and T_2 for the scans made from slice 1.

Note that the RMS in the relative error is clearly higher for T_2 than for T_1 suggesting that this tissue parameter is harder to estimate. The sequence resulting from Opt F, which only focused on minimising the undersampling error in T_2 , clearly performs poorly for T_1 . This suggests that focusing on the error for one tissue parameter is not a sensible approach, as the error which is not taken into account can seriously increase.

4.2.4. MODEL BASED INSIGHTS INTO THE EFFECTS OF OPTIMISATION

To understand why the optimised sequences outperforms the conventional sequence a model-based qualitative analysis is performed. For this part the chequerboard and brain phantom, presented in Figures 3.4 and 3.5, are used.

A numerical optimisation is performed using the extended undersampling model from section 3.2.4 with the chequerboard phantom as ground truth. This optimisation focused only on reducing the undersampling error in T_2 using the RMS of the relative error as cost function. A constant density spiral with an undersampling factor of $1/32$ was applied with a rotation scheme as described in section 3.4. No phase was added to the chequerboard phantom and the stochastic term was neglected. The resulting optimised sequence is shown in Figure 4.16. The analyses performed in this section use this optimised sequence and described model parameters.

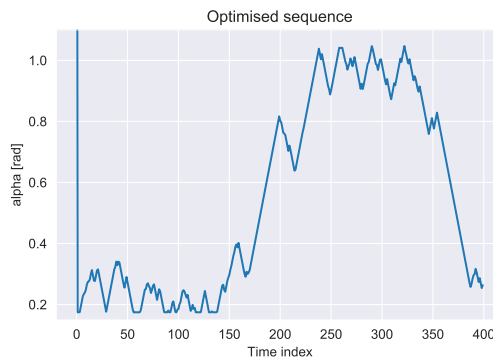


Figure 4.16: Optimised sequence using a chequerboard as ground truth. The optimisation algorithm was initialised with Init 1 from section 3.3.

The evolution of the magnetisation resulting from this optimised flip angle scheme is shown in Figure 4.17 together with the evolution for the conventional sequence for comparison. The tissue parameters are chosen as $(T_1, T_2, \rho) = (1000 \text{ ms}, 80 \text{ ms}, 1)$ as this is the θ_0 for the chequerboard phantom. The derivatives to the parameters are also presented in this figure. As the natural logarithm of the relaxation parameters is used in the model, the derivatives to $T_1' = \ln(T_1)$ and $T_2' = \ln(T_2)$ are used. Notice that the evolution of the magnetisation and the derivatives to the respective tissue parameters are much more constant for the optimised sequence compared to the conventional one.

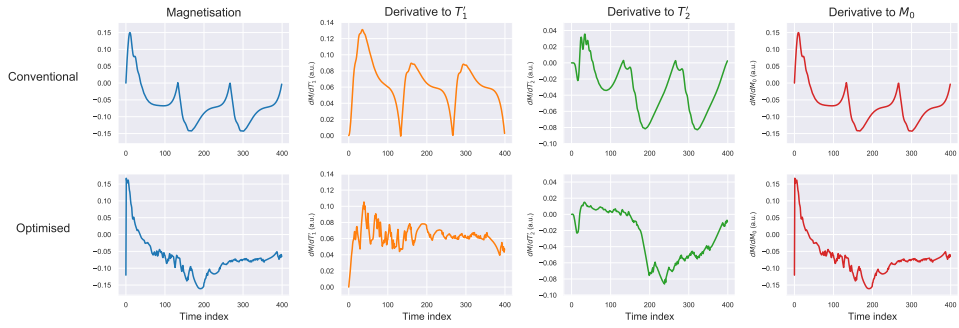


Figure 4.17: Evolution of the magnetisation with the derivatives to the parameters T'_1 , T'_2 and M_0 for the optimised and the conventional sequence using $(T_1, T_2, \rho) = (1000\text{ms}, 80\text{ms}, 1)$. The relaxation related derivatives are to $T'_1 = \ln(T_1)$ and $T'_2 = \ln(T_2)$ as these parameters are used in the model.

4.2.4.1. DESTRUCTIVE INTERFERENCE FOR ERROR REDUCTION

To study the behaviour of the different error terms, the extended undersampling model from section 3.2.4 is used with the model settings described above. Remember that the resulting undersampling error terms are separated as:

$$\theta_1^*(\vec{x}) = \text{Re}(f(P) * (\rho_0 \theta_1))(\vec{x}) + \mathcal{E}_1(\vec{x}; \boldsymbol{\xi}) + \mathcal{E}_2(\vec{x}; \boldsymbol{\theta}_1, \boldsymbol{\xi}), \quad (4.1)$$

where f is a linear operator on the PSF. The first term on the right hand side is an estimation for the true θ_1 and does not depend on the acquisition sequence. It can only be improved by using a better sampling scheme. The second and third term on the right hand side are the error terms. These terms do depend on the acquisition parameters $\boldsymbol{\xi}$ and can be optimised. The \mathcal{E}_1 -error term is closely related to the sampling density around the centre of k-space [8]. The \mathcal{E}_2 -error term also depends on the true tissue parameters. The sum over the index q (see equation (3.20)) in the definition of \mathcal{E}_2 , causes cross-talk effects between the different tissue maps. This means that the true value of T_1 can influence the reconstruction of T_2 and vice versa. Writing out the error terms from equation (4.1), the following expression was obtained in section 3.2.4:

$$\begin{aligned} \theta_{1,r}^*(\vec{x}) = & \left[\text{Re}(N)^{-1} \frac{1}{|\rho_0^*|^2} \text{Re} \left(\overline{\rho_0^*} N (P * (\rho_0 \omega \theta_1)) \right) (\vec{x}) \right]_r \\ & + \sum_{p=1}^3 \text{Re}(N)_{r,p}^{-1} \frac{\mathbf{E}_{1,p}(\vec{x}; \boldsymbol{\xi})}{|\rho_0^*|^2} + \sum_{p=1}^3 \text{Re}(N)_{r,p}^{-1} \frac{\mathbf{E}_{2,p}(\vec{x}; \boldsymbol{\theta}, \boldsymbol{\xi})}{|\rho_0^*|^2}, \end{aligned} \quad (4.2)$$

where the meaning of \mathbf{E}_1 and \mathbf{E}_2 is presented in equation (3.20) and the index r defines the tissue parameter. In this section we are going to study \mathcal{E}_1 and \mathcal{E}_2 as a weighed sum of the matrices $\frac{\mathbf{E}_{1,\{0,1,2\}}}{|\rho_0^*|^2}$ and $\frac{\mathbf{E}_{2,\{0,1,2\}}}{|\rho_0^*|^2}$ respectively. From this analysis we will see what the effect of the optimisation is. Notice that the weights of the aforementioned sets of three matrices come from the inverse Fisher information matrix that is also dependent on the acquisition parameters. As the cost function of the optimisation in this section only depends on the undersampling error in T_2 , the presented results focus on this tissue parameter ($r = 1$). The inverse Fisher information matrices are presented for the conventional and optimised acquisition parameters:

$$\text{Re}(N_{\text{conv}})^{-1} = \begin{bmatrix} 1.05 & 0.40 & 0.45 \\ 0.40 & 4.30 & -1.55 \\ 0.45 & -1.55 & 1.25 \end{bmatrix} \quad \text{Re}(N_{\text{opt}})^{-1} = \begin{bmatrix} 1.76 & 0.51 & 0.84 \\ 0.51 & 3.40 & -0.86 \\ 0.84 & -0.86 & 1.10 \end{bmatrix}. \quad (4.3)$$

Focusing on the T_2 tissue parameters implies that the weights for the matrices $\frac{\mathbf{E}_{1,\{0,1,2\}}}{|\rho_0^*|^2}$ are $\text{Re}(N)_{1,\{0,1,2\}}^{-1}$ respectively. The same holds for \mathcal{E}_2 .

In Figure 4.18, \mathcal{E}_1 and the $\frac{\mathbf{E}_{1,\{0,1,2\}}}{|\rho_0^*|^2}$ are presented for tissue parameter T_2 . In Figure 4.19, \mathcal{E}_2 and the $\frac{\mathbf{E}_{2,\{0,1,2\}}}{|\rho_0^*|^2}$ are presented for tissue parameter T_2 .

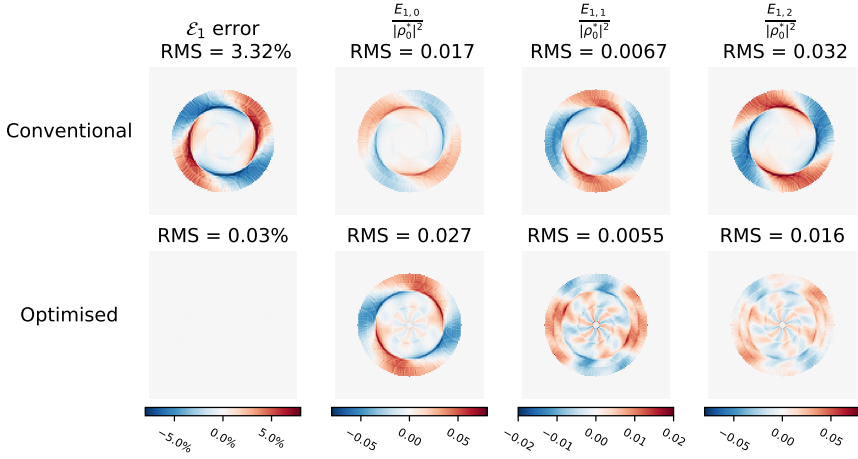


Figure 4.18: The \mathcal{E}_1 error for T_2 using the conventional and optimised flip angle sequence. The \mathcal{E}_1 error is a weighted sum of the matrices $\frac{E_{1,\{0,1,2\}}}{|\rho_0^*|^2}$ where the weights are determined by the inverse Fisher information matrix: $\text{Re}(N)_{1,\{0,1,2\}}^{-1}$.

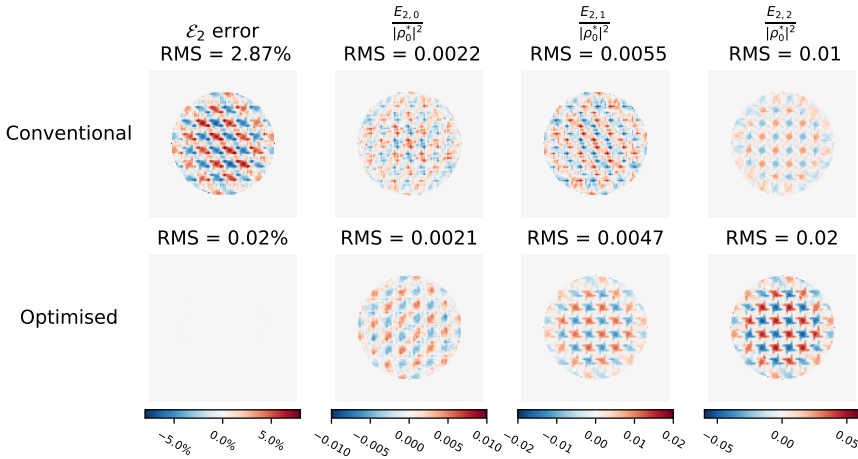


Figure 4.19: The \mathcal{E}_2 error for T_2 using the conventional and optimised flip angle sequence. The \mathcal{E}_2 error is a weighted sum of the matrices $\frac{E_{2,\{0,1,2\}}}{|\rho_0^*|^2}$ where the weights are determined by the inverse Fisher information matrix: $\text{Re}(N)_{1,\{0,1,2\}}^{-1}$.

Note that the optimisation does not significantly reduce the magnitude of the matrices $\frac{E_{1,\{0,1,2\}}}{|\rho_0^*|^2}$ and $\frac{E_{2,\{0,1,2\}}}{|\rho_0^*|^2}$, but rather modifies their shape such that they interfere destructively in the weighted sum. The optimisation tweaks the convolution kernels $S_{\text{resid};p}^{(1,0)}$ and

$S_{\text{resid};p,q}^{(1,1)}$ and the inverse FIM to obtain the reduction in \mathcal{E}_1 and \mathcal{E}_2 errors. Although the physical significance of these observations is marginal, they are interesting from a modelling perspective.

Figure 4.20 shows the total relative error divided into relative errors from the first term of equation (4.1) (the PSF error) and the relative errors from the second and third term (\mathcal{E}_1 and \mathcal{E}_2) for the checkerboard phantom.

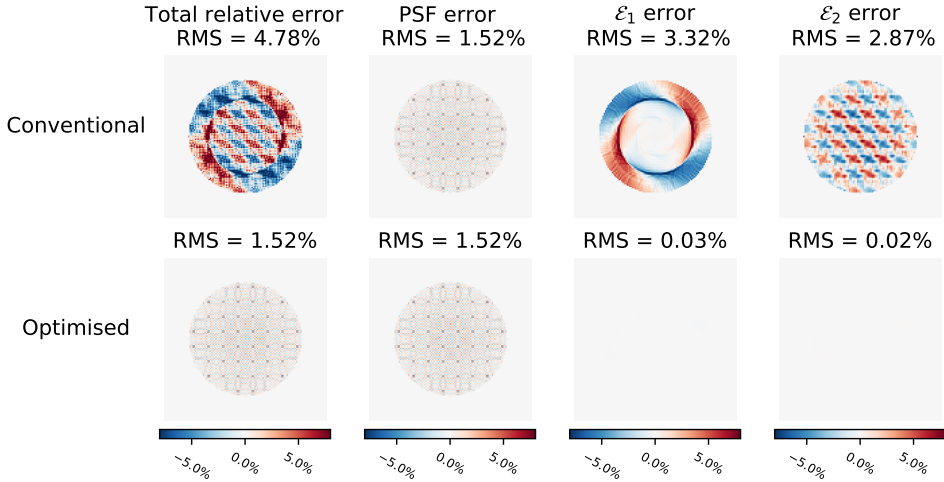


Figure 4.20: Total undersampling error for the T_2 reconstruction, divided into its individual components for the checkerboard phantom (see Figure 3.4).

Notice that the total relative error for the optimised sequence merely consists of PSF error which cannot be optimised using the acquisition parameters ξ . The optimisation succeeds in eliminating the acquisition dependent error terms \mathcal{E}_1 and \mathcal{E}_2 .

Figure 4.21 shows the total relative error divided into relative errors from the first term of equation (4.1) (the PSF error) and the relative errors from the second and third term (\mathcal{E}_1 and \mathcal{E}_2) for the brain phantom.

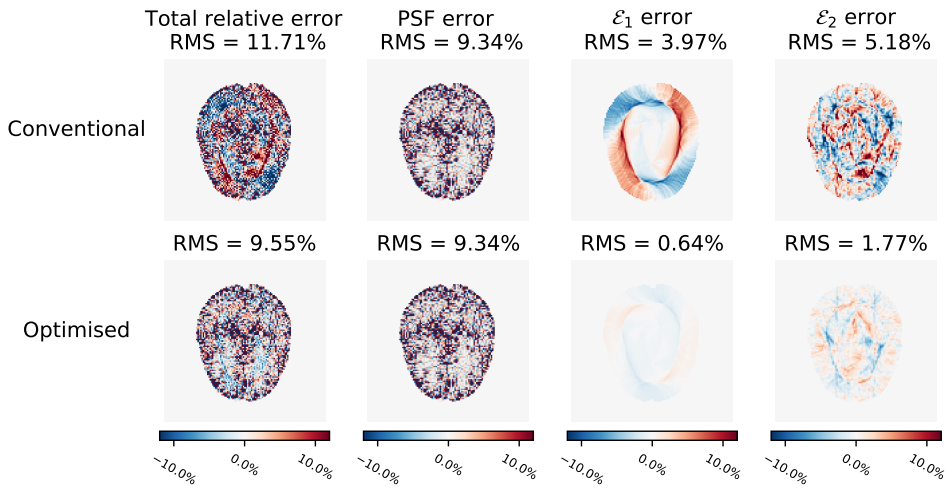


Figure 4.21: Total undersampling error for the T_2 reconstruction, divided into its individual components for a brain phantom (see Figure 3.5).

Despite the fact that the optimised sequence is obtained using a checkerboard as ground truth, it is still able to effectively reduce the \mathcal{E}_1 and \mathcal{E}_2 errors for the brain phantom. Notice that the structure of the brain phantom as well as the tissues present in it, fairly differ from the checkerboard. For \mathcal{E}_1 the reduction was expected as the only dependence on the ground truth for this error term is via ρ_0 which is merely a mask for the air around the object. The difference in ρ_0 for the checkerboard and the brain phantom is small suggesting that the optimisation should also perform well on the brain phantom, which it does. The fact that the \mathcal{E}_2 error reduces is more surprising as this term strongly depends on the true tissue parameters θ_1 . However, do note that the error reduction for this term is less than the reduction for \mathcal{E}_1 as expected. The reason why the optimised sequence also reduces the \mathcal{E}_2 term when using a ground truth that strongly differs from the ground truth on which the optimisation is based, is given using Fourier analysis in Appendix F. The next section focuses on a Fourier analysis for the \mathcal{E}_1 error, but shows overlap with the \mathcal{E}_2 analysis.

4.2.4.2. FOURIER ANALYSIS

To analyse why the optimisation in Figure 4.16 performs better than the conventional sequence, a Fourier analysis of the different error terms \mathcal{E}_1 and \mathcal{E}_2 is performed. Again using the extended undersampling model from section 3.2.4 ignoring a potential transmit phase and stochastic term, the error terms can be rewritten into:

$$\begin{aligned}\mathcal{E}_{1,r}(\vec{x}) &= \text{Re}\left(\text{Re}(N)_{r,p}^{-1} S_{\text{resid};p}^{(1,0)}(\vec{x}) * \rho_0(\vec{x})\right), \\ \mathcal{E}_{2,r}(\vec{x}) &= \text{Re}\left(\sum_{q=1}^{N_\Theta} \text{Re}(N)_{r,p}^{-1} S_{\text{resid};p,q}^{(1,1)}(\vec{x}) * (\rho_0 \theta_{1,q})(\vec{x})\right).\end{aligned}\quad (4.4)$$

The index r denotes the different tissue parameter values. Note that multiplicative ρ_0^* terms are neglected as their influence is marginal. The Einstein notation (repeated indices imply summation) is used for index p from now on, to increase the readability.

The Fourier transform of the term inside the real operator of $\mathcal{E}_{1,r}(\vec{x})$ will be written into a form that helps inference [8]. Generally the lower the values of this term in Fourier space, the lower the resulting $\mathcal{E}_{1,r}$ error. Using this analysis suggested by [8], we will try to create an understanding of why the optimised sequence performs better than the conventional one. The Fourier transforms are:

$$\begin{aligned}\mathcal{F}\left(\text{Re}(N)_{r,p}^{-1} S_{\text{resid};p}^{(1,0)}(\vec{x}) * \rho_0(\vec{x})\right) &= \text{Re}(N)_{r,p}^{-1} \hat{S}_{\text{resid};p}^{(1,0)}(\vec{k}) \cdot \hat{\rho}_0(\vec{k}), \\ \mathcal{F}\left(\sum_{q=1}^{N_\Theta} \text{Re}(N)_{r,p}^{-1} S_{\text{resid};p,q}^{(1,1)}(\vec{x}) * (\rho_0 \theta_{1,q})(\vec{x})\right) &= \sum_{q=1}^{N_\Theta} \text{Re}(N)_{r,p}^{-1} \hat{S}_{\text{resid};p,q}^{(1,1)}(\vec{k}) \cdot \mathcal{F}(\rho_0 \theta_{1,q})(\vec{k}).\end{aligned}\quad (4.5)$$

Here $\hat{\cdot}$ is used to represent that the variable is in Fourier space. The analysis below is for $\mathcal{E}_{1,r}$ only, but an equivalent approach can be used for $\mathcal{E}_{2,r}$. Note that $\text{Re}(N)_{r,p}^{-1} \hat{S}_{\text{resid};p}^{(1,0)}(\vec{k})$ is the relevant term for this analysis as it is the only one depending on the acquisition parameters. Using the definition $S_{\text{resid};p}^{(1,0)} = \sum_{j=1}^{N_j} (P_j(\vec{x}) - P(\vec{x})) \overline{\mathcal{D}M_{j;p}(\boldsymbol{\theta}_0)} M_j(\boldsymbol{\theta}_0)$, the expression below is obtained for a certain \vec{k} . As only one k-space vector can be chosen to perform the analysis on we will call our vector choice \vec{k}^* :

$$\begin{aligned}\text{Re}(N)_{r,p}^{-1} \hat{S}_{\text{resid};p}^{(1,0)}(\vec{k}^*) &= \text{Re}(N)_{r,p}^{-1} \sum_{j=1}^{N_j} \hat{P}_j(\vec{k}^*) \overline{\mathcal{D}M_{j;p}(\boldsymbol{\theta}_0)} M_j(\boldsymbol{\theta}_0) \\ &\quad - \text{Re}(N)_{r,p}^{-1} \hat{P}(\vec{k}^*) \sum_{j=1}^{N_j} \overline{\mathcal{D}M_{j;p}(\boldsymbol{\theta}_0)} M_j(\boldsymbol{\theta}_0) \\ &= \langle \mathbf{f}, \mathbf{g}_r \rangle - \langle \mathbf{h}, \mathbf{g}_r \rangle,\end{aligned}\quad (4.6)$$

where \mathbf{f} , \mathbf{g}_r and \mathbf{h} are temporal $N_j \times 1$ vectors given by:

$$\begin{aligned}f(j) &= \hat{P}_j(\vec{k}^*) \\ h(j) &= \hat{P}(\vec{k}^*) = \frac{1}{N_j} \sum_{j=1}^{N_j} \hat{P}_j(\vec{k}^*) \\ g_r(j) &= \text{Re}(N)_{r,p}^{-1} \mathcal{D}M_{j;p}(\boldsymbol{\theta}_0) \overline{M_j(\boldsymbol{\theta}_0)}.\end{aligned}\quad (4.7)$$

From equation (2.45) we know that $f(j)$ (the spatial Fourier transform of $P_j(\vec{x})$ at \vec{k}^*) is actually the spiral sampling pattern belonging to the read-out at time index j weighted with the density compensation function at \vec{k}^* . The temporal vector \mathbf{f} is called the sampling vector as it depends on the k-space sampling scheme. Furthermore, notice that the temporal vector \mathbf{h} is constant for all j . Let $\tilde{f}(v)$ denote the Fourier transform of the temporal vector \mathbf{f} : $\tilde{f}(v) = \sum_{j=1}^{N_j} f(j) e^{-i \frac{2\pi}{N_j} v(j-1)}$, $v = 0, 1, \dots, N_j - 1$. Using Parseval's theorem on the expression in equation (4.6) the following result is obtained for \vec{k}^* :

$$\text{Re}(N)_{r,p}^{-1} \hat{S}_{\text{resid};p}^{(1,0)}(\vec{k}^*) = \frac{1}{N_j} \langle \tilde{\mathbf{f}}, \tilde{\mathbf{g}}_r \rangle - \frac{1}{N_j} \langle \tilde{\mathbf{h}}, \tilde{\mathbf{g}}_r \rangle. \quad (4.8)$$

Here $\tilde{\cdot}$ is used to represent that the temporal vector is transformed to Fourier space. Using the property that the Fourier transform of the constant vector \mathbf{h} is a delta peak in k-space: $\tilde{h}(v) = \delta(v) \sum_{j=1}^{N_j} \hat{P}_j(\vec{k}^*)$, where $\delta(v)$ is the Kronecker-delta. Noting that for \vec{k}^* : $\tilde{f}(0) = \sum_{j=1}^{N_j} \hat{P}_j(\vec{k}^*)$, equation (4.8) can be rewritten into:

$$\begin{aligned} \text{Re}(N)_{r,p}^{-1} \hat{S}_{\text{resid};p}^{(1,0)}(\vec{k}^*) &= \frac{1}{N_j} \langle \tilde{\mathbf{f}}, \tilde{\mathbf{g}}_r \rangle - \tilde{f}(0) \overline{\tilde{g}_r(0)} \\ &= \frac{1}{N_j} \sum_{v=1}^{N_j-1} \tilde{f}(v) \overline{\tilde{g}_r(v)}. \end{aligned} \quad (4.9)$$

Using an equivalent approach for $\mathcal{E}_{2;r}$, we find for the acquisition dependent term:

$$\sum_{q=1}^{N_\Theta} \text{Re}(N)_{r,p}^{-1} \hat{S}_{\text{resid};p,q}^{(1,1)}(\vec{k}^*) = \frac{1}{N_j} \sum_{q=1}^{N_\Theta} \sum_{v=1}^{N_j-1} \tilde{f}(v) \overline{\tilde{g}_{r,q}(v)}, \quad (4.10)$$

with:

$$\begin{aligned} f(j) &= \hat{P}_j(\vec{k}^*) \\ g_{r,q}(j) &= \text{Re}(N)_{r,p}^{-1} \mathcal{D}M_{j;p}(\boldsymbol{\theta}_0) \overline{\mathcal{D}M_{j;q}(\boldsymbol{\theta}_0)}. \end{aligned} \quad (4.11)$$

4.2.4.3. \mathcal{E}_1 ERROR

For the analysis of the acquisition dependent term from equation (4.5), the vectors $\tilde{\mathbf{f}}$ and $\tilde{\mathbf{g}}_r$ are explored in further detail. The temporal vector \mathbf{g} is called the response vector as it depends on the acquisition parameters. As the optimisation in Figure 4.16 is only performed for the undersampling error in T_2 , this analysis will focus on $\mathcal{E}_{1;1}$ only, thus $r = 1$. Using the new form from equation (4.9), we know that the inner product of the vectors $\tilde{\mathbf{f}}$ and $\tilde{\mathbf{g}}$ (where $\tilde{g}_1(0)$ and $\tilde{f}(0)$ have been set to 0) determines the value of the Fourier transform of the acquisition dependent term $\text{Re}(N)_{r,p}^{-1} \hat{S}_{\text{resid};p}^{(1,0)}$ for \vec{k}^* . As the different k-space locations of the acquisition dependent term can be studied only one at the time, the vector \vec{k}^* is chosen close to the centre. The reason to chose this location is because the distribution of $\hat{\rho}_0$ is concentrated at the centre as it is the Fourier transform of a constant mask function. This implies that a k-space location close to the centre will probably be the most significant in the Fourier transform presented in equation (4.5), as the weighting from $\hat{\rho}_0(\vec{k})$ is high here. We purposely did not chose the centre of k-space,

but a point close to it, as the the Fourier transform of the acquisition dependent term is 0 in the centre as $\tilde{f}(v) = 0$ due to the density compensation weighting of the sampling spirals.

A small numerical study of the Fourier transform of the acquisition dependent term for the k-space location \vec{k}^* revealed that the inner product in equation (4.9) is mainly real. To visualise the inner product in this equation, the real and imaginary parts of the vectors \tilde{f} and \tilde{g}_1 are shown (where $\tilde{g}_1(0)$ and $\tilde{f}(0)$ have been set to 0). Note that the real part of the sum in equation (4.9) is the sum of inner products:

$$\operatorname{Re}\left(\operatorname{Re}(N)_{1,p}^{-1} \hat{S}_{\text{resid};p}^{(1,0)}(\vec{k}^*)\right) = \left\langle \operatorname{Re}(\tilde{f}^0), \operatorname{Re}(\tilde{g}_1^0) \right\rangle + \left\langle \operatorname{Im}(\tilde{f}^0), \operatorname{Im}(\tilde{g}_1^0) \right\rangle, \quad (4.12)$$

where \tilde{g}_1^0 and \tilde{f}^0 denote the vectors \tilde{g}_1 and \tilde{f} , where the $v = 0$ term has been set to 0. Figure 4.22 gives the vectors from both these inner products for the conventional and optimised case.

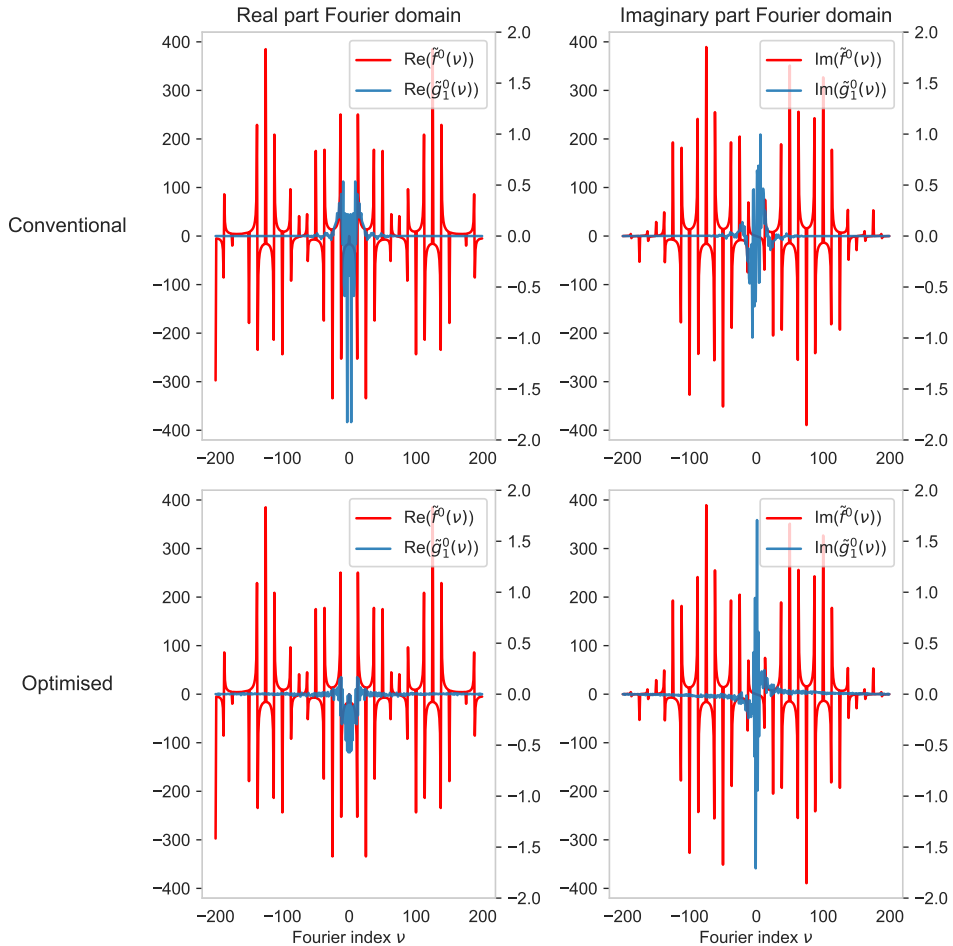


Figure 4.22: Fourier analysis of the sampling and response vectors. The left axis belongs to the red curve and the right axis to the blue curve.

Note that the non-zero Fourier indices from $\mathbf{g}_1^0(\nu)$ are higher for the conventional case compared to the optimised case for the real part of the spectrum. For the imaginary part, the vector $\mathbf{g}_1^0(\nu)$ for the conventional case is broader than the optimised one. Note that the imaginary part of the vector $\mathbf{f}^0(\nu)$ is very small close to $\nu = 0$, but grows bigger very fast. As the vector $\mathbf{g}_1^0(\nu)$ is more narrow in the optimised case, it decreases the inner product between the vectors $\mathbf{g}_1^0(\nu)$ and $\mathbf{f}^0(\nu)$ compared to the conventional case. Both these effects cause the sum of the inner products of $\langle \text{Re}(\tilde{\mathbf{f}}^0), \text{Re}(\tilde{\mathbf{g}}_1^0) \rangle$ and $\langle \text{Im}(\tilde{\mathbf{f}}^0), \text{Im}(\tilde{\mathbf{g}}_1^0) \rangle$ to be strongly decreased in the optimised case. This results in a lower Fourier term for $\text{Re}(N)_{r,p}^{-1} \hat{S}_{\text{resid};p}^{(1,0)}(\vec{k}^*)$ where \vec{k}^* is a vector close to the centre of k-space:

- Conventional case: $\text{Re}(N)_{1,p}^{-1} \hat{S}_{\text{resid};p}^{(1,0)}(\vec{k}^*) = 0.167$
- Optimised case: $\text{Re}(N)_{1,p}^{-1} \hat{S}_{\text{resid};p}^{(1,0)}(\vec{k}^*) = 0.002$.

This difference in magnitude indicates why the optimised sequence outperforms the conventional one. A small empirical study of other vectors \vec{k}^* close to the centre, revealed that the optimised sequence performed better for the majority of points. The same analysis for the error term $\mathcal{E}_{2;1}$ has been performed in Appendix F using more graphical guidance.

5

DISCUSSION

We have provided two models, which both focus on a different type of MRF error. The first model gives a prediction for the lower bound on the variance of the estimated tissue parameters, using a multi-component signal model. This lower bound is predicted, using the estimation theoretic Cramér-Rao lower bound which assumes unbiased estimators. The second model predicts the undersampling error in the context of MRF reconstruction, leveraging on techniques from perturbation theory. The perturbations can be decomposed into two main error terms (\mathcal{E}_1 and \mathcal{E}_2) that depend on the acquisition sequences for a first order approximation. Both these models were used to perform optimisations of the acquisition parameters to increase the accuracy or precision of the reconstructed parameter maps.

Based on *Framework I*; using the estimators for T_1 , T_2 and ρ for both tissues in the MC voxel (Opt α), we found that two different initialisations of the optimisation algorithm converge to the same sequence shown in Figure 4.1. This suggests that the presented result is a global minimum for the MC optimisation problem at hand. It was not possible to numerically evaluate the performance of the MC optimisation using the Non-Negative Least Squares algorithm. A multi-component analysis using this algorithm failed to separate the multi-component signal with added noise for a reasonably sized dictionary. This malfunctioning could be due to the ill-posedness of the problem at hand. Additional sparsity regularisation on the NNLS algorithm might improve this evaluation, although the simultaneous estimation of these 6 parameters for one voxel is rarely relevant.

Based on *Framework I*; using only the estimators for the proton density for both tissues in the MC voxel (Opt β), we found that the evaluation of the different optimisations could be performed in this setting as the relaxation times were assumed to be known. The variance reduction in the reconstructed parameters shown in Figure 4.4 was relatively small. The MC optimisation using the tissue parameters for white matter and myelin water is clinically the most interesting as myelin water serves as a bio marker

for myelin alterations, which is relevant for progressive diseases such as multiple sclerosis. The MC optimisation using the tissue parameters for white matter and myelin water did not (or barely) improve the variance in the reconstruction of the proton density for myelin water as shown in Figure 4.4d. This is because the signal from myelin water is larger than the signal from white matter which results in the optimisation focusing on the signal for white matter as it can gain a higher variance reduction here. For clinically relevant applications, one would like to reduce the variance in the myelin water reconstruction rather than the variance in the white matter reconstruction. Additional weights in the cost function should improve the variance optimisation for the myelin water reconstruction and could be used in follow up research.

A numerical analysis using *Framework II* showed that sequence optimisation makes that the undersampling error terms \mathcal{E}_1 and \mathcal{E}_2 get effectively suppressed in simulations. The transmit phase appeared to be an important parameter when modelling the undersampling errors as shown in Figure 4.5. Highly varying phase patterns cause the undersampling error to increase. Fortunately, the transmit phase for in vivo scans is relatively constant in the ROI as shown in Figure 4.8. Adding the transmit phase to the model improves its predictive power which was confirmed using in vivo scans. The in vivo scans depicted in Figure 4.11 show that the scans performed using the sequence from Opt A results in a distinct increase of the image quality compared to the results from the conventional sequence. The magnitude of the error decreased and simultaneously its distribution became much more homogeneous for two different brain slices. The undersampling error appears to be the dominating source of error in the in vivo scans when using the conventional sequence. This conclusion was drawn as the predicted errors from the undersampling model agree very well with the errors from the in vivo scan results in Figure 4.7. When using the sequence resulting from Opt A, the undersampling model cannot predict the errors in the in vivo scan anymore. This suggests that another source of error becomes dominating from which we conclude that the suppression of the undersampling error is successful. The optimisations resulting from optimisation problems with different settings and constraints, generally performed better than the conventional sequence, but not than the sequence from Opt A. Part of this effect can be explained by noticing that fully sampled reference data was only available for the conventional sequence and the sequence from Opt A. The optimisation for which the smoothness constraint on the flip angles was lifted (Opt E), performs worse than the conventional sequence. This suggests that smoothness of the flip angle sequence (and thus the resulting transverse magnetisation) is crucial for the reconstruction when using undersampled images. This observation was confirmed by other research projects [9, 30].

Further numerical analysis showed that an optimisation performed using a chequerboard phantom as ground truth also performs well on a brain phantom in terms of suppression of the acquisition dependent error terms (see Figure 4.21). The brain phantom contained different tissue parameters than the chequerboard phantom. This suggests that the optimisation is not highly dependent on the ground truth used in the model. It was confirmed by in vivo scans, for which the optimisations based the brain of volunteer Nr. I achieved serious suppression of the undersampling error in scans of volunteer Nr. II for two structurally different slices. This is a valuable property for the optimisations to

be clinically relevant.

Follow up research could be conducted to study whether the value of the tissue parameters or the structure of the ground truth has most influence on the optimisation result. It would be interesting to study whether the undersampling errors can be further minimised if the optimisation is tailored to the scanned region of interest based on previously acquired information from a short survey scan or scans part of a standard scan protocol. If the in vivo results benefit from an optimisation tailored to the specific ROI, a protocol where the short survey scan or standard scan is used for sequence optimisation followed by an optimised scan can be developed. As the optimisation time is currently on the order of days, this should be decreased by applying a dimension reduction of the optimisation space (e.g. using B-splines as discussed in the next paragraph) and rewriting the algorithm such that it is suitable for GPU computations. The k-space sampling plays an important role in the distribution of the undersampling error as shown in Appendix E. Follow up research should be conducted to find out if sequences optimised for a certain k-space acquisition also perform well for different sampling schemes.

One fundamental advantage of using the extended undersampling model for the optimisations, is that it contains an inherent separation of the spatial response function (the PSF) depending on the k-space sampling and the temporal function depending on the acquisition parameters. As the spatial response function does not need to be recalculated during the optimisation, the separation causes a speed-up of the optimisation algorithm with approximately a factor 20, depending on the sampling scheme. Although based on a fastly different model based on volume fractions, a similar separation of the spatial and temporal function already proved to be invaluable in sequence design as described in the work by S. Hu et al [31]. Furthermore, no dictionary matching is required as the error model is based on a least-square estimation of the tissue parameters. For iterative optimisation where the dictionary is required, it has to be updated for every iteration of the algorithm resulting in significantly longer computation times.

To further improve the optimisations, the following model improvements are suggested for follow up research. The multi-component *Framework I* might be extended with magnetisation transfer to make the MC signal model more realistic.

More complex reconstruction schemes might be incorporated in the undersampling model from *Framework II*. This extension would be interesting as advanced reconstruction algorithms might have a significant effect on the resulting errors. Due to the linearity of the SVD compression this reconstruction scheme might be implemented in the model with relative ease. A disadvantage of this approach is that the reconstruction using the SVD is based on a compression of the dictionary, which has to be calculated in each iteration [32].

A hybrid optimisation that suppresses the undersampling error and improves the variance in the estimators can be easily created by adding an extra term to the cost function based on the inverse Fisher information matrix calculated for *Framework II*.

The undersampling model might be used to optimise other acquisition parameters as

well. The number of time steps, the k-space sampling pattern and the TR times might be added to the model and could all be effectively optimised at once. A disadvantage of such approach is that the dimensions of the optimisation space will increase. This will drive up the computation time and as the optimisation problems are non-linear and non-convex, the algorithm can get stuck in a local minimum, instead of converging to the global minimum. To avoid this from happening, B-spline function might be introduced [33]. The B-spline functions are used such that the optimisation problem reduces to a minimisation of the amplitude of these functions. This results in a dimension reduction of the optimisation space. When choosing a limited number of B-spline functions, no additional constraints are required to guarantee the smoothness of the flip angle sequence.

An inherent problem of sequence optimisation in the context of MRF is that possible Bloch-model errors might harm the optimisations. The over-simplified nature of the Bloch equations creates a risk of introducing biases in the reconstruction of the parameter maps. An analysis of these effects is outside the scope of this work.

Although the clinical relevance of qualitative scans is subject for debate, MRF is gaining terrain as accepted quantitative MR imaging technique. The undersampling model could be used as a quick assessment tool for flip angles sequences applied in clinical research, to estimate the impact of the undersampling error. For spatially coherent undersampling errors such as the one from the conventional sequence in Figure 4.7, the model estimation of the error might even be used to increase image quality for reconstructions performed in the past, using a correction based on the predicted error.

6

CONCLUSION

Sequence optimisation for Magnetic Resonance Fingerprinting can be a valuable tool in increasing the accuracy and precision of the quantitative results. In this research project two different frameworks have been developed for sequence optimisation.

Framework I used the estimation theoretic Cramér-Rao lower bound to quantify the lower bound on the variance in the reconstruction of the tissue maps for a certain set of acquisition parameters. This lower bound was used for sequence optimisation, resulting in an increased precision in numerical simulations. The effects of this optimisation were relatively small.

Framework II estimated the undersampling error using a model that takes into account the interplay between the k-space sampling pattern and the the acquisition parameters such as the flip angle sequence. Optimisations using the model predictions are a new approach for suppressing the undersampling error which is usually (over) simplified as being spatially and temporal incoherent. Numerical simulations suggested that the undersampling error can be suppressed successfully using optimised flip angle sequences. In vivo scan results confirmed the validity of the undersampling model as well as the significant improvement in image quality using the optimised sequences.

For multi-component analysis, the optimisations using *Framework I* might be of interest. By merely changing the acquisition parameters more precise results can be obtained for e.g. the estimation of component maps for myelin water. These component maps are interesting as they act as a bio marker for myelin alterations that are relevant for monitoring progressive diseases such as multiple sclerosis.

For regular MRF T_1 and T_2 mapping, the optimisations using *Framework II* might improve the chances of MRF bringing quantitative imaging into clinical routine on short term. The undersampling error, which is the dominating source of error using the conventional sequence, can be significantly reduced using the optimised sequences or shorter scan times can be achieved.

ACKNOWLEDGEMENTS

I want to express my sincere gratitude to some people who have been invaluable in the making of this work.

First of all Dr. Frans Vos, whose directions and advice have been of great help to me. Frans always made it easy for me to ask questions and discuss results or new ideas. His experience in the medical imaging field, helped me get a good insight in this part of the scientific world.

Prof. Dr. Ir. Martin van Gijzen has provided me with advice and practical suggestions. His great theoretical knowledge in mathematics helped me understand the optimisation algorithms better. Furthermore, as a double degree student a lot of bureaucratic actions have to be undertaken and Martin helped me navigate in this maze.

A special word of thanks to Ir. Martijn Nagtegaal for his contribution. Martijn has extensive knowledge of MRI and always surprised me with how broad his comprehension of the field is. Besides a great mentor, he has helped to keep me on the right track when I lost myself into details and provided me with mental support. I will never forget the Zoom call till 4:00 a.m. to finish the ISMRM abstract I wanted to submit so bad. Without him the research would not have been what it is right now.

I would also like to thank Dr. Sebastian Weingärtner for the fruitful discussions we had. As an MRI physicist with an impressive grasp of the material, he had a sensible answer to virtually all my questions. Dr. Ir. Kirsten Koolstra also deserves a word here, as she was very helpful during the many evenings we scanned at the LUMC. I also want to thank my fellow students in the group: Emiel Hartsema and Maaïke Smit. We had nice discussions as well as a lot of laughs. Also Telly Ploem, Bram Simons and the rest of the Medical Imaging group have made my time in the student office a pleasant one.

Last but not least, I want to thank my family. My brother Moos for enduring my occasional moodiness. My parents for the stable family they have provided me with. I want to thank them for the love and support I have received over the years and for providing me with some perspective when I was stressed out. Without them, I would have lost my sanity a long time ago. I will be forever in their debt.

Delft, University of Technology
September 23, 2021

D.G.J. Heesterbeek

REFERENCES

- [1] Hai-Ling Margaret Cheng, Nikola Stikov, Nilesh R. Ghugre, and Graham A. Wright. Practical medical applications of quantitative MR relaxometry. *Journal of Magnetic Resonance Imaging*, 36(4):805–824, 2012.
- [2] Debra F. McGivney, Rasim Boyacıoğlu, Yun Jiang, Megan E. Poorman, Nicole Seiberlich, Vikas Gulani, Kathryn E. Keenan, Mark A. Griswold, and Dan Ma. Magnetic resonance fingerprinting review part 2: Technique and directions. *Journal of Magnetic Resonance Imaging*, 51(4):993–1007, July 2019.
- [3] Dan Ma, Vikas Gulani, Nicole Seiberlich, Kecheng Liu, Jeffrey L. Sunshine, Jeffrey L. Duerk, and Mark A. Griswold. Magnetic Resonance Fingerprinting. *Nature*, 495(7440):187–192, March 2013.
- [4] Jakob Assländer. A Perspective on MR Fingerprinting. *Journal of Magnetic Resonance Imaging*, 53(3):676–685, March 2021.
- [5] Ananya Panda, Bhairav B. Mehta, Simone Coppo, Yun Jiang, Dan Ma, Nicole Seiberlich, Mark A. Griswold, and Vikas Gulani. Magnetic resonance fingerprinting – An overview. *Current Opinion in Biomedical Engineering*, 3:56–66, September 2017.
- [6] Megan E. Poorman, Michele N. Martin, Dan Ma, Debra F. McGivney, Vikas Gulani, Mark A. Griswold, and Kathryn E. Keenan. Magnetic resonance fingerprinting Part 1: Potential uses, current challenges, and recommendations. *Journal of Magnetic Resonance Imaging*, 51(3):675–692, July 2019.
- [7] Martijn Nagtegaal, Peter Koken, Thomas Amthor, and Mariya Doneva. Fast multi-component analysis using a joint sparsity constraint for MR fingerprinting. *Magnetic Resonance in Medicine*, 83(2):521–534, July 2019.
- [8] C. C. Stolk and A. Sbrizzi. Understanding the Combined Effect of k-Space Under-sampling and Transient States Excitation in MR Fingerprinting Reconstructions. *IEEE Transactions on Medical Imaging*, 38(10):2445–2455, October 2019.
- [9] B. Zhao, J. P. Haldar, C. Liao, D. Ma, Y. Jiang, M. A. Griswold, K. Setsompop, and L. L. Wald. Optimal Experiment Design for Magnetic Resonance Fingerprinting: Cramér-Rao Bound Meets Spin Dynamics. *IEEE Transactions on Medical Imaging*, 38(3):844–861, March 2019.
- [10] Jakob Assländer, Dmitry S. Novikov, Riccardo Lattanzi, Daniel K. Sodickson, and Martijn A. Cloos. Hybrid-state free precession in nuclear magnetic resonance. *Communications Physics*, 2(1):1–12, June 2019.
- [11] Ouri Cohen and Matthew S. Rosen. Algorithm comparison for schedule optimization in MR fingerprinting. *Magnetic Resonance Imaging*, 41:15–21, September 2017.
- [12] L. I. Schiff and H. Snyder. Theory of the Quadratic Zeeman Effect. *Physical Review*, 55(1):59–63, January 1939.

- [13] Robert W. Brown, Yu-Chung N. Cheng, E. Mark Haacke, Michael R. Thompson, and Ramesh Venkatesan, editors. *Magnetic Resonance Imaging: Physical Principles and Sequence Design*. John Wiley & Sons Ltd, Chichester, UK, April 2014.
- [14] Da Smith. A Simple Derivation of the Bloch Equations for Localized Moment E.S.R. in Metals in the Presence of Anisotropy. *Australian Journal of Physics*, 26(4):475, 1973.
- [15] Jerry L. Prince and Jonathan M. Links. *Medical imaging signals and systems*. Pearson, Boston, 2 edition, 2015.
- [16] Michael Loecher and Oliver Wieben. k-Space. In Mushabbar A. Syed, Subha V. Raman, and Orlando P. Simonetti, editors, *Basic Principles of Cardiovascular MRI: Physics and Imaging Technique*, pages 13–23. Springer International Publishing, Cham, 2015.
- [17] Matthias Weigel. Extended phase graphs: Dephasing, RF pulses, and echoes - pure and simple. *Journal of Magnetic Resonance Imaging*, 41(2):266–295, February 2015.
- [18] Yun Jiang, Dan Ma, Nicole Seiberlich, Vikas Gulani, and Mark A. Griswold. MR fingerprinting using fast imaging with steady state precession (FISP) with spiral readout. *Magnetic Resonance in Medicine*, 74(6):1621–1631, 2015.
- [19] Klaus Scheffler and Stefan Lehnhardt. Principles and applications of balanced SSFP techniques. *European Radiology*, 13(11):2409–2418, November 2003.
- [20] M. Weigel, S. Schwenk, V. G. Kiselev, K. Scheffler, and J. Hennig. Extended phase graphs with anisotropic diffusion. *Journal of Magnetic Resonance*, 205(2):276–285, August 2010.
- [21] Tobias D. Faizy, Christian Thaler, Gabriel Broocks, Fabian Flottmann, Hannes Leischner, Helge Kniep, Jawed Nawibi, Gerhard Schön, Jan-Patrick Stellmann, André Kemmling, Ravinder Reddy, Jeremy J. Heit, Jens Fiehler, Dushyant Kumar, and Uta Hanning. The Myelin Water Fraction Serves as a Marker for Age-Related Myelin Alterations in the Cerebral White Matter – A Multiparametric MRI Aging Study. *Frontiers in Neuroscience*, February 2020.
- [22] Charles L. Lawson and Richard J. Hanson. *Solving Least Squares Problems*. Classics in Applied Mathematics. Society for Industrial and Applied Mathematics, January 1995.
- [23] Shaihan J. Malik, Rui Pedro A. G. Teixeira, and Joseph V. Hajnal. Extended phase graph formalism for systems with magnetization transfer and exchange. *Magnetic Resonance in Medicine*, 80(2):767–779, 2018. Number: 2.
- [24] Steven M. Kay. *Fundamentals of statistical signal processing: estimation theory*. Prentice-Hall, Inc., USA, 1993.
- [25] Richard D. Hoge, Remi K. S. Kwan, and G. Bruce Pike. Density compensation functions for spiral MRI. *Magnetic Resonance in Medicine*, 38(1):117–128, 1997.

- [26] William H. Press, Saul A. Teukolsky, William T. Vetterling, and Brian P. Flannery. *Numerical Recipes*. 3 edition, 1986.
- [27] Manushka V. Vaidya, Christopher M. Collins, Daniel K. Sodickson, Ryan Brown, Graham C. Wiggins, and Riccardo Lattanzi. Dependence of B1+ and B1- Field Patterns of Surface Coils on the Electrical Properties of the Sample and the MR Operating Frequency. *Concepts in Magnetic Resonance. Part B, Magnetic Resonance Engineering*, 46(1):25–40, February 2016.
- [28] C.A. Cocosco, V. Kollokian, R.K.-S. Kwan, and A.C. Evans. BrainWeb: Online Interface to a 3D MRI Simulated Brain Database. *NeuroImage*, 5(4). part 2/4, S425, 1997 – Proceedings of 3-rd International Conference on Functional Mapping of the Human Brain, Copenhagen, May 1997.
- [29] David Heesterbeek, Frans Vos, Martin van Gijzen, and Martijn Nagtegaal. Sequence optimisation for Multi-component analysis in Magnetic Resonance Fingerprinting. International Society for Magnetic Resonance in Medicine, May 2021.
- [30] J.B.M. Warntjes, O. Dahlqvist, and P. Lundberg. Novel method for rapid, simultaneous T1, T*2, and proton density quantification. *Magnetic Resonance in Medicine*, 57(3):528–537, 2007.
- [31] Siyuan Hu, Stephen Jordan, Rasim Boyacioglu, Ignacio Rozada, Matthias Troyer, Mark Griswold, Debra McGivney, and Dan Ma. A Fast MR Fingerprinting Simulator for Direct Error Estimation and Sequence Optimization. *arXiv:2105.11594 [eess]*, May 2021.
- [32] D. F. McGivney, E. Pierre, D. Ma, Y. Jiang, H. Saybasili, V. Gulani, and M. A. Griswold. SVD Compression for Magnetic Resonance Fingerprinting in the Time Domain. *IEEE Transactions on Medical Imaging*, 33(12):2311–2322, December 2014. Conference Name: IEEE Transactions on Medical Imaging.
- [33] Evan Scope Crafts and Bo Zhao. An Efficient Approach to Optimal Design of MR Fingerprinting Experiments with B-Splines. International Society for Magnetic Resonance in Medicine, May 2021.
- [34] Andrew Zangwill. *Modern electrodynamics*. Cambridge University Press, Cambridge, 2013.
- [35] Santiago Aja-Fernández and Gonzalo Vegas-Sánchez-Ferrero. *Statistical Analysis of Noise in MRI*. Springer International Publishing, Cham, 2016.

A

UNDERSAMPLING MODEL IN A MULTI-COMPONENT SETTING

The model presented in this section is not used for optimisations, nor was it used to generate simulation results. It is merely included in an effort to create an intuitive undersampling model in a multi-component setting.

For the model derived in section 2.6, single-component matching is assumed. This model is easily extended to a multi-component setting by adopting the additive signal model presented in section 2.4. If we assume there are two tissues in a voxel, call them a and b , $\boldsymbol{\theta}$ would change to $\boldsymbol{\theta} = (T_1^a, T_2^a, \rho^a, T_1^b, T_2^b, \rho^b)^T$ for the MC situation. In the multi-component case the equation for the parameter estimation would grow to 8 terms which have to be linearized instead of 2 terms for the single-component case. The final estimation for the tissue parameters in the multi-component setting would not be intuitive anymore.

For this reason, we adopt a volume fraction based approach where we again assume that a voxel consists of a finite number of tissues of interest with known tissue parameters. This signal model was also adopted by Hu et al. [31]. The only unknown is the volume fraction (\boldsymbol{p}):

$$\boldsymbol{M}(\boldsymbol{p}(\vec{x})) = \sum_{n=1}^{N_T} p_n(\vec{x}) \boldsymbol{M}(\boldsymbol{\theta}^n), \quad (\text{A.1})$$

where N_T is the total number of tissue types in a voxel, p_n the volume fraction of tissue type n and $\boldsymbol{\theta}^n$ the tissue parameters of tissue type n without the proton density (as this information is already present in the volume fractions). Non-negative least-square algorithms are able to recover the component maps from the mixed signals [3]. For a certain

signal $\mathbf{I}(\vec{x})$ the reconstructed component maps can be described as:

$$\mathbf{p}^*(\vec{x}) = \underset{\mathbf{p}}{\operatorname{argmin}} \|\mathbf{I}(\vec{x}) - \mathbf{M}(\mathbf{p})\|^2 \quad (\text{A.2})$$

where \mathbf{p} is an N_T dimensional vector. We assume that for realistic MR Fingerprinting experiments, the MC-algorithm performs such that the least-square estimator in equation (A.2) and the resulting component maps from the algorithm are in good agreement. The signal model for the undersampled images is the same as in section 2.6: $I_j = P_j * M_j$. Following the same approach as in equation (2.51) to find the stationary point of the objective function in equation (A.2), results in:

$$\operatorname{Re} \sum_{j=1}^{N_J} \left(\left(\sum_{n=1}^{N_T} p_n^*(\vec{x}) M_j(\boldsymbol{\theta}^n) - P_j * \sum_{n=1}^{N_T} p_n(\vec{x}) M_j(\boldsymbol{\theta}^n) \right) \overline{M_j(\boldsymbol{\theta}^k)} \right) = 0, \quad \forall x \in G_p, \forall k = 1, 2, \dots, N_T, \quad (\text{A.3})$$

as $\mathcal{D}M_{j,k} = M_j(\boldsymbol{\theta}^k)$. Working out this equation the following expression is obtained:

$$\begin{aligned} & \operatorname{Re} \left(\sum_{j=1}^{N_J} \sum_{n=1}^{N_T} p_n^* M_j(\boldsymbol{\theta}^n) \overline{M_j(\boldsymbol{\theta}^k)} \right) - \\ & \operatorname{Re} \left(\sum_{j=1}^{N_J} \sum_{n=1}^{N_T} (P_j * p_n) M_j(\boldsymbol{\theta}^n) \overline{M_j(\boldsymbol{\theta}^k)} \right) = 0, \quad \forall x \in G_p, \forall k = 1, 2, \dots, N_T. \end{aligned} \quad (\text{A.4})$$

Note that the first term of this equation is simply given by $N\mathbf{p}^*$ with N defined as:

$$N_{k,n} = \sum_{j=1}^{N_J} \overline{M_j(\boldsymbol{\theta}^k)} M_j(\boldsymbol{\theta}^n). \quad (\text{A.5})$$

Introducing $S_{\text{resid};k,n}^{(0,0)} = \sum_{j=1}^{N_J} (P_j - P) \overline{M_j(\boldsymbol{\theta}^k)} M_j(\boldsymbol{\theta}^n)$, the following result is found:

$$\operatorname{Re} \left([N\mathbf{p}^*]_k - [N(P * \mathbf{p})]_k - \sum_{n=1}^{N_T} S_{\text{resid};k,n}^{(0,0)} * p_n \right) = 0 \quad (\text{A.6})$$

Note again that \mathbf{p} is real as it contains the volume fractions, and that P is approximately real as it approaches the Kronecker delta for realistic MRF experiments. The resulting MC undersampling model is:

$$\mathbf{p}^* = P * \mathbf{p} + \operatorname{Re}(N)^{-1} \mathbf{E}(\mathbf{p}, \boldsymbol{\xi}) \quad (\text{A.7})$$

with the error vector:

$$E_k(\vec{x}) = \operatorname{Re} \left(\sum_{n=1}^{N_T} S_{\text{resid};k,n}^{(0,0)}(\vec{x}) * p_n(\vec{x}) \right). \quad (\text{A.8})$$

Note that the first term in equation (A.7) is an approximation of the true tissue parameters \mathbf{p} . This part can only be improved by using a better k-space sampling scheme. The error term \mathbf{E} depend on the acquisition parameters and might be improved by an optimisation of these variables.

B

SLICE SELECTION

The necessity for the \vec{B}_1 field to be rotating with the Larmor frequency in order to enable the flip from the equilibrium state to the transverse plane as explained in section 2.1.1, is exploited for slice selection. Slice selection is the process in which a 2-dimensional plane in the x, y -direction of the sample is selected for imaging. Although direct 3-dimensional MR imaging is possible, 2-dimensional MR imaging is generally used for clinical applications. By applying a gradient field, spatial encoding is achieved as the Larmor frequency becomes spatially dependent:

$$\omega(\vec{r}) = \gamma(B_0 + \iiint \vec{G} \cdot d\vec{r}), \quad (\text{B.1})$$

where $\omega(\vec{r})$ is the spatially dependent Larmor frequency and \vec{G} the applied gradient. Notice that the gradient is the spatial derivative of the magnetic field strength in the z -direction which is a scalar. For slice selection, a gradient $\vec{G} = (0, 0, G_z)$ is applied such that the Larmor frequency can be written as:

$$\omega(z) = \gamma(B_0 + G_z z). \quad (\text{B.2})$$

This gradient is referred to as the slice selection gradient. In order to receive a measurable signal, a 2-dimensional slice of finite thickness is selected by sending an RF-pulse consisting of a range of frequencies as sketched in figure B.1. In this case the frequency range would be: $\text{rect}(\frac{\omega - \bar{\omega}}{\omega_2 - \omega_1})$, where $\bar{\omega} = \frac{\omega_2 + \omega_1}{2}$ and the resulting RF-pulse, known as an excitation or slice selection pulse, is a sinc function in time as is known from elementary Fourier theory. The vertical grey block in figure B.1 is the only part of the sample which is flipped from the equilibrium position into the transverse plane, so the detected signal only gives information about this slice. The thickness of the slice equals the dimension of the voxels in the z -direction and is determined by the range of frequencies in the slice selection pulse and the steepness of the gradient. Microscopic clusters of spins with the same resonance frequency within one voxel are called isochromats.

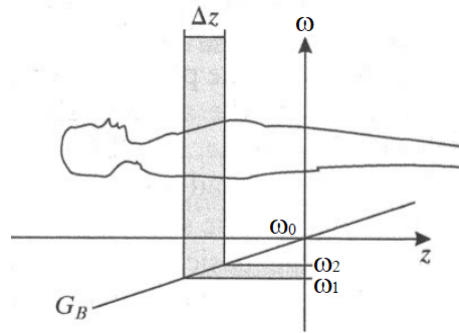


Figure B.1: Sketch of slice selection by application of a slice selection gradient in the z -direction. On the vertical axis the frequency of the slice selection pulse is depicted, which via the gradient can be translated into a location on the z -axis. The horizontal shaded area shows the range of frequencies in a slice selection pulse and the vertical shaded area the resulting slice with thickness Δz which is flipped to generate a signal. (Modified from: Prince et al. 2015 [15])

C

PRINCIPLE OF RECIPROCITY

The transverse component of the magnetisation can be measured using the receive coils of the MR scanner. A schematic representation of the orientation of these coils is depicted in figure 2.4. Because of the orientation of the detection coils an electromotive force (emf) is induced by the transverse component of the magnetisation dictated by Faraday's law of induction:

$$emf = -\frac{d\Phi}{dt}, \quad (C.1)$$

where Φ is the flux through the detection coil (not to be confused with the spin angular momentum Φ_s):

$$\Phi = \iint_{\text{coil area}} \vec{B} \cdot d\vec{S}. \quad (C.2)$$

To derive how the transverse component of the magnetisation of the sample changes the flux in the detection coils, it is convenient to work with the the vector potential which stems from the magnetisation as proposed in [13]. The resulting equation is an application of the *principle of reciprocity* in the context of electrodynamics. The magnetic field associated with the magnetisation of a sample can be modeled as originating from the effective current density:

$$\vec{J}(\vec{r}, t) = \vec{\nabla} \times \vec{M}(\vec{r}, t), \quad (C.3)$$

where \vec{J} is the current density (not to be confused with the total angular momentum \vec{J}_s), \vec{M} the magnetisation of the sample, \vec{r} the position in space and t the time. The vector potential at a position \vec{r} originating from a current source is:

$$\vec{A}(\vec{r}, t) = \frac{\mu_0}{4\pi} \iiint_{\text{all space}} \frac{\vec{J}(\vec{r}', t)}{|\vec{r} - \vec{r}'|} d^3r' \quad (C.4)$$

where \vec{A} is the vector potential and μ_0 the permeability of free space and the effects of retardation are ignored. The magnetic field is calculated as:

$$\vec{B} = \vec{\nabla} \times \vec{A}, \quad (\text{C.5})$$

and using this definition, the flux equation (C.2) can be rewritten using Stokes' theorem:

$$\Phi = \iint_{\text{coil area}} \vec{B} \cdot d\vec{S} = \iint_{\text{coil area}} (\vec{\nabla} \times \vec{A}) \cdot d\vec{S} = \oint_{\text{coil circumference}} \vec{A} \cdot d\vec{l}. \quad (\text{C.6})$$

By substituting equation (C.3) and (C.4) in equation (C.6) the following result is obtained:

$$\Phi(t) = \oint \left[\frac{\mu_0}{4\pi} \iiint \frac{\vec{\nabla}' \times \vec{M}(\vec{r}', t)}{|\vec{r} - \vec{r}'|} d^3 r' \right] \cdot d\vec{l}, \quad (\text{C.7})$$

where the integration boundaries are omitted for readability. The next step is to apply integration by parts where $R(\vec{r}, \vec{r}') \equiv \frac{1}{|\vec{r} - \vec{r}'|}$:

$$\begin{aligned} \iiint \frac{\vec{\nabla}' \times \vec{M}(\vec{r}', t)}{|\vec{r} - \vec{r}'|} d^3 r' &= \iiint R(\vec{r}, \vec{r}') (\vec{\nabla}' \times \vec{M}(\vec{r}', t)) d^3 r' \\ &= \begin{pmatrix} \iiint R \frac{\partial M_z}{\partial y'} d^3 r' - \iiint R \frac{\partial M_y}{\partial z'} d^3 r' \\ \iiint R \frac{\partial M_x}{\partial z'} d^3 r' - \iiint R \frac{\partial M_z}{\partial x'} d^3 r' \\ \iiint R \frac{\partial M_y}{\partial x'} d^3 r' - \iiint R \frac{\partial M_x}{\partial y'} d^3 r' \end{pmatrix} \\ &= \begin{pmatrix} \iint [RM_z]_{y'=-\infty}^{y'=\infty} d^2 r' - \iint [RM_y]_{z'=-\infty}^{z'=\infty} d^2 r' \\ \iint [RM_x]_{z'=-\infty}^{z'=\infty} d^2 r' - \iint [RM_z]_{x'=-\infty}^{x'=\infty} d^2 r' \\ \iint [RM_y]_{x'=-\infty}^{x'=\infty} d^2 r' - \iint [RM_x]_{y'=-\infty}^{y'=\infty} d^2 r' \end{pmatrix} \\ &\quad - \begin{pmatrix} \iiint M_z \frac{\partial R}{\partial y'} d^3 r' - \iiint M_y \frac{\partial R}{\partial z'} d^3 r' \\ \iiint M_x \frac{\partial R}{\partial z'} d^3 r' - \iiint M_z \frac{\partial R}{\partial x'} d^3 r' \\ \iiint M_y \frac{\partial R}{\partial x'} d^3 r' - \iiint M_x \frac{\partial R}{\partial y'} d^3 r' \end{pmatrix} \\ &= - \iiint (\vec{\nabla}' R \times \vec{M}(\vec{r}', t)) d^3 r'. \end{aligned} \quad (\text{C.8})$$

The surface term in this equation is ignored as there is no magnetisation at infinity for finite sources. If equation (C.8) is substituted into equation (C.7) and the closed integral and the integral over space are interchanged the following equation is obtained:

$$\Phi(t) = - \iiint \left[\frac{\mu_0}{4\pi} \oint (\vec{\nabla}' R \times \vec{M}(\vec{r}', t)) \cdot d\vec{l} \right] d^3 r'. \quad (\text{C.9})$$

Using the vector identity $(\vec{A} \times \vec{B}) \cdot \vec{C} = -(\vec{A} \times \vec{C}) \cdot \vec{B}$ the following equation is found:

$$\Phi(t) = \iiint \left[\left(\vec{\nabla}' \times \frac{\mu_0}{4\pi} \oint \frac{d\vec{l}}{|\vec{r} - \vec{r}'|} \right) \cdot \vec{M}(\vec{r}', t) \right] d^3 r', \quad (\text{C.10})$$

where the interchange between the derivative and the integral can be made because it is assumed that the appropriate smoothness conditions are satisfied. Now the reciprocity

is introduced in the equation. If a current would be sent through the detection coil, the following vector potential would occur:

$$\vec{A}(\vec{r}') = \frac{\mu_0 I}{4\pi} \oint \frac{d\vec{l}}{|\vec{r} - \vec{r}'|}, \quad (\text{C.11})$$

where I is the magnitude of the steady current through the coil [34]. If the field produced by one unit of current through the coil is denoted as $\vec{B}^{prod}(\vec{r}, t)$ the following expression is found:

$$\vec{B}^{prod}(\vec{r}') = \frac{\vec{B}(\vec{r}')}{I} = \frac{\vec{\nabla}' \times \vec{A}(\vec{r}')}{I} = \vec{\nabla}' \times \frac{\mu_0}{4\pi} \oint \frac{d\vec{l}}{|\vec{r} - \vec{r}'|}. \quad (\text{C.12})$$

The final expression for the flux through the coil in terms of the magnetisation of the sample is obtained by noting that the term in brackets in equation (C.10) is $\vec{B}^{prod}(\vec{r}')$:

$$\Phi(t) = \iiint_{\text{all space}} \vec{B}^{prod}(\vec{r}) \cdot \vec{M}(\vec{r}, t) d^3 r. \quad (\text{C.13})$$

Finally, using equation (C.1) and noting that outside the sample the magnetisation is zero, the measured signal is as follows:

$$s(t) \propto emf = -\frac{d}{dt} \iiint_{\text{sample}} \vec{B}^{prod}(\vec{r}) \cdot \vec{M}(\vec{r}, t) d^3 r, \quad (\text{C.14})$$

where $s(t)$ is the signal induced by the magnetisation of the sample which is measured with the detection coil. The proportionality factor depends on multiple factors e.g. the amplifier gain.

D

NOISE IN K-SPACE

Instead of adding the complex AWGN to k-space, we added the noise directly to image space. The reason we made this decision is that noise in k-space becomes correlated in image space because of the undersampling. Details of how uncorrelated noise in k-space becomes correlated in image space are presented here.

Under the reasonable assumption that the noise affects all the frequencies equally and is signal independent, the noise in k-space can be modelled as a complex Additive White Gaussian Noise (AWGN) process with 0 mean and variance σ^2 [35]. The resulting signal is:

$$d_j(\vec{k}_{j,l}) = s_j(\vec{k}_{j,l}) + \epsilon_{j,l}, \quad (\text{D.1})$$

where $\epsilon_{j,l} = n_r(0, \sigma^2) + n_i(0, \sigma^2) \cdot i$. In this equation $n(0, \sigma^2)$ is a Gaussian white noise term with 0 mean and variance σ^2 .

Using the k-space signal $d_j(\vec{k}_{j,l})$, undersampled images $I_j(\vec{x})$ can be constructed by applying the discretised inverse Fourier transform:

$$I_j(\vec{x}) = \frac{1}{m_1 m_2} \sum_{l=1}^{N_l} w_{j,l} d_j(\vec{k}_{j,l}) e^{i\vec{k}_{j,l} \cdot \vec{x}} \quad (\text{D.2})$$

where $w_{j,l}$ are again the density compensation weights.

Using equation (3.5) and (D.1) and substituting them into equation (D.2) the following expression is found:

$$I_j(\vec{x}) = \frac{1}{m_1 m_2} \left(\sum_{l=1}^{N_l} \sum_{\vec{y} \in G_p} w_{j,l} M_j(\boldsymbol{\theta}(\vec{y}); \boldsymbol{\xi}) e^{i\vec{k}_{j,l} \cdot (\vec{x} - \vec{y})} + \sum_{l=1}^{N_l} w_{j,l} \epsilon_{j,l} e^{i\vec{k}_{j,l} \cdot \vec{x}} \right). \quad (\text{D.3})$$

The noise in image space is called $E_j(\vec{x}) \equiv \frac{1}{m_1 m_2} \sum_{l=1}^{N_L} w_{j,l} \epsilon_{j,l} e^{i\vec{k}_{j,l} \cdot \vec{x}}$.

To derive some properties of this complex noise term, the following definitions for complex random variable z and w are introduced:

$$\begin{aligned} \mathbb{E}[z] &= \mathbb{E}[\text{Re}(z)] + \mathbb{E}[\text{Im}(z)] \cdot i \\ \text{Cov}[z, w] &= \mathbb{E}[(z - \mathbb{E}[z])\overline{(w - \mathbb{E}[w])}]. \end{aligned} \tag{D.4}$$

Using these definitions and the fact that the added noise $\epsilon_{j,l}$ is uncorrelated in k-space, the derivation of the following properties of E_j are performed by this author and considered trivial:

- $\mathbb{E}[E_j(\vec{x})] = 0$
- $\text{Var}[E_j(\vec{x})] = \frac{2}{(m_1 m_2)^2} \sum_{l=1}^{N_L} w_{j,l}^2 \sigma^2$
- $\text{Cov}[E_j(\vec{x}), E_j(\vec{y})] = \frac{2}{(m_1 m_2)^2} \sum_{l=1}^{N_L} w_{j,l}^2 e^{i\vec{k}_{j,l} \cdot (\vec{x} - \vec{y})} \sigma^2,$

where the factor 2, comes from the fact that the noise has a real and a complex component. This result implies that even though the noise $\epsilon_{j,l}$ in k-space is uncorrelated, there is a noise correlation in image space as $\text{Cov}[E_j(\vec{x}), E_j(\vec{y})]$ is generally not zero for under-sampled images. Notice that undersampling the k-space is the reason why the noise in image space becomes correlated: when the k-space is fully sampled $\text{Cov}[E_j(\vec{x}), E_j(\vec{y})] = 0$.

E

VARIABLE DENSITY SAMPLING

Instead of using a constant density spiral like in Figure 4.20, a variable density spiral might be applied. A variable density spiral has a relatively large amount of measurement points close to $k = 0$, compared to a constant density spiral. This results in a significant reduction of the undersampling error for the conventional sequence as shown in Figure E.1. Notice that the k-space sampling pattern directly influences the pattern of the relative undersampling error.

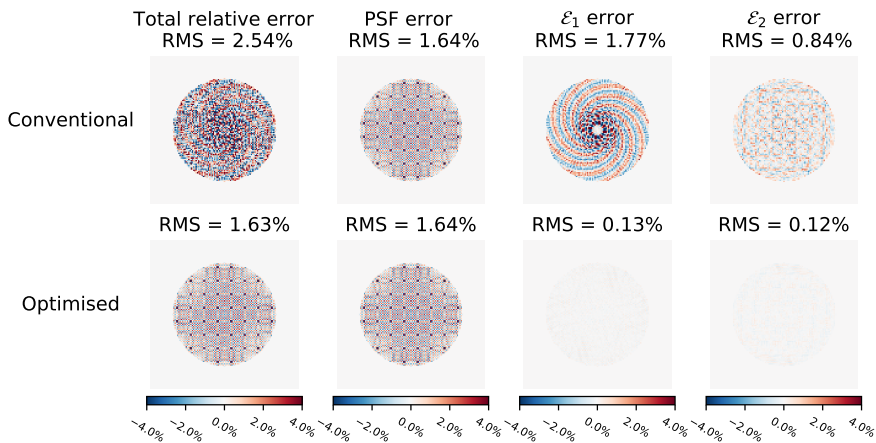


Figure E.1: Relative error in the T_2 map separated into PSF error, ϵ_1 error and ϵ_2 error. The sequence (not shown) is optimised for k-space sampling with a variable density spiral and a ground truth as in Figure 3.4.

F

FOURIER ANALYSIS OF THE \mathcal{E}_2 ERROR

For the analysis of the acquisition dependent term in \mathcal{E}_2 , the vector $\tilde{\mathbf{f}}$ and $\tilde{\mathbf{g}}_{r,q}$ are explored in further detail. As the optimisation in Figure 4.16 is only performed for the T_2 undersampling error, this analysis will focus on $\mathcal{E}_{2,1}$ only thus $r = 1$. A small numerical study pointed out that $q = 0$ is the dominating term for $r = 1$, meaning that there is significant cross-talk from T_1 in the reconstruction for T_2 . The same observation was made in [8]. As $q = 0$ is the dominating term, all results presented here are for the $q = 0$ case. Using the new form from equation (4.10), we know that the inner product of these vectors (where $\tilde{\mathbf{g}}_{1,0}(0)$ and $\tilde{\mathbf{f}}(0)$ have been set to 0) determines the value of the Fourier transform of the acquisition dependent term for a certain \vec{k} . As the different k-space locations of the acquisition dependent term can be studied only one at the time, a \vec{k} -vector shown in Figure E1 is chosen as $\mathcal{F}(\rho_0\theta_{1,0})$ has the highest value here. This implies that this k-space location will probably be the most significant in the Fourier transform of $\mathcal{E}_{2,1}$ as the weighting from $\mathcal{F}(\rho_0\theta_{1,0})(\vec{k})$ is high here (see equation (4.5)).

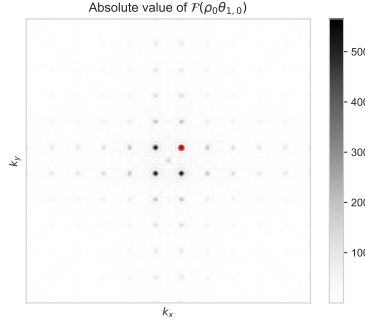
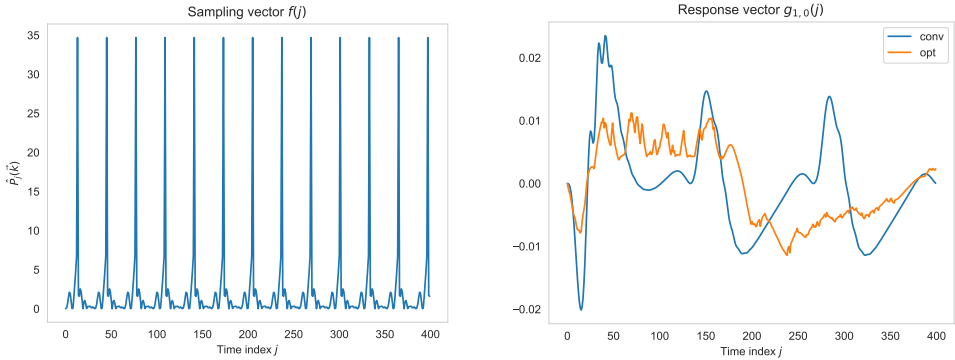


Figure E1: Absolute value of $\mathcal{F}(\rho_0\theta_{1,0})$. The k-space location for which the corresponding $f(j)$ is studied, is marked with a red dot.

For the k-space location marked above the temporal sampling vector \vec{f} is shown in Figure E2a. Notice the periodicity with the undersampling factor of 32 as the spirals are rotated with $\frac{2\pi}{32}$. Also notice that the temporal response vector for the optimised $\vec{g}_{1,0}$ is more constant while the response vector for the conventional sequence is more varying.



(a) The temporal sampling vector \vec{f} . Notice that this is the spiral sampling weighed with the density compensation function at different read-outs for the k-space location shown in Figure E1

(b) The temporal response vector $\vec{g}_{1,0}$. Notice that this vector is dependent on the acquisition parameters.

Figure E2: The sampling and response vectors.

A small numerical study of the Fourier transform of the acquisition dependent term for the k-space location marked in Figure E1 revealed that the sum in equation (4.10) is mainly real. To visualise the product from this equation the real and imaginary parts of the vectors in Fourier space \vec{f} and $\vec{g}_{1,0}$ are shown. Note that the real part of the sum in equation (4.10) is the sum of inner products:

$$\text{Re}\left(\text{Re}(N)_{1,p}^{-1} \hat{S}_{\text{resid};p,0}^{(1,1)}(\vec{k})\right) = \left\langle \text{Re}(\vec{f}), \text{Re}(\vec{g}_{1,0}) \right\rangle + \left\langle \text{Im}(\vec{f}), \text{Im}(\vec{g}_{1,0}) \right\rangle, \quad (\text{E.1})$$

where $\tilde{\mathbf{g}}_{1,0}^0$ and $\tilde{\mathbf{f}}^0$ denote the vectors $\tilde{\mathbf{g}}_{1,0}$ and $\tilde{\mathbf{f}}$, where the $\nu = 0$ term has been set to 0. Figure E3 gives the vectors from both inner products for the conventional and optimised Fourier transform of the response function.

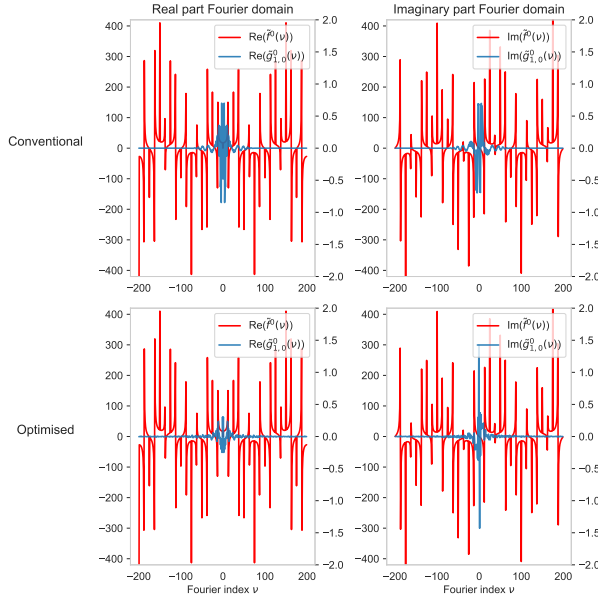


Figure E3: Fourier analysis of the sampling and response vectors. The left axis belongs to the red curve and the right axis to the blue curve.

Note that because response function for the conventional situation is more varying, the non-zero Fourier indices are higher compared to the optimised case for the real part of the spectrum. In the imaginary part, the Fourier spectrum of the conventional response function is broader than the optimised one. Both these effects cause the sum of the inner product of $\langle \text{Re}(\tilde{\mathbf{f}}^0), \text{Re}(\tilde{\mathbf{g}}_{1,0}^0) \rangle$ and $\langle \text{Im}(\tilde{\mathbf{f}}^0), \text{Im}(\tilde{\mathbf{g}}_{1,0}^0) \rangle$ to be significantly decreased in the optimised case. This results in a lower Fourier term of the error for \vec{k}_{marked} where \vec{k}_{marked} is shown in Figure F1:

- Conventional case: $\text{Re}(N)_{1,p}^{-1} \hat{S}_{\text{resid};p,0}^{(1,1)}(\vec{k}_{\text{marked}}) = -0.674$
- Optimised case: $\text{Re}(N)_{1,p}^{-1} \hat{S}_{\text{resid};p,0}^{(1,1)}(\vec{k}_{\text{marked}}) = -0.155.$

This difference in magnitude indicates why the optimised sequence outperforms the conventional one.

G

ISMRM 2021 ANNUAL MEETING

The abstract below had been accepted for the International Society for Magnetic Resonance in Medicine (ISMRM) 2021 annual meeting and was presented to the community on 17 May 2021 by this author. The program number for this abstract was 1561.

Errata:

- The label on the y-axis for Figure 1 and 3 should be ‘TR[ms]’ instead of ‘TR[sec]’.
- Figure 4 is not a proper evaluation of the multi-component optimisation as the applied NNLS algorithm does not perform well in situations with noise. The resulting variance is (way) too large to let the NNLS pass as a reasonable multi-component algorithm. Sparsity regularisation might improve the evaluation, but has not been performed.

1561

Sequence Optimisation for Multi-Component Analysis in Magnetic Resonance Fingerprinting

David Heesterbeek^{1,2}, Frans Vos^{1,2}, Martin van Gijzen², and Martijn Nagtegaal¹¹Department of Imaging Physics, Delft University of Technology, Delft, Netherlands, ²Department of Numerical Analysis, Delft University of Technology, Delft, Netherlands, ³Department of Radiology and Nuclear Medicine, Erasmus MC, Rotterdam, Netherlands

Synopsis

Quantitative MRI and especially MR Fingerprinting make use of complicated acquisition schemes and signal models to measure tissue parameters. The sequence choice is crucial for the noise robustness for parameter estimations of different tissues. Multi-component (MC) signal models for MRF are of importance to estimate partial volume effects or myelin-water fractions for example. We propose to use the Cramér-Rao bound to assess and optimise the multi-component parameter estimations for MRF. The optimised flip angle and TR patterns for MC-MRF were highly structured which was also observed for the optimisation based on the single-component model, but structural differences were noticed.

Introduction

Quantitative Magnetic Resonance Imaging has the potential to improve the reproducibility of MRI measurements by taking confounding physical processes into account that underlie the MR signal. In MR Fingerprinting (MRF)[1] a transient state signal is acquired, such that multiple relevant tissue parameters as well as system properties can be estimated simultaneously.

MRF typically consists of a flexible framework in which pseudo randomised acquisition patterns with varying length, flip angles (FA) and repetition times (TR) are applied. These encoding parameters can be optimised using different criteria e.g. by maximising the orthogonality of the dictionary signals[2] or reducing the Cramér-Rao bound (CRB) to improve the signal-to-noise ratio (SNR)[3,4]. In effect this can lead to enhanced measurement precision and/or a reduction in scan time.

These single-component optimisations do not necessarily improve estimations when multiple tissues are present in one voxel. A multi-component model is required, when estimating e.g. the myelin water fraction in white matter, a relevant parameter in many diseases such as multiple sclerosis, schizophrenia and concussions[5], or on boundaries between white matter, grey matter or CSF. In multi-component analysis the mixing of signals from different tissues in one voxel is taken into account. Current efforts in multi-component MRF (MC-MRF) focus on finding an optimal solution to a linear inverse problem[6,7] using standard MRF sequences. The choice of FA and TR patterns can, however, influence the precision of the multi-component analysis. In this work we introduce a framework for quantifying and optimising the precision of a chosen acquisition sequence based on the CRB specifically for MC-MRF.

Methods

The CRB is an estimation-theoretical limit to the precision with which a parameter can be estimated using an unbiased estimator. As such the CRB makes it possible to quantitatively compare different MRF sequences[3], and is determined by the inverse of the Fisher information matrix \mathbf{F} .

To model the spin dynamics the Extended Phase Graph (EPG) formalism[8] was used, which typically yields marked computational advantages compared to the isochromat summation approach used in[3].

The MC-MRF signal is modelled as:

$$\mathbf{s}[n] = \sum_i \mathbf{m}_i(T_1^i, T_2^i, M_0^i)[n] + \mathbf{w}[n],$$

where $\mathbf{s}[n]$ is the measured magnetisation at the n th read-out time, $\mathbf{m}_i[n]$ is the theoretical transverse magnetisation in the absence of noise for tissue x_i at the n th read-out time and $\mathbf{w}[n]$ is independent identically distributed Gaussian noise. For the single-component model i concerns a single index.

Sequence optimisation for the single-component model is performed for a limited set of parameters, i.e. T_1 , T_2 and M_0 [3]. However, for the multi-component optimisation, the number of parameters for which we optimise scales linearly with the number of tissues considered. When two tissues are considered these parameters are T_1^a , T_2^a , M_0^a , T_1^b , T_2^b and M_0^b where the superscript is meant to distinguish different tissues.

Using the multi-component model the weighted sum of the CRBs can be minimised by optimising the acquisition parameters FA (α) and TR for a sequence (length N), using empirically defined constraints:

$$\begin{aligned} \min_{\{\alpha_n, TR_n\}_{n=1}^N} & \sum_{i=1}^6 w_i \cdot F(T_1^a, T_2^a, M_0^a, T_1^b, T_2^b, M_0^b)_{i,i}^{-1} \\ \text{s.t.} & \quad 10^\circ \leq \alpha_n \leq 60^\circ \quad \forall n \in \{2, 3, \dots, N\} \\ & \quad 11 \text{ ms} \leq TR_n \leq 15 \text{ ms} \quad \forall n \in \{1, 2, \dots, N\} \\ & \quad |\alpha_{n+1} - \alpha_n| \leq 1^\circ \quad \forall n \in \{1, 2, \dots, N-1\} \end{aligned}$$

where w is a weighting factor. The first two constraints enable both that results are unique as well as clinically feasible while the last constraint is set in place to keep the evolution of the magnetisation smooth which is beneficial in virtually all decoding schemes. This non-linear constrained optimisation problem is solved by using a Sequential Least-Squares Quadratic Programming algorithm.

Results

Numerical optimisation of the CRB using a single-component model and EPG for an MRF-IR-FISP[9] sequence is shown in Fig.1. These results are extremely similar to the results in[3] for the same problem.

The variance in estimated T_1 and T_2 of grey and white matter, using the conventional (see initialisation Fig.1) and optimised sequence, for different SNRs is shown in Fig.2.

Similarly, the optimised parameters and variance in T_1 and T_2 for MC-MRF are shown in Fig.3 and Fig.4.

CRB evaluation for MC-MRF for different T_1 - T_2 combinations for the conventional and optimised sequence are shown in Fig.5. The difference (row 3) shows that the optimised sequence generally gives a lower rCRB, as we expected. The figure shows that the rCRB of a parameter increases if this parameter for tissue b approaches the value of tissue a. The horizontal and vertical lines however, show that if the parameters are equal the rCRB decreases. Intuitively this marks the transition from being hard to distinguish (prone to errors) to being exactly the same (comparable to estimating one tissue using a single-component model).

Discussion and Conclusion

We introduced an optimisation method based on the theoretical CRB for MC-MRF. Its usefulness was shown in the application to different MRF-FISP sequences using the multi-component model. Further comparisons can be made with other regular sequences used for multi-component estimations such as multi-echo spin echo and mcDESPOt.

Monte Carlo simulations showed that improvements could be obtained in multi-component estimations by sequence optimisation. In future work we will perform in vitro and in vivo scans to assess the achieved improvement in precision in practice.

The results were optimised for white and grey matter relaxation times, in further studies we plan to optimise for different tissues such as myelin water and CSF.

In conclusion, the Cramér-Rao Bound shows to serve as a tool in multi-component models to quantitatively assess and optimise different sequences. This method provides new insights into the possibilities and restrictions of multi-component estimations.

Acknowledgements

M.A. Nagtegaal his research is funded by the Medical Delta consortium, a collaboration between the Delft University of Technology, Leiden University, Erasmus University Rotterdam, Leiden University Medical Center and Erasmus Medical Centre.

References

- [1] Dan Ma, Vikas Gulani, Nicole Seiberlich, Kecheng Liu, Jeffrey L. Sunshine, Jeffrey L. Duerk, and Mark A. Griswold. Magnetic Resonance Fingerprinting. *Nature*, 495(7440):187–192, March 2013.
- [2] Ouri Cohen and Matthew S. Rosen. Algorithm comparison for schedule optimization in MR fingerprinting. *Magnetic Resonance Imaging*, 41:15–21, September 2017.
- [3] B. Zhao, J. P. Haldar, C. Liao, D. Ma, Y. Jiang, M. A. Griswold, K. Setsompop, and L. L. Wald. Optimal Experiment Design for Magnetic Resonance Fingerprinting: Cramér-Rao Bound Meets Spin Dynamics. *IEEE Transactions on Medical Imaging*, 38(3):844–861, March 2019.
- [4] Jakob Assländer, Riccardo Lattanzi, Daniel K. Sodickson, and Martijn A. Cloos. Optimized quantification of spin relaxation times in the hybrid state. *Magnetic Resonance in Medicine*, June 2019.
- [5] Alex L. MacKay and Cornelia Laule. Magnetic Resonance of Myelin Water: An in vivo Marker for Myelin. *Brain Plasticity*, 2(1):71–91, 2016.
- [6] Debra F. McGivney, Rasim Boyacoglu, Yun Jiang, Megan E. Poorman, Nicole Seiberlich, Vikas Gulani, Kathryn E. Keenan, Mark A. Griswold, and Dan Ma. Magnetic resonance fingerprinting review part 2: Technique and directions. *Journal of Magnetic Resonance Imaging*, 51(4):993–1007, July 2019.
- [7] Martijn Nagtegaal, Peter Koken, Thomas Amthor, and Mariya Doneva. Fast multi-component analysis using a joint sparsity constraint for MR fingerprinting. *Magnetic Resonance in Medicine*, 83(2):521–534, July 2019.
- [8] Matthias Weigel. Extended phase graphs: Dephasing, RF pulses, and echoes - pure and simple. *Journal of Magnetic Resonance Imaging*, 41(2):266–295, February 2015.
- [9] Yun Jiang, Dan Ma, Nicole Seiberlich, Vikas Gulani, and Mark A. Griswold. MR fingerprinting using fast imaging with steady state precession (FISP) with spiral readout. *Magnetic Resonance in Medicine*, 74(6):1621–1631, 2015.

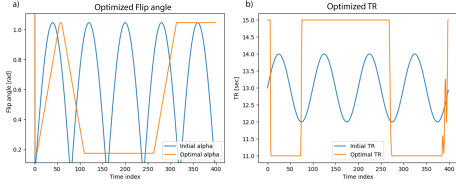


Figure 1: a) FA and b) TR sequences at initiation and after optimisation for single-component MRF. Optimisation was performed for tissue parameters T_1 , T_2 , $M_0 = 700$ ms, 60ms, 0.6, 850ms, 50ms, 0.6, 1100ms, 102ms, 0.6 with the constraints mentioned in the Methods section. These optimised patterns are highly similar to the optimised pattern in [3] which was based on an isochromat summation (140 minutes) approach instead of the EPG simulations (40 minutes) as used here.

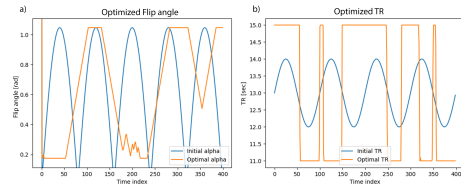


Figure 3: a) FA and b) TR sequences at initiation and after optimisation for multi-component MRF. Optimisation was performed for tissue parameters T_1^a , T_2^a , $M_0^a = 700$ ms, 60ms, 0.3 and T_1^b , T_2^b , $M_0^b = 1100$ ms, 102ms, 0.3 with the constraints mentioned in the Methods section. Different initialisation of the optimisation problem returned the same result.

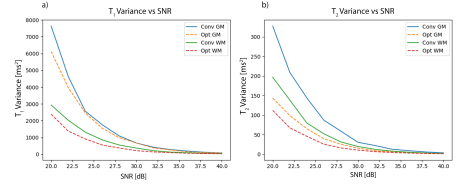


Figure 2: a) Variance in T_1 estimation. b) Variance in T_2 estimation. SNR is defined as $\text{SNR} = 20\log_{10}(M_0/\sigma)$. The variance is estimated using a Monte-Carlo approach with 1000 noisy signal realisations per tissue. Grey and white matter are modelled separately using a single-component model.

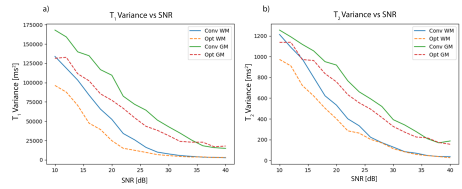


Figure 4: a) Variance in T_1 estimation. b) Variance in T_2 estimation. The variance is estimated using a Monte-Carlo approach with 1000 realisations. Multi-component estimations were performed using the NNLS algorithm. Grey and white matter are modelled together using a multi-component model.

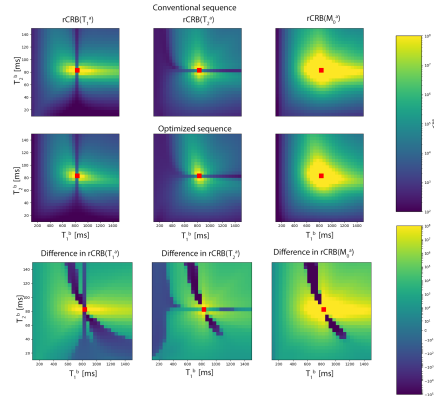


Figure 5: Relative CRB values were calculated using the multi-component Fisher matrix for a conventional MRF sequence (row 1) and an optimised sequence (row 2). The difference is shown in row 3 by subtracting the second row from the first. The rCRB is defined as $\text{rCRB} = \text{CRB}/(\sigma^2\theta^2)$ where θ represents T_1^a , T_2^a or M_0^a . Tissue parameters for one tissue (superscript a) were fixed at $T_1^a = 800$ ms, $T_2^a = 80$ ms, while T_1^b and T_2^b for the second tissue (superscript b) vary. In the centre red dot the 2 tissues are exactly the same, resulting in a singularity.

CURRICULUM VITÆ

D.G.J. HEESTERBEEK

30-04-1997 Born in Beverwijk, The Netherlands.

EDUCATION

- 2009–2015 Grammar School (*Cum Laude*)
Kennemercollege Atheneum, Beverwijk
- 2015–2018 Bachelor in Applied Physics (*Cum Laude*)
Delft University of Technology, Delft
Thesis: Deconvolution for coherent imaging
Supervisor: Prof. dr. ir. M. Verhaegen
- 2017–2018 Minor in Applied Mathematics
Delft University of Technology, Delft
- 2018–present Master in Applied Physics
Delft University of Technology, Delft
- 2019–present Master in Applied Mathematics
Delft University of Technology, Delft

PROJECTS

- 2016–2019 Honours program for Applied Physics
Delft University of Technology, Delft
- 2021 ISMRM Conference contribution
D.G.J. Heesterbeek, F.M. Vos, M.B. van Gijzen and M.A. Nagtegaal.
Sequence Optimisation for Multi-Component Analysis in Magnetic Resonance Fingerprinting.
Poster presented at: ISMRM; 2021 May 17